NASA Contractor Report 174851

Effects of MAR-M247 Substrate (Modified) Composition on Coating Oxidation and Coating/Substrate Interdiffusion

Brian H. Pilsner

Michigan Technological University
Houghton, Michigan

February 1985

TABLE OF CONTENTS

i

LIST OF APPENDICES

ii

I. INTRODUCTION

In most contemporary applications, protective coatings are required for the components used in the hot sections of turbine engines. The two types of coatings generally applied are aluminide and overlay coatings. The purpose of these coatings is to provide oxidation resistance with minimum superalloy degradation (1,2). The ability to tailor the coating composition (1-4) and to apply larger coating thicknesses (1,5,6) has resulted in the increased use of MCrAl (M=Metal) overlay coatings in turbine applications (2,7-10). Thicker coatings provide improved oxidation resistance, while compositional control allows matching of the composition of the coating to that of the substrate, minimizing substrate/coating degradation via interdiffusion (1,3,4,11).

The optimum conditions occur when a compact protective oxide is formed at the oxide/coating (coating surface) interface (12-14). Earlier generation Co- and Ni-base alloys contained sufficient Cr levels to provide a protective Cr_2O_3 scale (15). However, the new generation of turbine alloys have been designed with a significant number of secondary elements for strengthening purposes with a corresponding decrease in Cr (13,15-17). These new alloys do not contain enough Cr to provide the protective scale (15,17). These strengthening elements have allowed the new generation of superalloys to maintain their mechanical integrity at higher temperatures

2

(3,13,17). Even if the alloys could be designed with a Cr level high enough to form the Cr_2O_3 scale, the Cr_2O_3 scale is no longer protective at these increased temperatures (18). At these higher temperatures, the most desirable barrier to rapid oxidation is the α-Al_2O_3 scale (2,13-14,18-19). Superalloys usually do not have the levels of Al necessary to provide the Al_2O_3 scale (2,17).

Normally (Fe, Co, Ni) CrAl-type coatings are used to protect superalloys (16,18,20-22). The Al is added in significant quantities to form the Al_2O_3 scale (15,16), while the Cr provides improved hot corrosion resistance (3,23).

The high degree of compositional control of overlay coatings allows adjustments of the mechanical properties of the coating to meet specific applications (2). This freedom allows coatings in turbine applications to have good ductility and high thermal fatigue resistance over a wide temperature range (2,4,16). The high ductility results from the presence of the brittle high Al β (NiAl or CoAl) phase embedded in a soft γ matrix (Ni solid solution).

The two main techniques used to apply overlay coatings are low pressure plasma spray (6,10) and physical vapor deposition (2,5,10). Generally, low pressure plasma spray coatings can obtain higher compositional control than physical vapor deposition (4). The disadvantages of overlay coatings compared to aluminide coatings are the inability to coat internal channels (9,5), the need for increased apparatus (5), and the inability to coat large batches (5).

In summary, the ability to tailor the coating composition to meet the higher oxidation and corrosion environments has resulted in increased interest in overlay coatings.

Coating and Substrate Degradation

Both the coating and the substrate are degraded by coating/substrate interdiffusion (2,6,12,24), while the coating is also degraded by diffusional transport of Al to the protective scale at the coating surface (2,24,25).

Coating/substrate interdiffusion can decrease the mechanical properties of the substrate (16). The new generation of alloys contain many secondary alloying elements (13,15-17), while overlay coatings normally are ternary or quaternary compositions plus a small addition of an active element (2,16). The significant secondary elements in the substrate result in a driving force for the diffusion of these elements into the coating. The degradation effects are often difficult to assess since the superalloy interactions are complex. The presence of the coating, itself, may also decrease the mechanical properties (creep and fatigue strength) of the coating/ substrate system (2,4,16).

The significant differences in coating and substrate composition also result in coating degradation via coating/substrate interdiffusion. The concentration of Al in the superalloy (substrate) is generally much lower than the concentration in the coating (3). The Al gradient can result in signi-

ficant quantities of Al moving into the substrate (3). Permanent loss of the Al reduces the oxidation resistance potential of the coating. The term "permanent" loss is used since it is possible for Al that has been transported into the substrate to reverse directions and move back into the coating at a later time (24). The return is due to the reduction of Al in the coating due to oxide scale formation. The Al in either case is replaced by Ni and other substrate alloying elements (26, 27).

The second coating degradation mechanism is the loss of Al via diffusional transport to the oxide/coating interface (2, 27), where the Al is selectively oxidized (12,29). During isothermal oxidation, the Al_2O_3 oxide will grow parabolically (12) and the Al consumption rate will decrease with time. However, most high temperature turbine components are subject to thermal cycling (2,12,25,30). Thermal cycling results in random spalling of the protective scale (30). The reduction in scale thickness results in increased Al transport to replace the scaled oxide and thus increased Al consumption. Oxide spalling in cyclic applications can be attributed to the stresses generated by the differences in the thermal expansion coefficients of the Al_2O_3 scale and the coating (2,25,30). Oxide spalling can be reduced by small additions of active elements (7,14,19,31-35), by decreasing the temperature differential (the ΔT of the heating and cooling cycles) (30), by decreasing the cooling rate (35), and by increasing the cycle

length (19).

Higher temperatures increase the rates of both degradation mechanisms. Interdiffusion is increased since diffusion increases exponentially with temperature. The demand for Al at the oxide/coating interface is also increased since the rate of oxidation increases with temperature (36).

Continued degradation of overlay coatings results in the formation of less protective Ni and Cr oxide scales (16,37). The growth of less protective oxides results in increased spalling and oxidation (breakaway oxidation). The less protective oxides form when the coating is no longer capable of supplying the necessary flux to the protective Al_2O_3 scale (16,38). Heckel and Nesbitt (38) defined the occurrence of breakaway oxidation as when the Al concentration at the oxide/coating interface is approximately zero. The higher rates of spalling and/or oxide growth lead to earlier coating failure. The continued formation of less protective oxides also leads to internal oxidation since O is able to penetrate the coating (29,39, 12). Internal oxidation can totally deplete the coating of Al and also shorten coating life (12,39).

Effects of Tantalum

The major substrate compositional variation in this study is Ta concentration. The increased use of Ta in the aerospace industry combined with 97% of its supply being imported has resulted in its designation as a strategic element (40). Tan-

talum is used in advanced nickel-base superalloys primarily to increase high-temperature strength (40,41) and to improve oxidation resistance (3,40). Recent investigations have been undertaken to further understand the effects of Ta (40-42).

Tantalum has been shown to increase the high-temperature mechanical properties of $\gamma + \gamma$' nickel-base superalloys. These improvements have been attributed to the increase in γ' wt. fraction and increased solid solution hardening of γ with increasing Ta (41). These increases are caused by changes in the phase chemistries of γ and γ'.

Tantalum has been shown to vary oxidation resistance (10, 34,42,43). Increases have been observed in both aluminide (34), and low-pressure, plasma-sprayed coatings (10). In both cases, high concentrations of Ta (exceeding 8 wt.%) were found in either the coating or substrate or both. There is no complete explanation of the beneficial effects of Ta on oxidation resistance of MCrAlY coating alloys (3). Small concentrations of Ta (3 wt.%) were also shown to increase oxidation resistance in uncoated complex superalloys, while oxidation resistance was decreased when Ta was significantly (9 wt.%) increased (42). The increase in oxidation resistance was attributed to the earlier formation of the protective Al_2O_3 scale, while the decrease was attributed to the formation of the less protective Ta_2O_5 (42).

Active Elements

Small amounts of active elements such as zirconium, yt-trium, and hafnium can produce a marked improvement in oxidation behavior (7,14,19,31-35). Most theories relate the higher oxidation resistance to improved scale adhesion (7,14,32,33,35). In many situations more than one theory has been attributed to the improved oxidation resistance (50). Five of the more popular theories are discussed below:

1. The mechanical keying ("pegging") of the oxide to the coating or alloy. In this case, the reactive elements form a dispersed oxide or reactive particle which pegs the oxide to the coating (31,33,44,45).

2. The active elements enhance the plasticity of the scale. The plasticity of the scale may be increased by a change in defect structure caused by the presence of the active elements (46).

3. The active elements reduce the quantity of voids present at the oxide/coating interface. The active elements act as vacancy sinks in the coating. This reduces the number of vacancies at the oxide/coating interface which reduces the void concentration at the inter-face (47).

4. The active elements produce an oxide between the oxide scale and the coating with an inter-mediate expansion coefficient. The development of an intermediate expansion coefficient reduces

the stresses generated during thermal shock, thereby reducing spallation (40).

5. The active elements block the transport of Al and O along grain boundaries. By blocking the transport, these elements limit internal oxidation of the coating or alloy, and also limits the lateral growth of the Al_2O_3 scale (18).

Superalloy Interactions

The high number of elements in superalloys (often ten or more) increases the difficulty of understanding complex oxidation and interdiffusion interactions in coating/substrate systems (9). Unlike simple binary systems, diffusion in ternary and multicomponent systems is affected by the gradients of numerous elements. In the Ni-Cr-Al system, both uphill diffusion of Cr and Al is seen (24,49). The uphill diffusion in this system is attributed to the diffusion cross terms (i.e., the flux of element A is influenced by the gradients of elements B,C,D... as well as by its own gradient) (24). This example indicates the complexities of trying to analyze multicomponent diffusion in superalloys.

The complexity of determining multicomponent diffusion coefficient data has prompted studies on ternary systems where diffusion coefficient data is more readily determined. The presence of Al and Cr in commercial superalloys has resulted in numerous oxidation and interdiffusion studies based on the Ni-Cr-Al system (19,24,29,38,49). Work has progressed

in this area to the point where a model capable of predicting the effects of overlay coating degradation by simultaneous oxidation and coating/substrate interdiffusion for the Ni-Cr-Al system has become available (24). This study will, in part, investigate the applicability of this Ni-Cr-Al ternary oxidation model to complex superalloys.

Purpose of Study

The purpose of the present study is twofold:

1. To examine the effects of Mar-M247 (modified) substrate composition variations on overlay coating oxidation resistance and coating/substrate interdiffusion. Particular emphasis will be placed on:

   a. Effect of substrate Ta concentration;
   b. Effect of substrate C concentration;
   c. Effect of substrate grain boundary strengthening element additions.

2. To compare the oxidation resistance and interdiffusion interactions of the overlay-coated $\gamma+\gamma'$ Mar-M247 substrate to the overlay-coated γ Ni-Cr-Al substrate.

Mar-M247 (modified) substrates were low-pressure, plasma-coated with a $\gamma+\beta$ Ni-Cr-Al-Zr coating. The coating was identical to the one applied to the ternary Ni-Cr-Al substrates studied in a previous investigation (24,38). The specimens

were given the same cyclic oxidation treatment (1 hour at 1150°C) as those in this previous study. Diffusion couples of the γ+β coating composition and the γ+γ' Mar-M247 substrate were also employed to evaluate coating/substrate interdiffusion.

II. PROCEDURE

The Mar-M247 (modified) substrates investigated can be divided into three groups according to Ta concentration (Tables 1 and 2, see Appendix 1 for complete analysis). The following substrate values are listed by weight percent. Group 1 contains substrates A(0 Ta) and B(3 Ta) which are equaxied poly-crystalline alloys, and substrates C(0 Ta) and D(3 Ta) which are directly solidified polycrystalline alloys. Group 1 substrates only depart from the commercial Mar-M247 composition is the Ta variation (i.e. substrates B and D are the commercial Mar-M247 composition). Group 2 contains single crystal substrates E(0 Ta), F(3 Ta), and G(4.5 Ta) which do not contain the grain boundary strengthening elements (Hf, Zr, and B) of commercial Mar-M247. Group 3 contains single crystal substrates H(0 Ta), I(1.5 Ta), and J(3 Ta) without the carbon and the grain boundary strengthening elements. The microstructures of these alloys are shown in Figure 1a and 1b. These Mar-M247 (modified) substrates were cast by the Howmet Turbine Components Corporation. The single crystal alloys were cast by the withdrawal process.

Diffusion couple specimens were fabricated from the cast Mar-M247 (modified) substrates and the arc melted coating powder (coating-powder composition, Table 3, see Appendix 1 for complete analysis). The "coating" alloy was molded by pressing 25 grams of the alloyed Ni-Cr-Al-Zr powder (Table 3)

TABLE 1

Substrate Nominal Compositions [w/o]

	A Conv.	B Conv.	C DS	D DS	E XL	F XL	G XL	H XL	I XL	J XL
Ta	--	3		3	–	3	4.5	–	1.5	3
C	0.1	0.1	0.1	0.1	0.1	0.1	0.1			
Zr	.05	.05	.05	.05						
B	.01	.01	.01	.01						
Hf	1.2	1.2	1.2	1.2						

For all alloys:

Cr 8.0, W 9.6, Co 9.5, Mo 0.5, Al 5.2, Ti 0.6, Ni Bal

TABLE 2

Substrate Nominal Compositions [a/o]

	A Conv.	B Conv.	C DS	D DS	E XL	F XL	G XL	H XL	I XL	J XL
Ta	--	1	--	1	--	1	1.5	--	0.5	1
C	0.5	0.5	0.5	0.5	0.5	0.5	0.5			
Zr	.04	.04	.04	.04						
B	.06	.06	.06	.06						
Hf	0.4	0.4	0.4	0.4						

For all alloys:

Cr 9.0, W 3.1, Co 9.4, Mo 0.3, Al 11.3, Ti 0.7, Ni Bal

TABLE 3

Coating Nominal Composition [w/o & a/o]

	Al	Cr	Zr	Ni
Weight Percent:	13.4	14.0	0.1	Bal
Atomic Percent:	24.9	13.5	0.05	Bal

14

a)

b)

c)
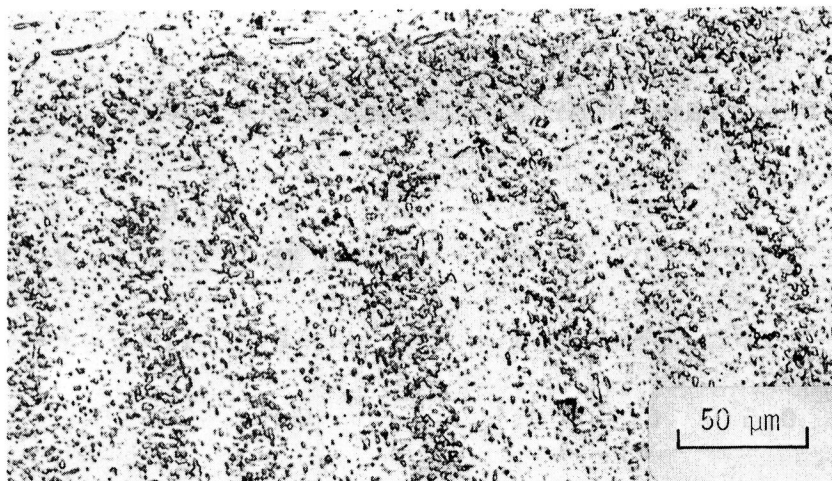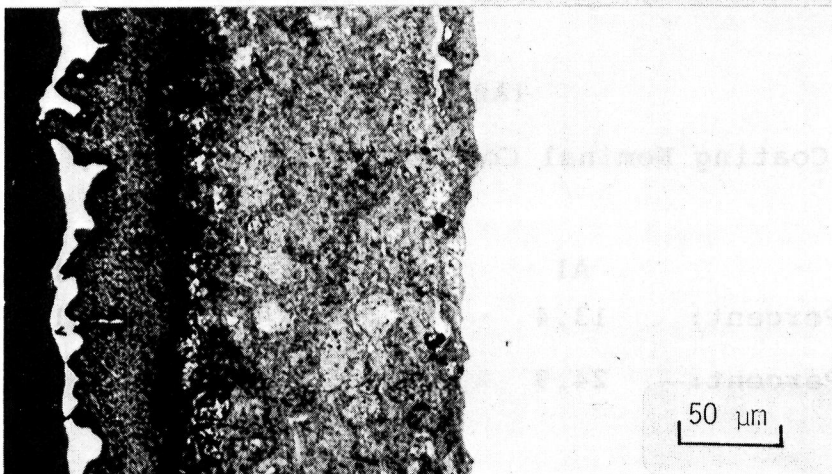
Ni Cu COATING   SUBSTRATE
Plating

Figure 1   Microstructures of substrates and coating a)Sub-
             J($\gamma+\gamma'$)after 200 hour anneal at 1150°C b) Substrate
             D($\gamma+\gamma'$ +carbides)after 200 hour anneal at 1150°C
             c) As sprayed coating on substrate H

with 3.35 grams of Al, 3.50 grams of Cr, and 18.15 grams of Ni (the elemental powder was used to increase pressibility). The 13.4 Al, 14.0 Cr, 0.05 Zr, balance Ni by weight, powder compact was vacuum arc melted several times. Both the substrate and the "coating" alloy were sliced into 2mm thick wafers. The surface of both wafers were polished through 600 grit SiC paper and cleaned with methanol. The two wafers were pressed together in a molybdenum canister. The couple specimens were heat treated at 1150°C in a flowing-argon, tube furnace for 200 hours.

The Mar-M247 (modified) substrates were low pressure, plasma sprayed with a composition of 13.4 Al, 14.0 Cr, 0.1 Zr, balance Ni by weight (Table 3). The as sprayed microstructure is shown in Figure 1c. The overlay coating was applied by a low-pressure (60-70 torr), plasma-spray process at the General Electric Research and Development Center, Schenectady, New York. Powder sizes of -400 mesh were used. The procedure used to coat these substrates involves two spraying steps. First, the dumbell shaped specimen (Figure 2a) was gripped at the 0.25" diameter section and the entire geometry coated. Next, the entire specimen was removed from the low pressure vessel and the ends (cross hatched) removed. The remaining length (Figure 2b) was returned to the vessel where the cut surfaces of the length were coated. The two-step spraying process results in a unwanted oxide layer at the
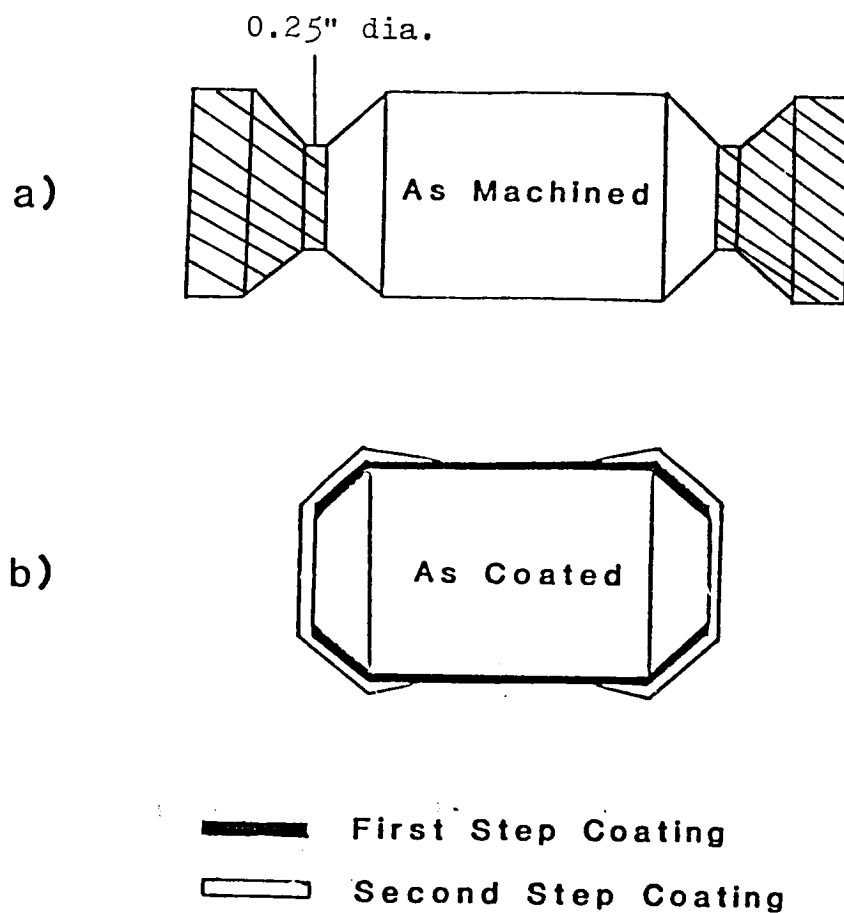
0.25" dia.

a)

As Machined

b)

As Coated

First Step Coating

Second Step Coating

Figure 2.   The specimen geometry coated in this study
            a) As machined uncoated dumbell geometry;
            b) As coated cylinder specimen. Scale 2:1
               (coating not to scale)

coat/coat interface. This oxide layer reduces the apparent oxidation resistance of the specimen (see Appendix 2). The average coating thickness for the specimens were generally in the 80-140 μm range. Each specimen had coating thickness variations which were usually less than 30 μm.

The average coating thickness specification does not adequately characterize the coating thickness of a specimen when large coating thickness variations are present. This problem is evident when evaluating change in weight (ΔWg) curves. Thinner coatings result in high rates of spalling at earlier times. The higher rates are a result of the earlier depletion of the available Al supply. In the case of specimens with large coating thickness variations, one side may be experiencing breakaway oxidation (high weight losses), while the other side is experiencing minimum oxidation (low weight losses). This phenomena results in larger weight losses than a specimen with identical average coating thickness and negligible thickness variations.

Two average coating thickness values were listed (on each ΔWg curve) to more completely characterize the coating thickness. Generally, one or two longitudinal slices were cut through each specimen. The first slice was cut in the region where the oxide spalling was the greatest. This location was based mainly on the appearance of the specimen (color of oxide and surface roughness). In certain cases, X-ray diffraction was utilized to determine this location. If necessary, another

slice was cut through the specimen (required in cases where minimum degradation had occurred) to determine the minimum. These slices allowed the average thickness of 2-4 sides to be determined. The average thickness of each side was measured. A minimum of 15 measurement were averaged for each side. The first value specified (on each ΔWg curve) is the average thickness of the thinnest side. The second value specified (on each ΔWg curve) is the average thickness based on the measurements of all sides measured.

The LPPC substrates were cyclically oxidized at the NASA-Lewis Research Center, Cleveland, Ohio. Each cycle involved a one-hour, isothermal treatment at 1150°C in still air followed by a 20 minute cool at room temperature in still air. The one-hour cycle term described from this time forth includes both the one hour heat treatment plus the 20 minute cool. At certain cyclic increments (Table 4), specimens were cooled to room temperature and the specimens were weighed.

A set of LPPC specimens was given a preheat treatment of four hours at 1150°C in a still air atmosphere. The specimens were cycled with an identical set of specimens that did not receive the heat treatment. No effect was seen on their oxidation resistance (ΔWg curves) and excellent adhesion of the coating to the substrate was observed in both cases (optical microscope observation). The set of low-pressure, plasma-coated (LPPC) specimens studied in the remainder of the investigation were not given pre-oxidation heat treatments.

TABLE 4

Wg Measuring Schedule

original weight	160 cycles
1 cycle	175 cycles
15 cycles	190 cycles
30 cycles	200 cycles
45 cycles	250 cycles
60 cycles	300 cycles
75 cycles	350 cycles
90 cycles	400 cycles
100 cycles	450 cycles
115 cycles	500 cycles
130 cycles	550 cycles
145 cycles	

Weight-change curves were used to evaluate the oxidation behavior of the coating as affected by the substrate composition. The original weight of LPPC substrate was measured and subtracted from the weight of the specimens measured at specific cycle times (Table 4). The ΔWg was given in terms of the change in weight per unit surface area (Mg/cm^2). An example of ΔWg curves for low- and high-oxidation resistance is shown in Figure 3.

The oxide scale was examined using X-ray diffraction and scanning electron microscopy. X-ray diffraction using a Picker X-ray system with an operating voltage of 40 KV and a current of 20 ma was used on the oxide surface. The oxide volume fractions were ranked qualitively. The energy dispersive system (EDS) on the scanning electron microscope (SEM) was used to correlate oxide morphology and X-ray diffraction data. The oxidized specimens were carbon coated to minimize charging. The SEM was a JOEL 35C operated at 15 KV with a beam current of approximately 1×10^{-10} ma.

Standard metallographical techniques were used to prepare the specimens for microstructural examination. Marbles etchant was utilized to examine the microstructure.

Compositional studies were performed with the aid of both the SEM and the electron microprobe (EM) with necessary analytical capabilities (procedures described in Appendix III). The accuracy of both the SEM/ZAF and EM/ZAF measurement tech-
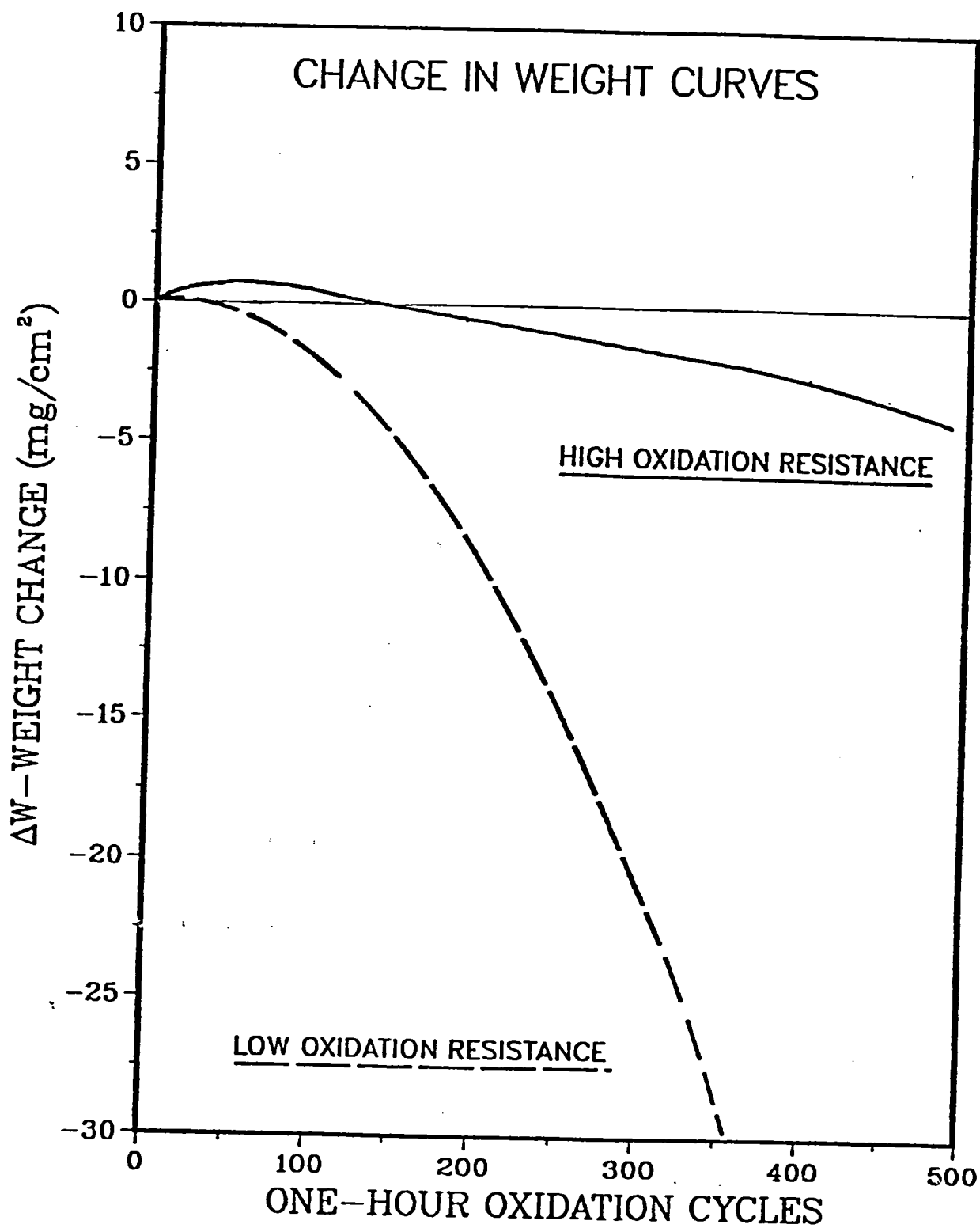
Figure 3. Comparison of ΔWg curves for low and high oxidation resistance.

niques were checked against known compositions. (See Appendix III). Main attention was placed on the investigation of LPPC substrates C, D, E, F, H, and J since extensive cyclic oxidation testing was performed on this group (one set of LPPC substrates A and B were also cycled).

III.   RESULTS

Diffusion Couple Studies

Microstructure

The coupling of the $\gamma+\beta$ coating composition with the $\gamma+\gamma'$ superalloy substrate composition resulted in both "coating" alloy and substrate phase depletion zones (Figure 4a-d). Generally, the coating/substrate interdiffusion resulted in γ' depletion in the substrate and β depletion in the coating (Figures 4a-c). The exceptions were the high carbon, tantalum-free substrates (A, E, and C) which developed a continuous $M_{23}C_6$ carbide layer at the coating/substrate interface (Figures 4d-e). The continuous, high-Cr, carbide layer results in γ (high Cr phase) depletion rather than β depletion in the coating.

The thickness of the γ' depletion zone in the substrate decreases with increasing Ta concentration (Figure 5). The decrease in γ' depletion zone thickness with increasing Ta is due to the strong γ' forming capabilities of Ta. The exceptions were the high-carbon, tantalum-free substrates (A, E, and C). These substrates developed significantly lower γ' depletion zone thicknesses than the low-carbon, tantalum-free substrates. These thicknesses were similar to the high-carbon, tantalum-containing (3 wt.%) substrates. The decrease was due to the formation of the continuous

24
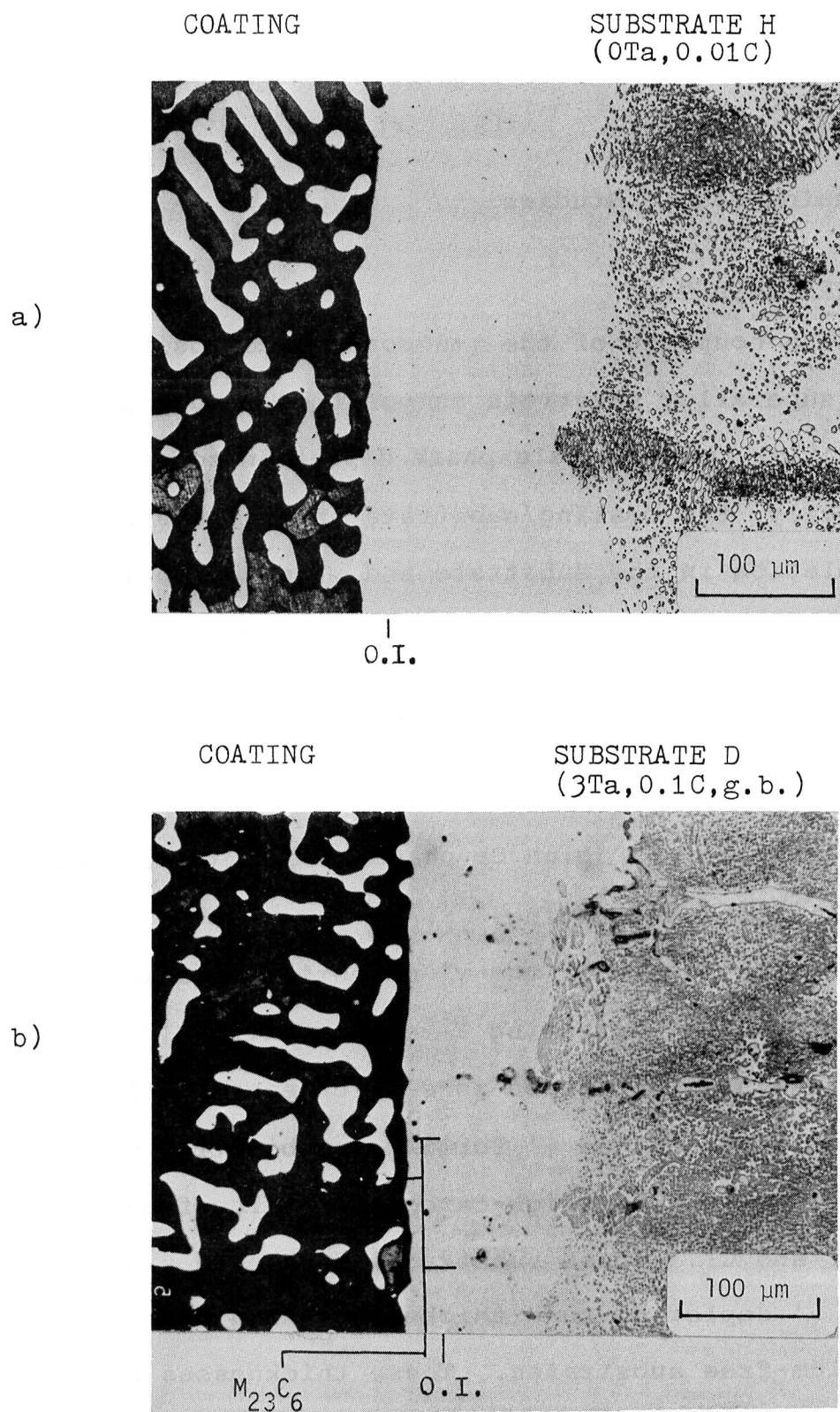
Figure 4. Microstructures of diffusion couples
   a)   Couple alloy H
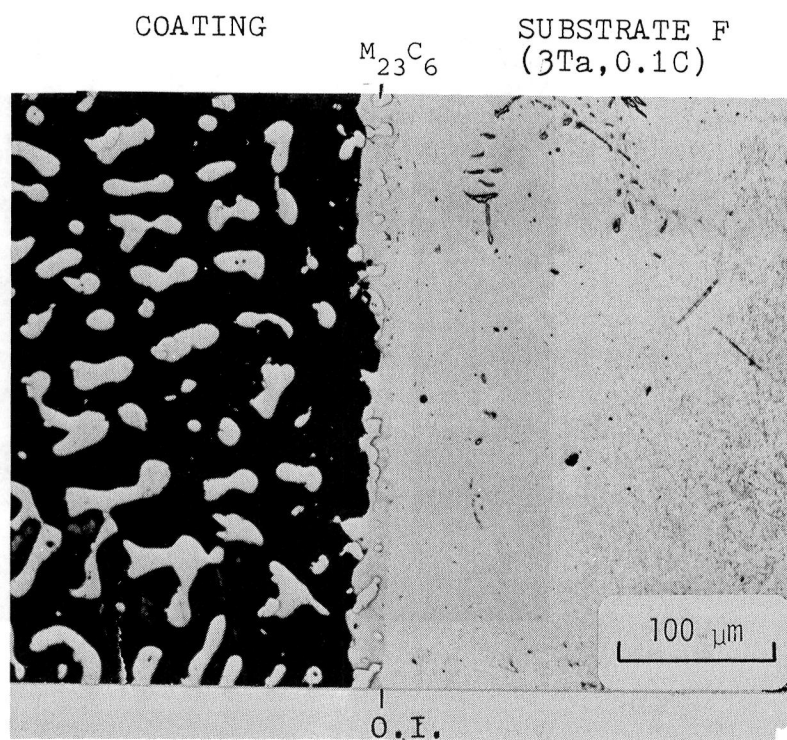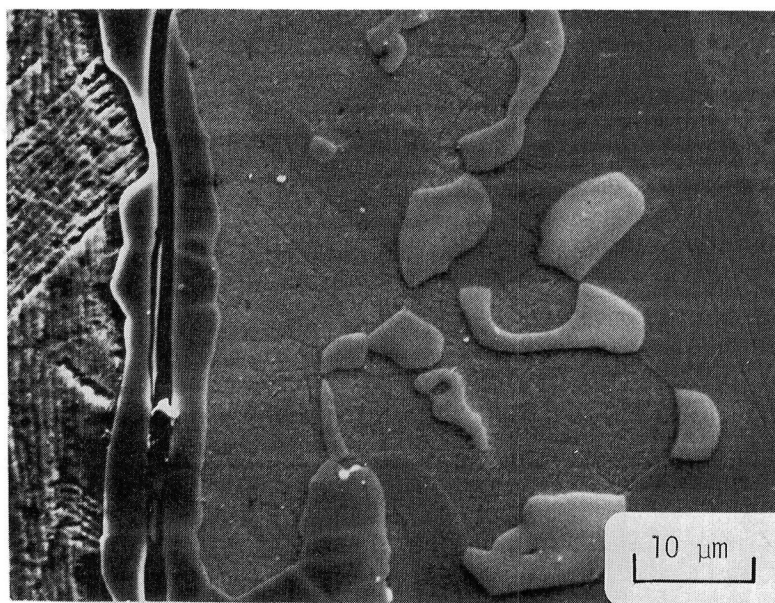   b)   Couple alloy D
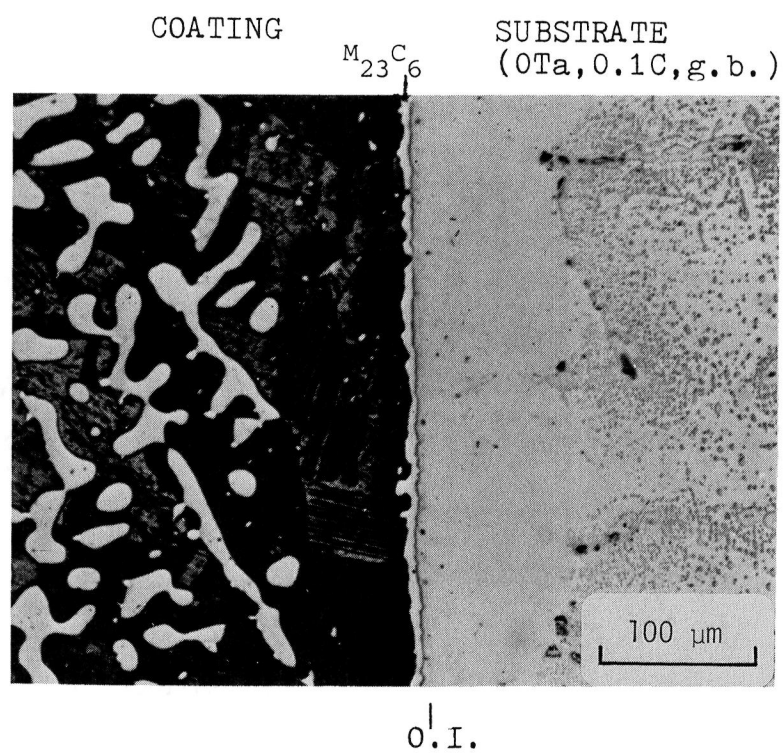
Figure 4.   Microstructures of diffusion couples (con't)
c) Couple alloy F
d) Couple alloy C
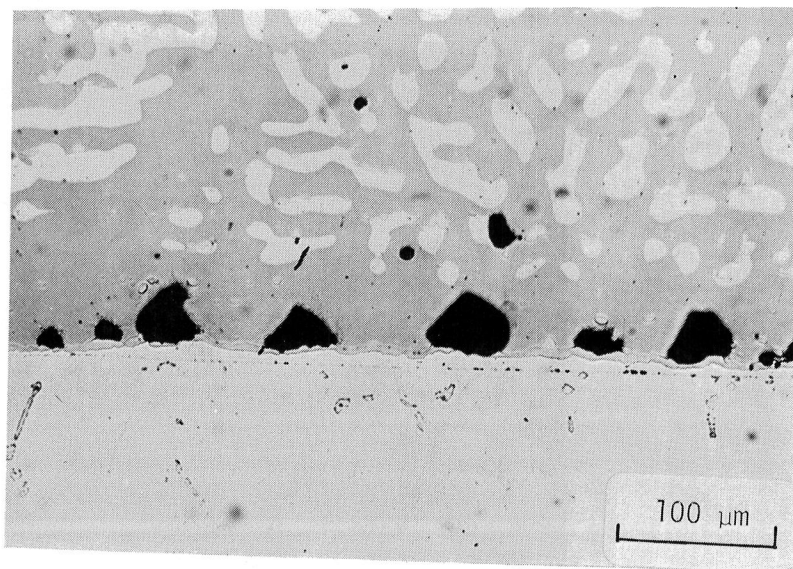
26

COATING $M_{23}C_6$ SUBSTRATE C
(0Ta,0.1C,g.b.)

e)

O.I.

10 μm

COATING

f)

100 μm

SUBSTRATE C

Figure 4.   Microstructures of diffusion couples (con't)
         e) Couple alloy C(crack in $M_{23}C_6$ carbide)
         f) Couple alloy C(Kirkendall porosity)

$M_{23}C_6$ carbide layer (see concentration/distance profile section). The thickness of the β-depletion zone in the coating was not affected by Ta concentration (Figure 5). This β depletion zone was also observed for the γ+β/γ Ni-Cr-Al system (24,28). Both the γ' (substrate) and β (coating) depletion zone thicknesses exhibited parabolic thickening (Figure 6).

Chromium-rich, $M_{23}C_6$ carbides were present in all diffusion zones for the couples with high-carbon substrates (Figures 4b-e). Generally, the carbides nucleated at the coating/substrate and γ+β/γ interfaces. However, scattered $M_{23}C_6$ particles were found in other locations in both the coating and substrate. The $M_{23}C_6$ carbides are predominately Cr with significant quantities of W (upto 15 wt.%). Continuous $M_{23}C_6$ carbides were present in all couples that contained high-carbon, tantalum-free substrates (A, C, and E). Cracks were observed in the continuous $M_{23}C_6$ carbides (Figure 4e). As shown in Figures 4b-d, the amount of $M_{23}C_6$ carbide decreased with increasing Ta concentration. The decrease is due to the strong carbide forming capabilities of Ta, which reduce the levels of C available in the matrix to form $M_{23}C_6$ carbides. The reduced carbon levels could be caused by increased M C carbide stability (Ta-containing carbide) or decreased matrix C soluability (51). Both the $M_{23}C_6$ particles and continuous $M_{23}C_6$ carbides were identified by X-ray diffraction.

Kirkendall porosity was observed in all diffusion couples. The porosity was predominately in the coating
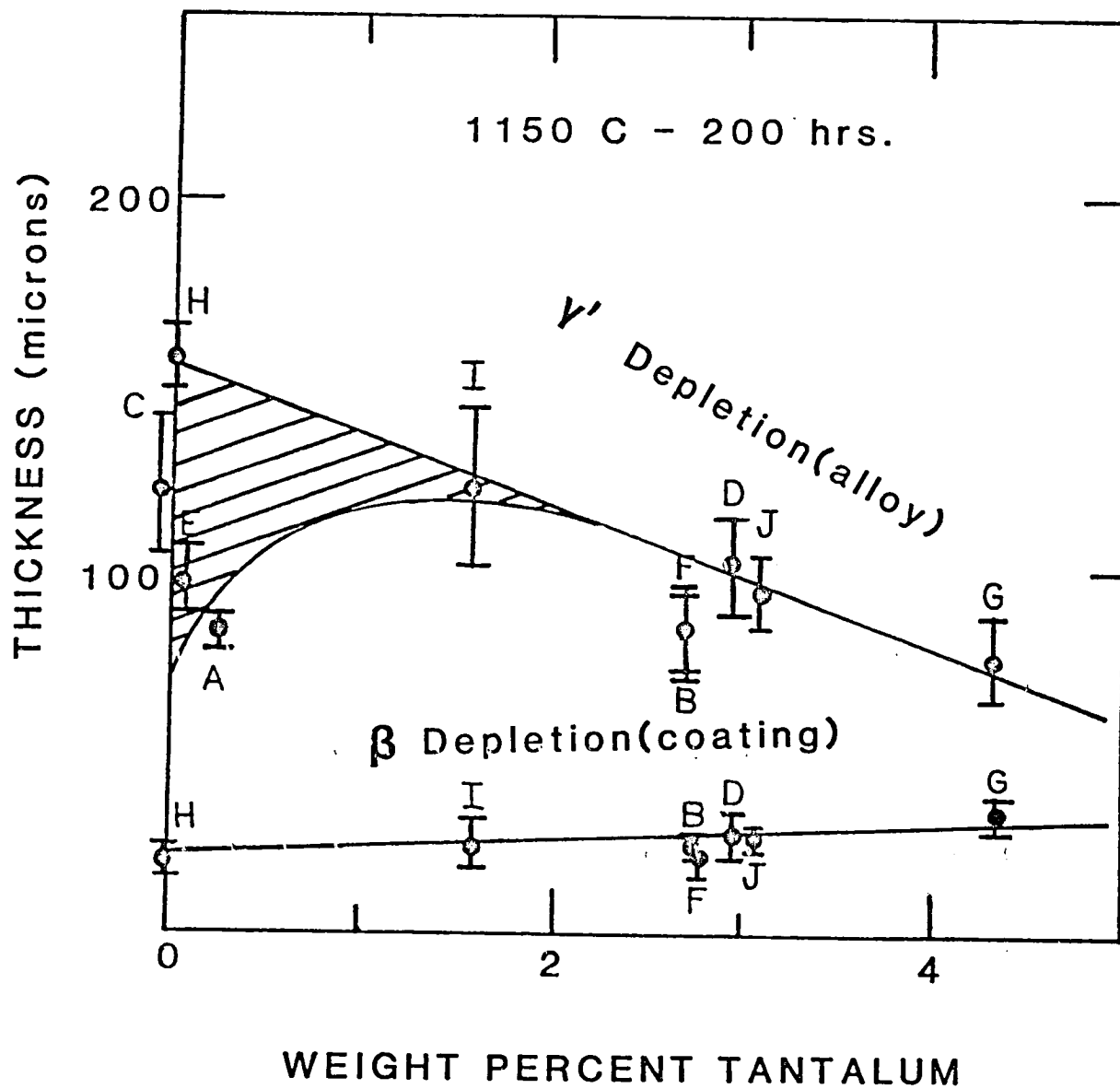
Figure 5.   Coating and substrate depletion zone
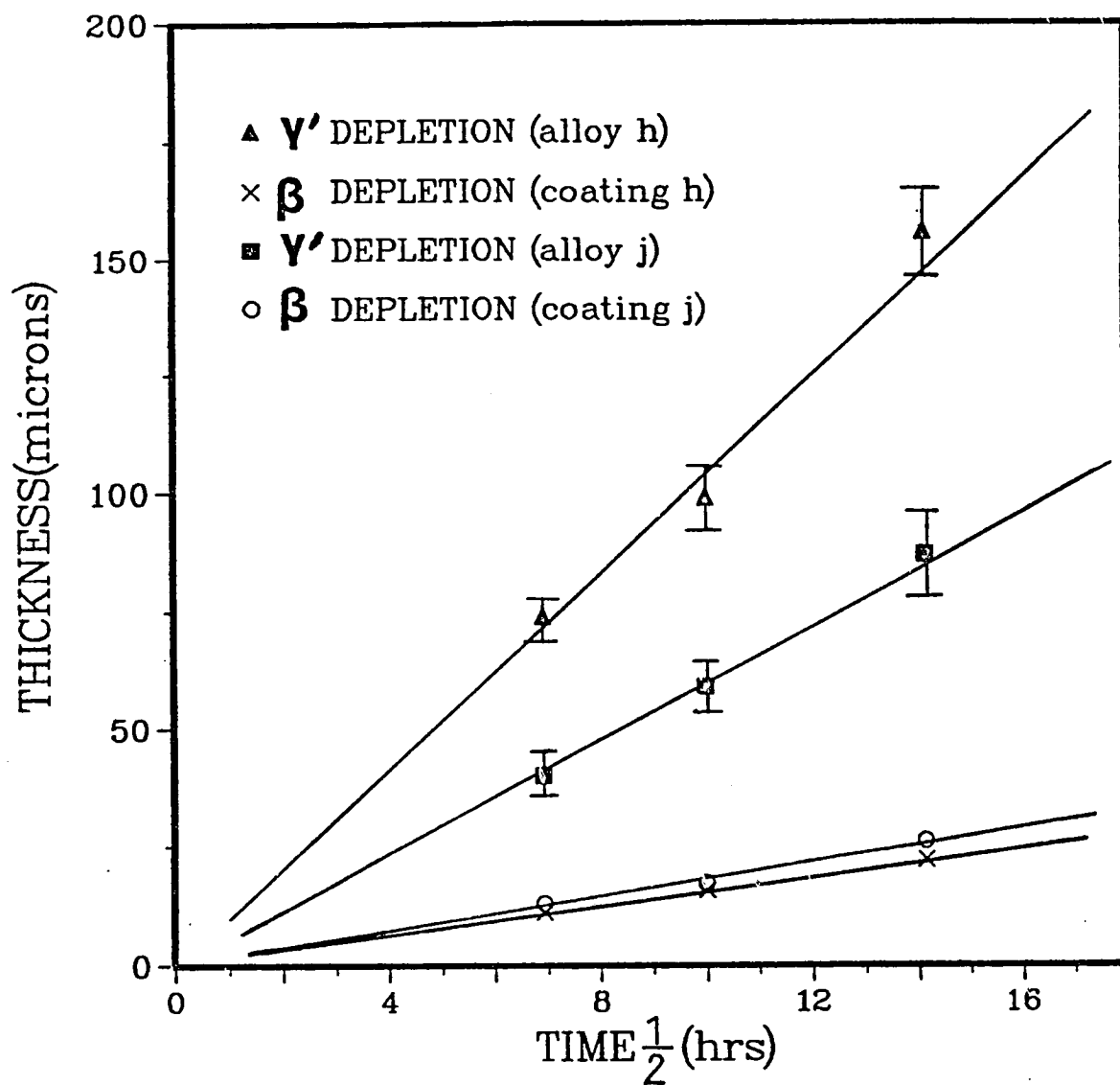   thicknesses in diffusion couples

Figure 6. Parabolic thickening behavior of coating and substrate depletion zone thicknesses for diffusion couples

composition section of the couple (Figure 4f). The porosity was greatest in the high-carbon, tantalum-free substrate couples.

Concentration/Distance Profiles

The concentration/distance profiles for all diffusion couples exhibited diffusion of the Cr up its concentration gradient (Figure 7a-f). The behavior was observed for $\gamma+\beta/\gamma$ couples in the Ni-Cr-Al system in a prior study (24). The uphill diffusion of Cr was caused by the diffusion cross terms (i.e., the effect of the Al gradient in transporting Cr up its own gradient). The cross term conclusion was verified by diffusion coefficient determination for the Ni-Cr-Al system (24).

The uphill diffusion of Cr resulted in the formation of $M_{23}C_6$ carbides in the diffusion couples containing high-carbon substrates (Figures 7c-f). The development of the continuous layers of $M_{23}C_6$ carbide in high carbon, tantalum-free substrates (C and E) resulted in limited interdiffusion of Al, Cr, Co, and W (Figures 7c and e). The limited interdiffusion resulted in smaller γ' depletion zone thicknesses than occurred in the low-carbon, tantalum-free substrate.
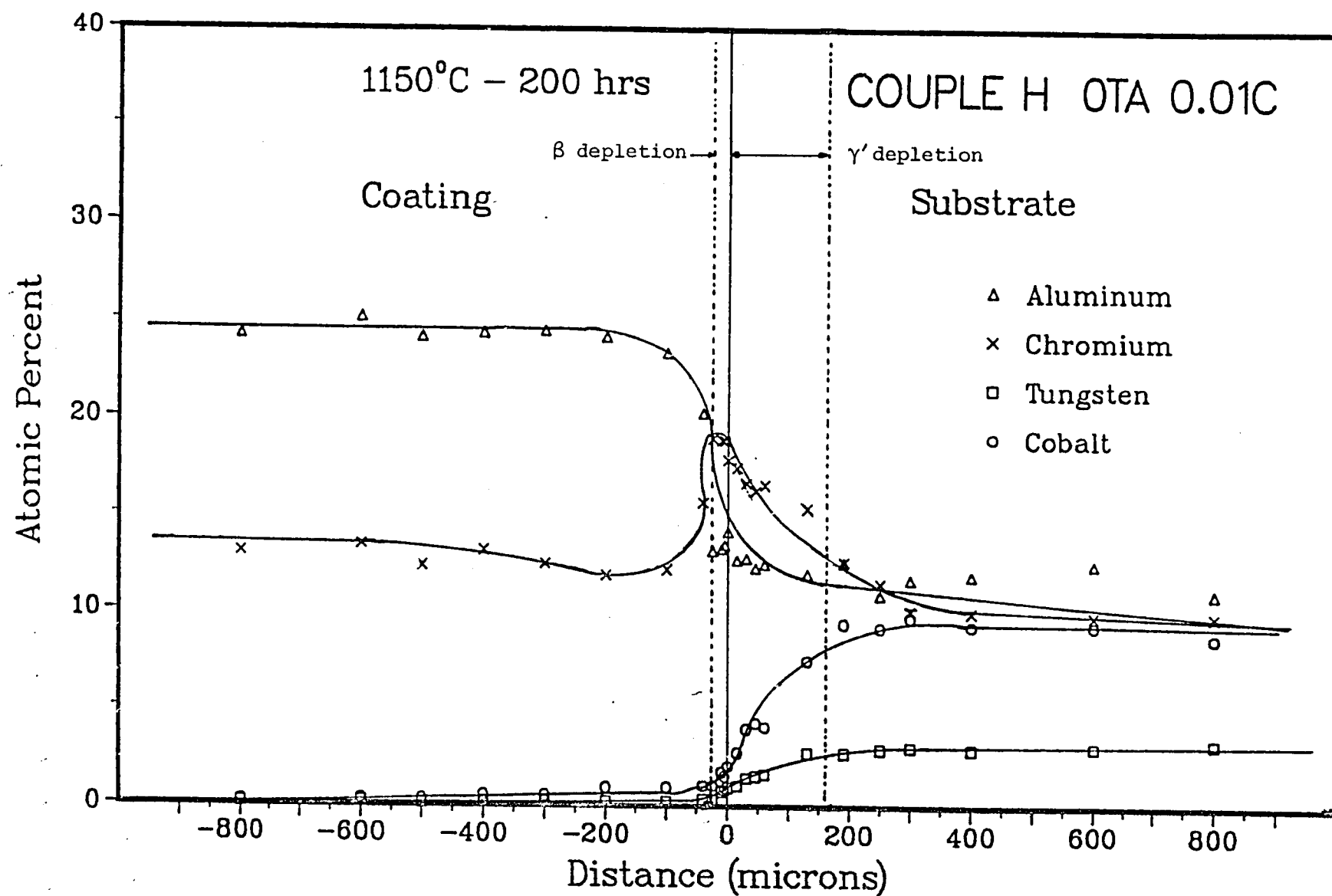
Figure 7   Concentration/distance profiles for diffusion couples
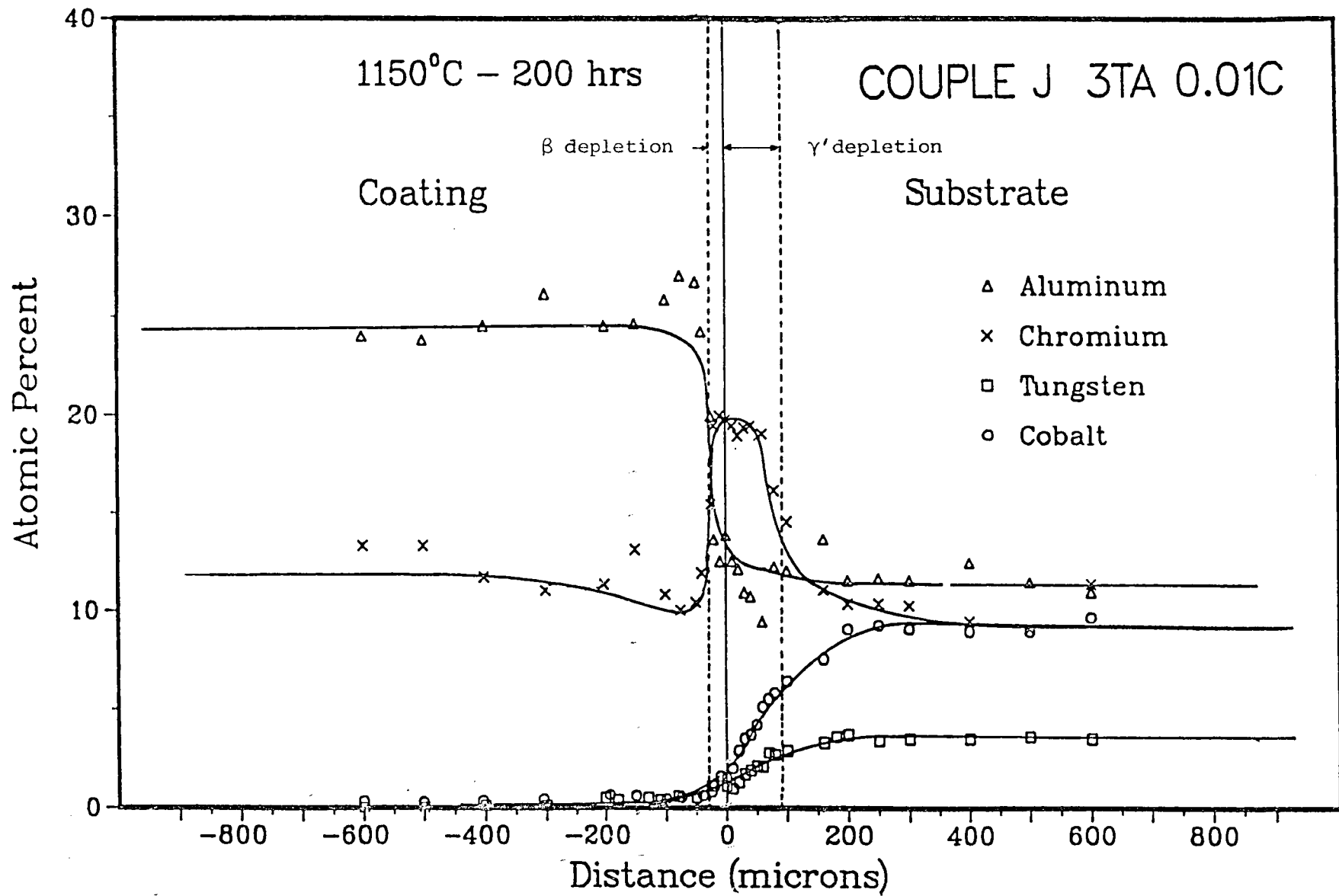   a) Couple alloy H -- 0 Ta, 0.01C

Figure 7   Concentration/distance profiles for diffusion couples
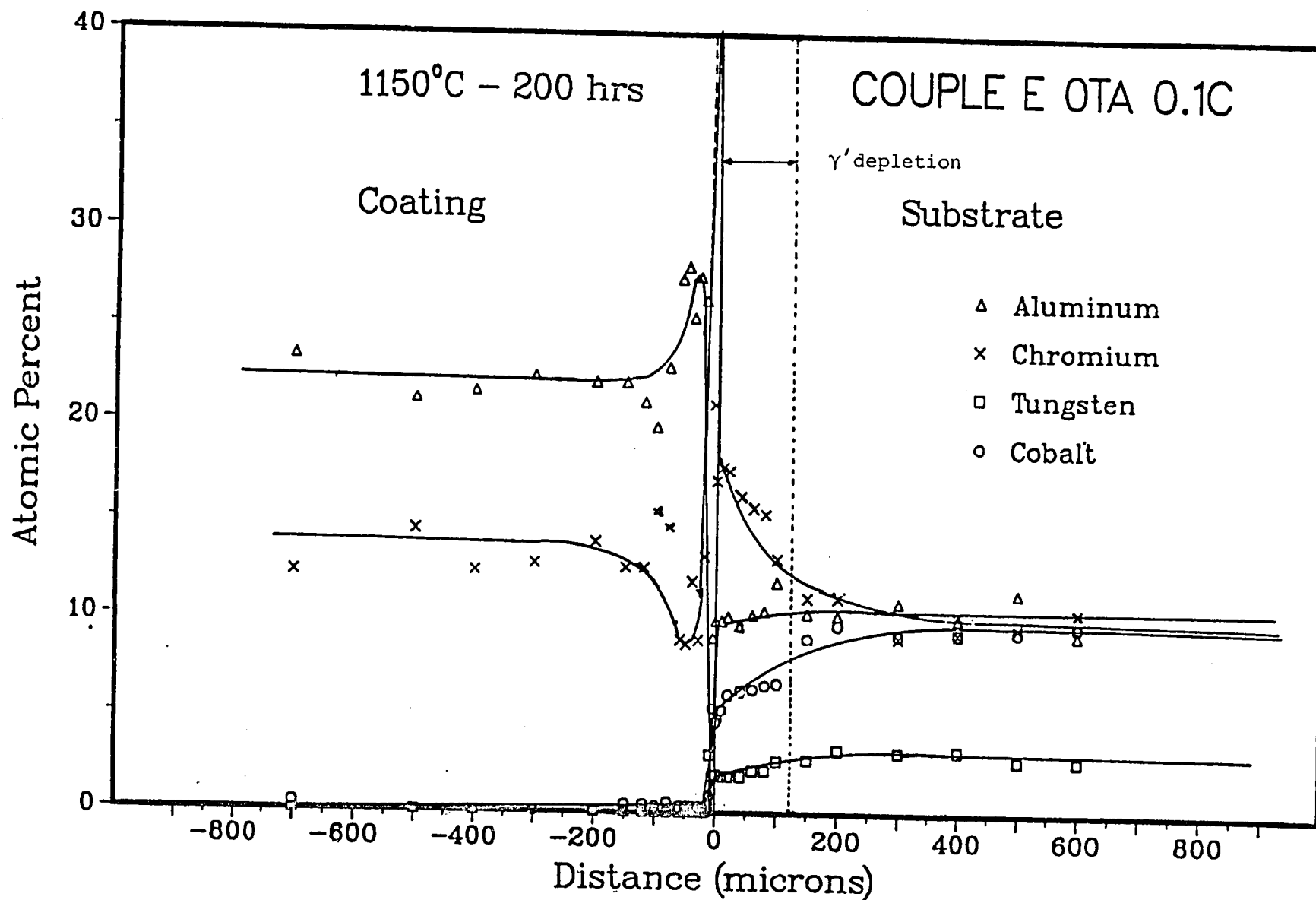b) Couple alloy J -- 3 Ta, 0.01C

Figure 7   Concentration/distance profiles for diffusion couples
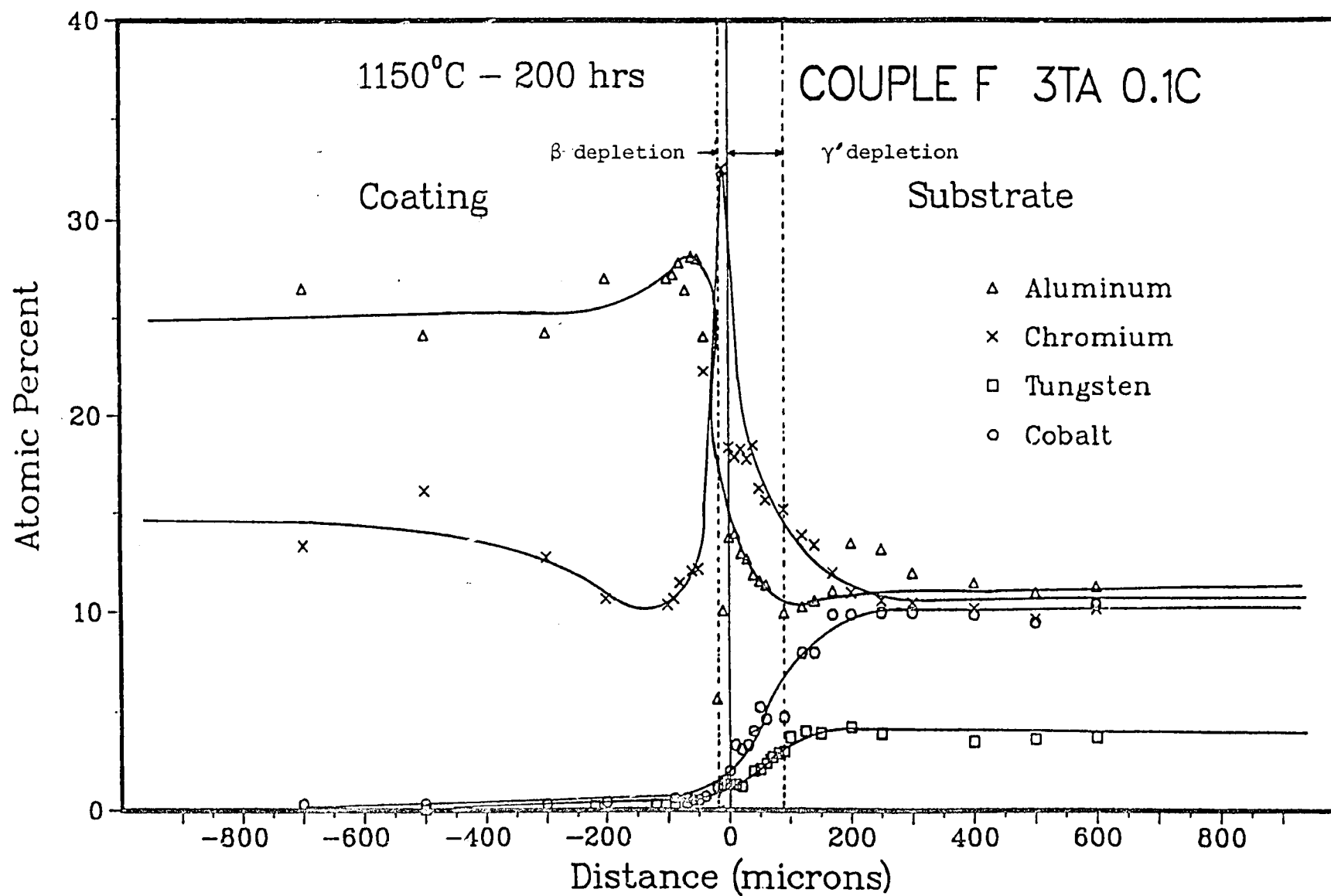c) Couple alloy E -- 0 Ta, 0.1C

Figure 7   Concentration/distance profiles for diffusion couples
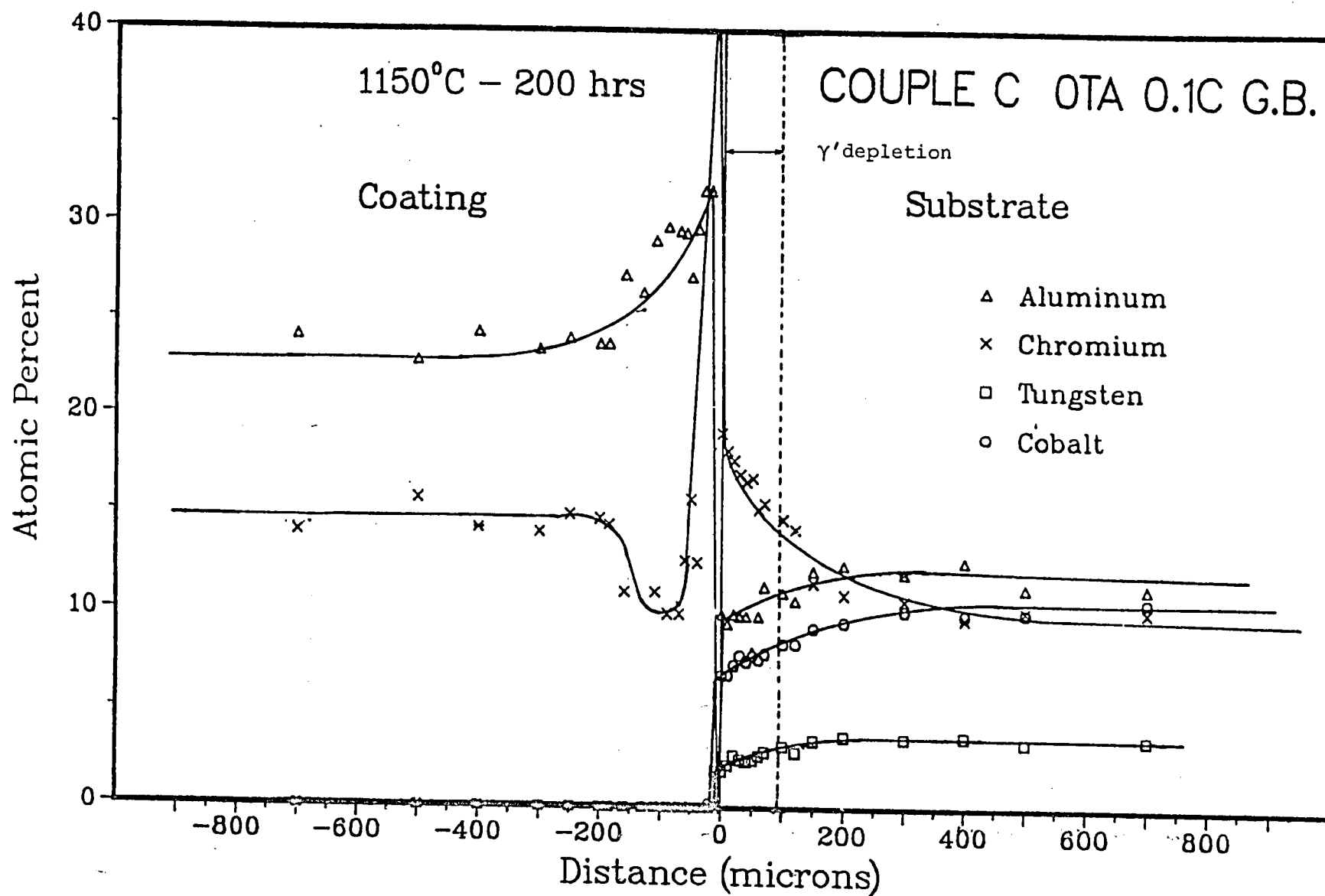d) Couple alloy F -- 3 Ta, 0.1C

Figure 7   Concentration/distance profiles for diffusion couples
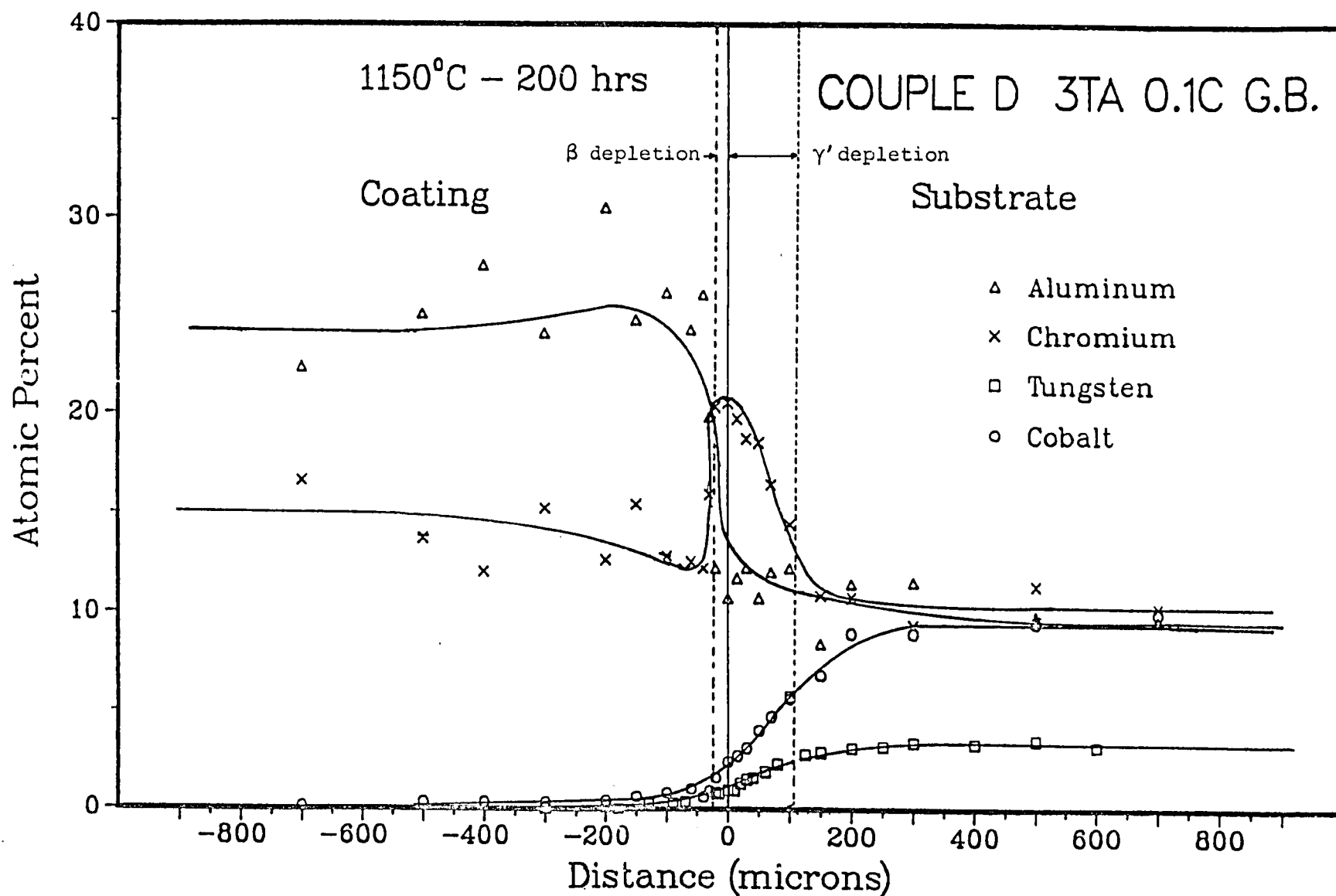   e) Couple alloy C -- 0 Ta, 0.1C, g.b.

Figure 7   Concentration/distance profiles for diffusion couples
f) Couple alloy D -- 3 Ta, 0.1C, g.b.

CYCLIC OXIDATION STUDIES

Change in Weight Curves (ΔWg)

The low-pressure, plasma-coated (LPPC) superalloy substrates (E, F, H, and J) without grain boundary strengthening elements (g.b.s.e.) exhibited similar ΔWg curves (Figure 8a). These curves were also similar to the ΔWg curve (Figure 8a) for the LPPC Ni10Cr10Al (nominal atomic percent) substrate studied by Nesbitt (24).

The LPPC superalloy substrates with g.b.s.e. (A, B, C, and D) exhibited ΔWg curves indicating higher oxidation resistance than LPPC superalloy substrates without these elements (Figure 8b). The improved oxidation resistance was caused by g.b.s.e. and larger coating thicknesses. The improved oxidation resistance caused by increased coating thicknesses for LPPC substrates without g.b.s.e. is shown in Figure 8c.

Significant macrospalling occurred for all LPPC substrates after 200 cycles (Figure 8b). Macrospalling was due to the coating overlap which is a by-product of the coating process. The overlap resulted in premature macrospalling of the coating at the ends (Figure 9). Unfortunately, the significant macrospalling at later cycle times limits the application of ΔWg curves to separate active element and coating thickness improvements on oxidation resistance for thicker coatings.

The presence of the continuous $M_{23}C_6$ carbide can result in premature macrospalling of the coating. Premature macrospalling occurred for high-carbon, tantalum-free LPPC substrate E at 75 cycles in one case. The result was macrospalling of the end
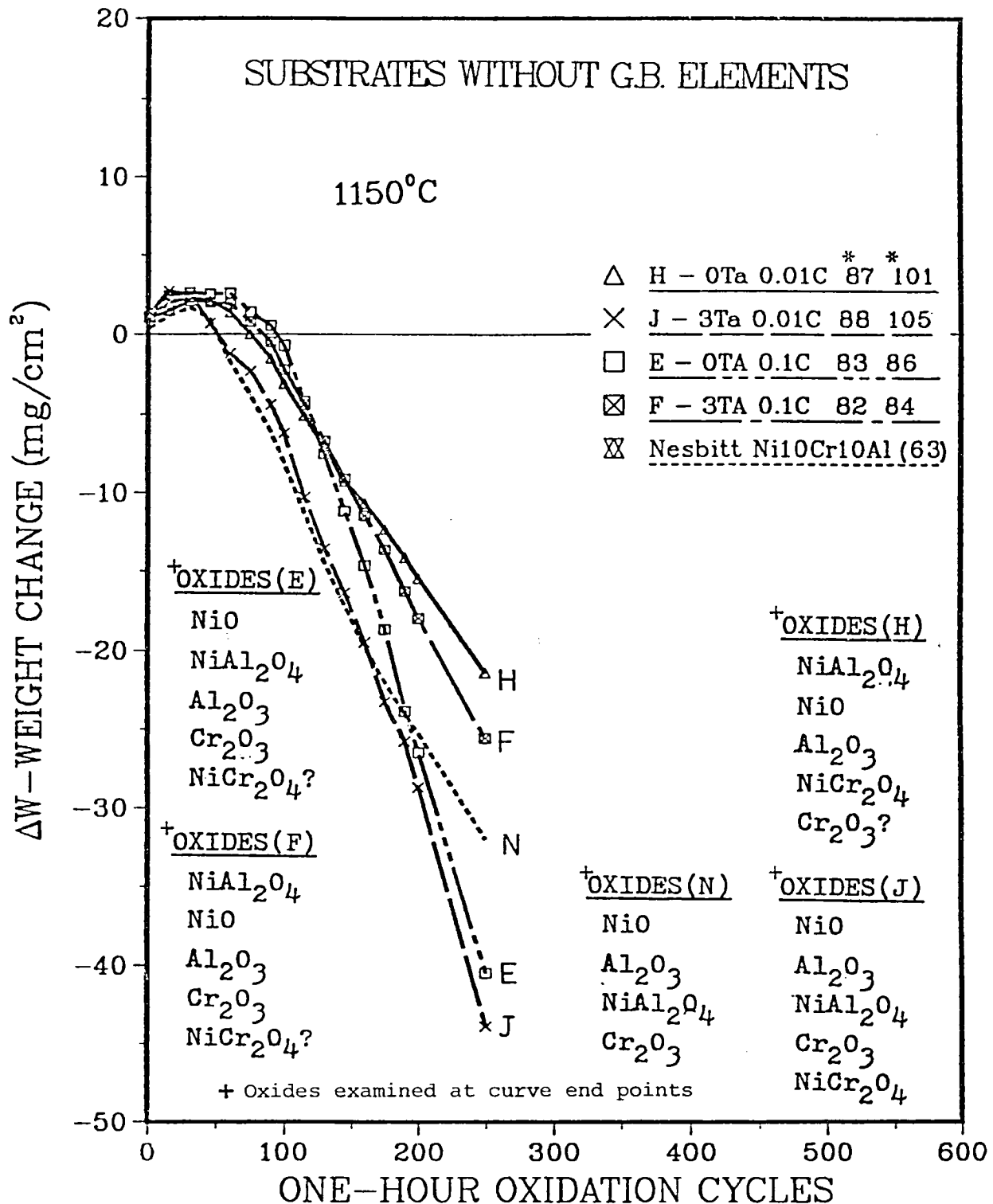
Figure 8. Change in weight curves (Wg) for low pressure
plasma coated substrates (LPPC). *Minimum
coating thickness, average coating thickness —
(see procedure for complete description)
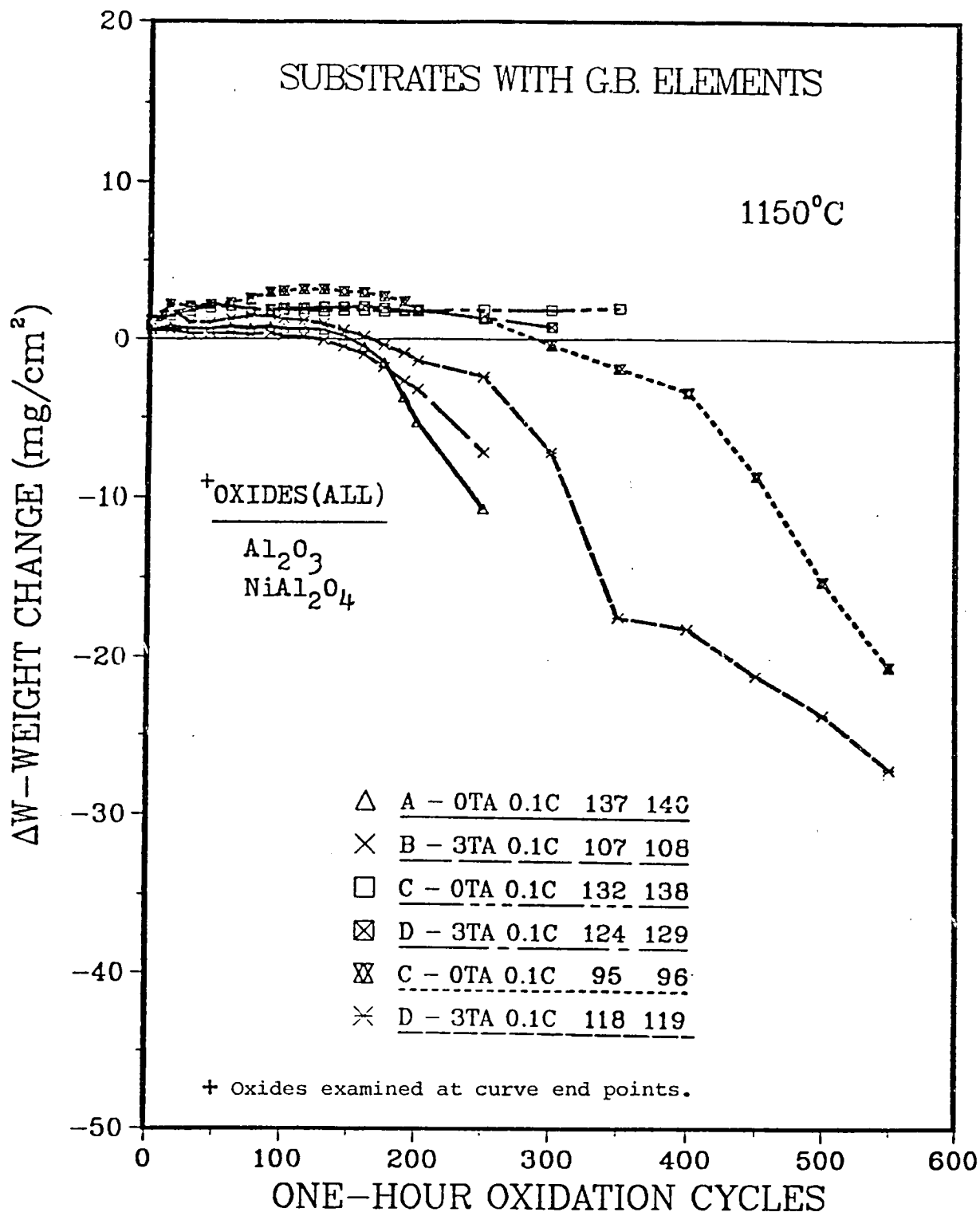a) Substrates without g.b. elements

Figure 8. Change in weight curves (ΔWg) for the low pressure
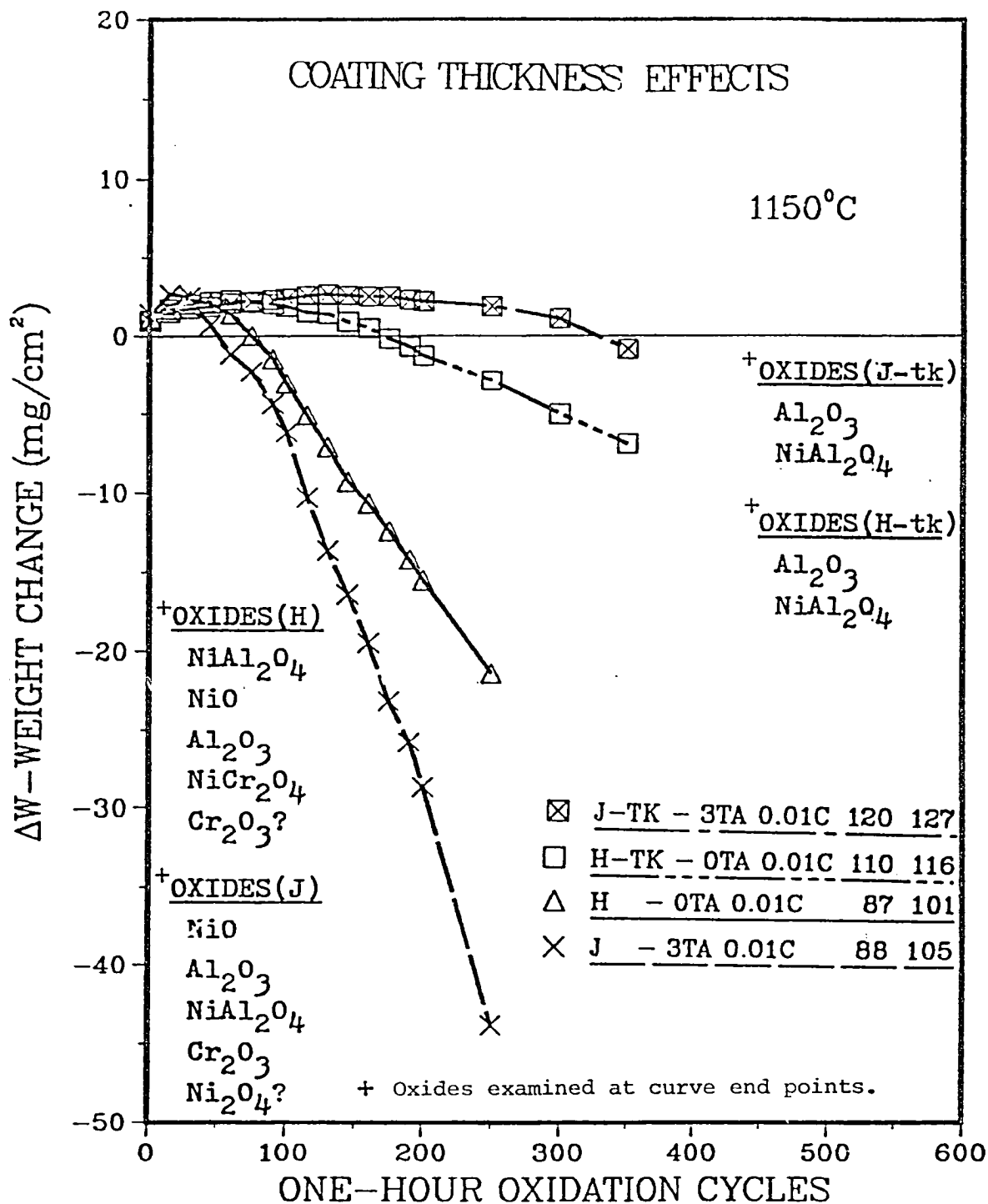plasma coated substrates (LPPC) (con't)
b) Substrates with g.b. elements

Figure 8. Change in weight curves (ΔWg) for the low pressure
plasma coated substrates (LPPC) (con't)
c) Coating thickness effects

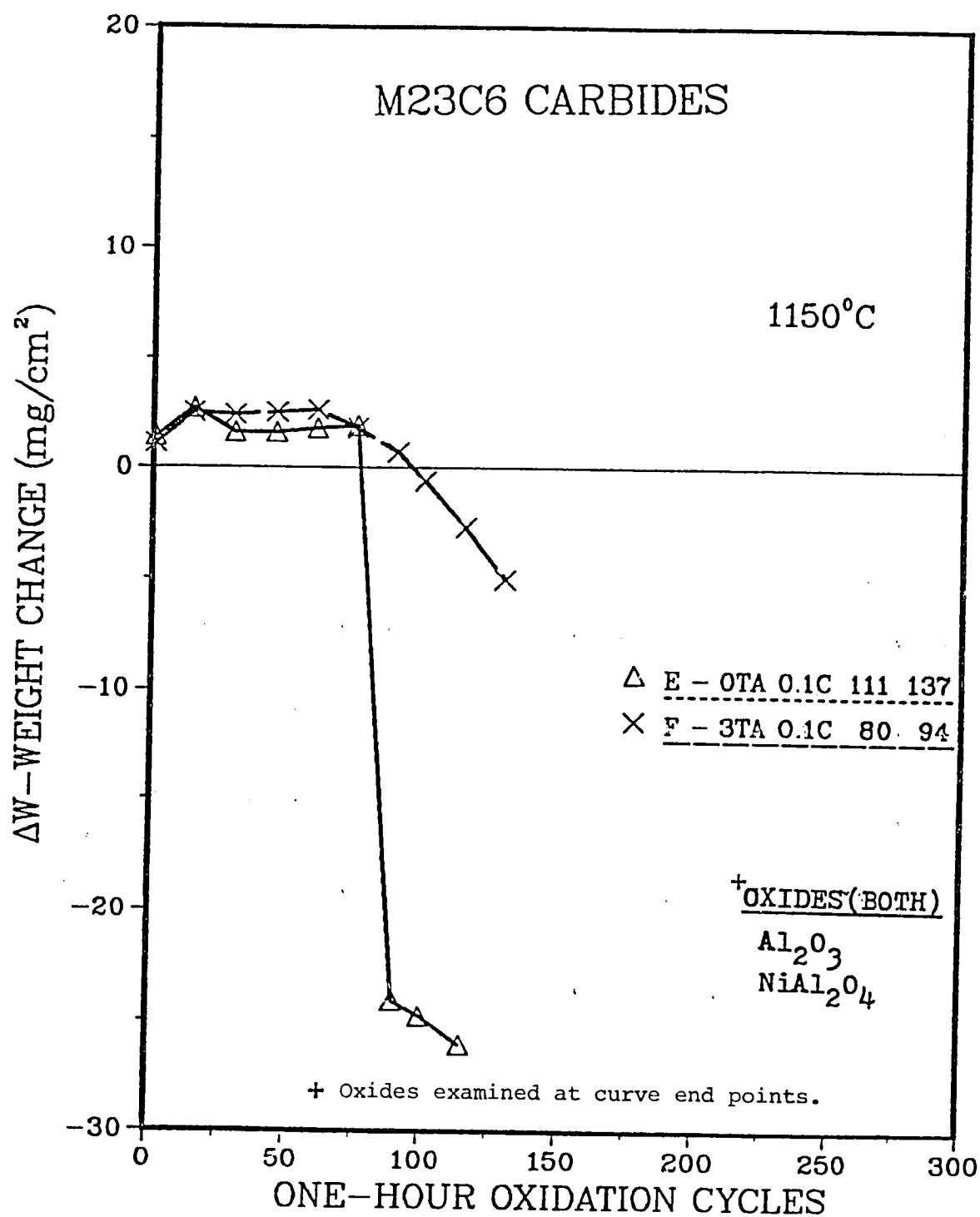Figure 8. Change in weight curves (ΔWg) for the low pressure plasma coated substrates (LPPC) (con't) d) $M_{23}C_6$ carbide effects

42

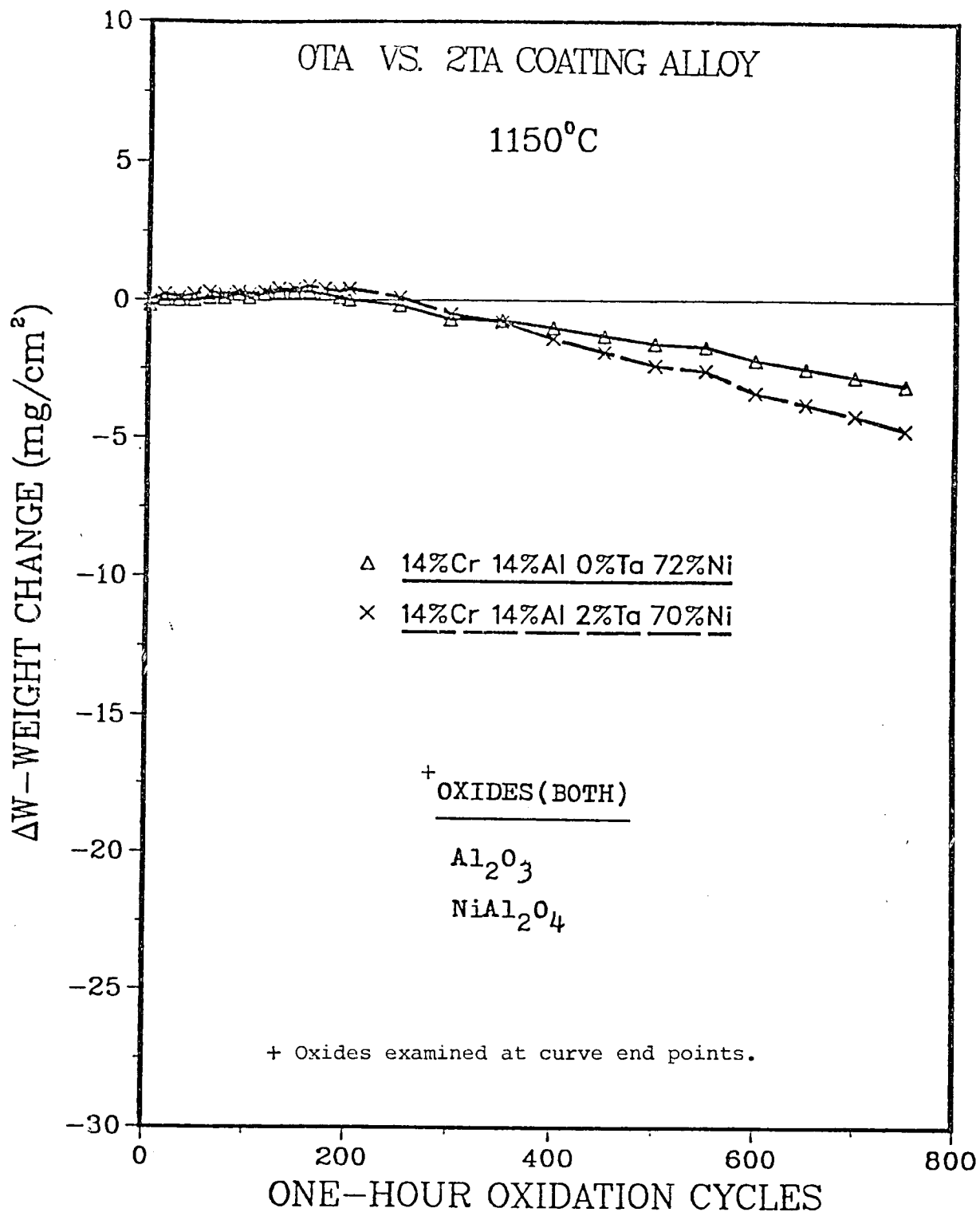
Figure 8. Change in weight curves (ΔWg) for the low pressure
plasma coated substrates (LFPC) (con't).
e) 0 Ta vs. 2 Ta coating alloy
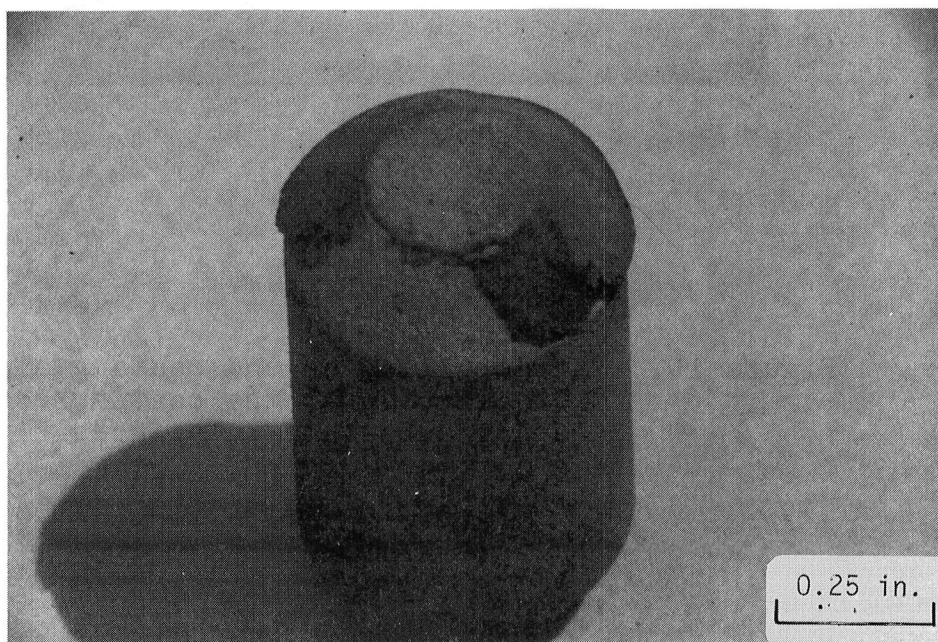
a)
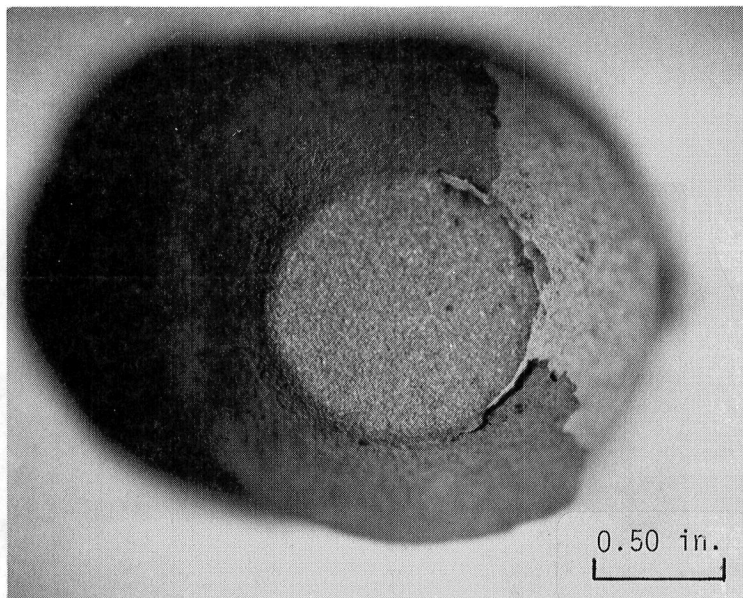
b)

Figure 9.   Macrospalling of the end of the coating
            (LPPC substrate D at 350 cycles)
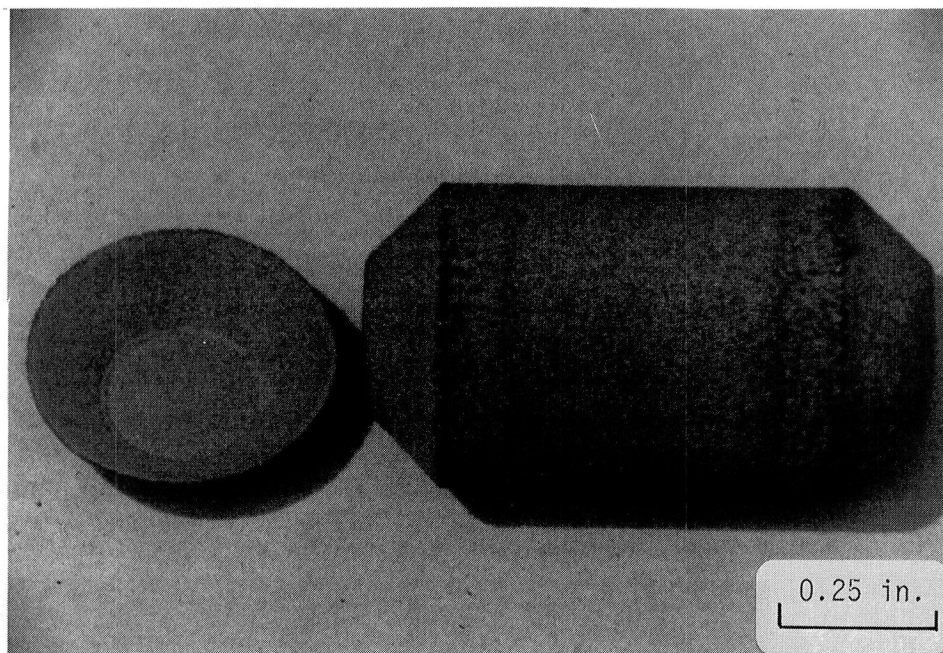   a) End section view
            b) Entire section view

Figure 10. Macrospalling of end coating along continuous $M_{23}C_6$ carbide at the coating/coating and coating/substrate interfaces

coating (Figure 10). The failure was linked directly to the formation of continuous $M_{23}C_6$ carbides at both the coating/substrate and coating/coating interfaces in the specimen. Macrospalling of the end coating was the cause of the large weight loss in Figure 8d (compared to LPPC substrate F, normal behavior).

The oxidation resistance was not affected by adding 2 wt.% Ta directly to a coating alloy. Two coating alloys (alloy produced by vacuum arc melting the coating powder) were produced to eliminate the effects of coating thickness and macrospalling. Alloy 2Ta contained the same composition as the coating except that 2 wt.% Ta (0.7% atomic) was added. Alloy 0Ta contained the same composition as used in the couples. The identical ΔWg curves (Figure 8e) indicate that the oxidation resistance of the two coating alloys was similar.

Surface Oxides

The protective surface-oxide scale (Figures 11a,b) that was present on all LPPC substrates at short cycles times (50 cycles) was Al_2O_3 and $NiAl_2O_4$ (spinel). Recent studies indicate that the combination of these oxides provide excellent oxidation resistance (13,19). These oxides were replaced by NiO and other less protective oxides when the coating/substrate specimen was unable to supply the required Al flux. The formation of these less protective oxides indicate the onset of breakaway oxidation.

The LPPC superalloy substrates with thinner coatings

a)
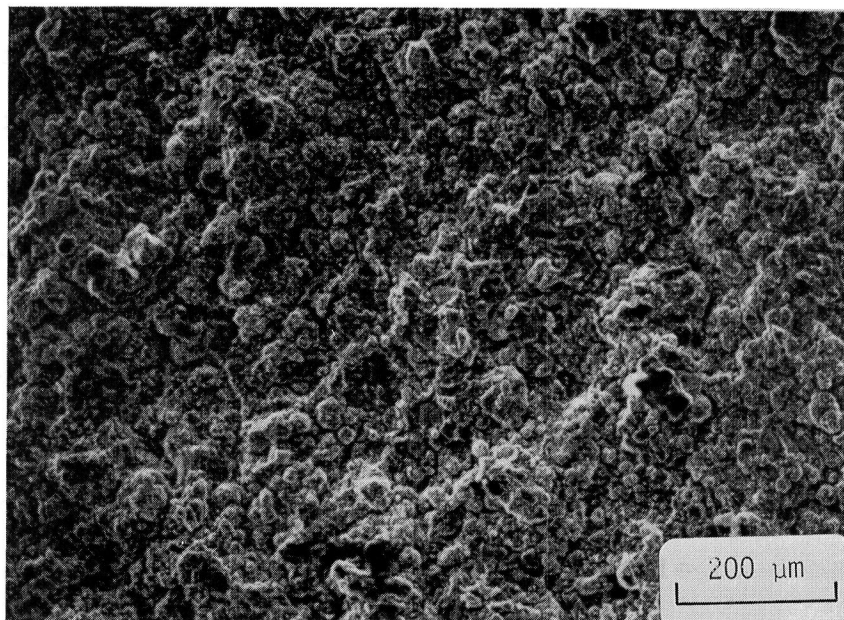
b)

Figure 11. Surface oxide morphologies for LPPC
substrates

a,b) LPPC substrate at 50 cycles(Ex. LPPC
substrate J)
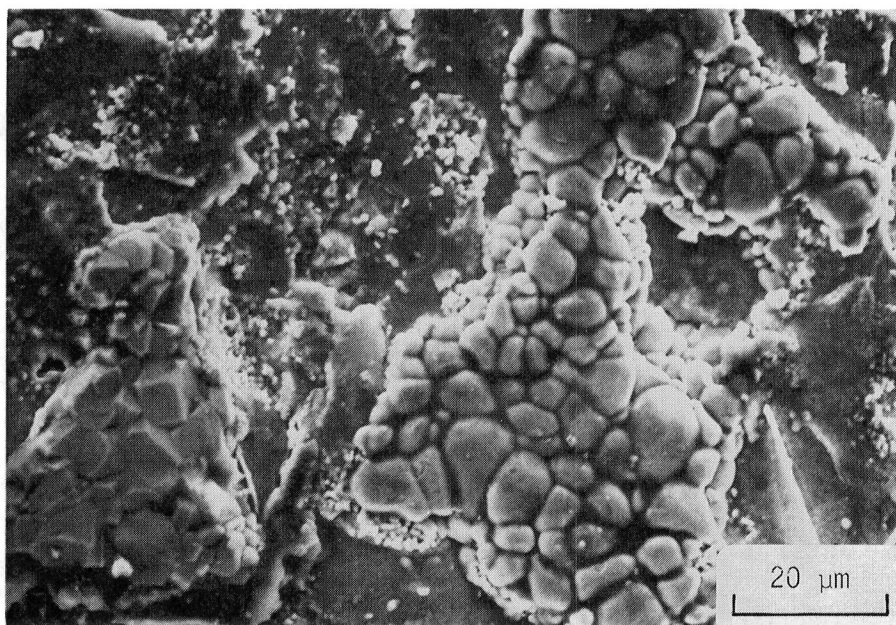
Figure 11. Surface oxide morphologies for LPPC
substrates (con't)

c,d) LPPC substrate with less protective
oxides. Note: the presence of both
faceted and unfaceted NiO (Ex. LPPC
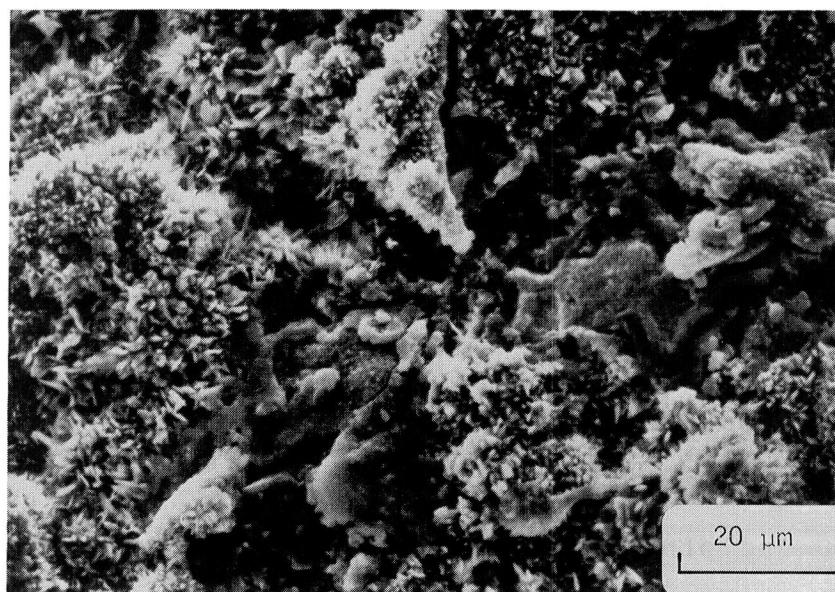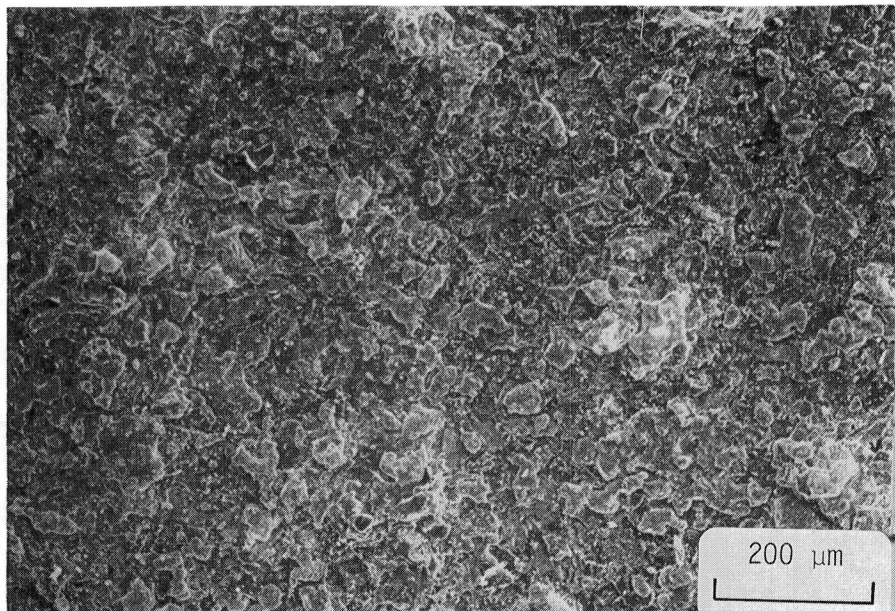substrate E-250 cycles)

e)
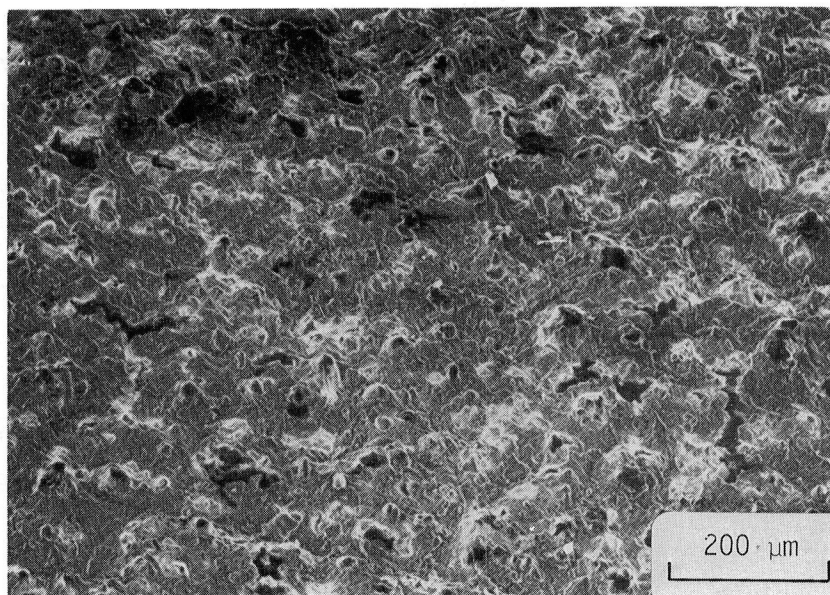
f)

Figure 11. Surface oxide morphologies for LPPC
substrates (con't)

e,f) LPPC substrate at 550 cycles(Ex. LPPC
substrate C)

g)
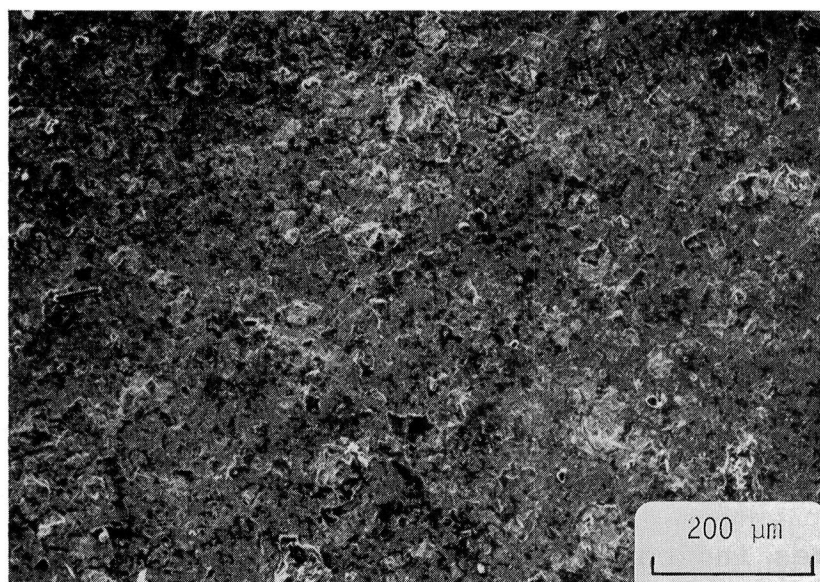
h)

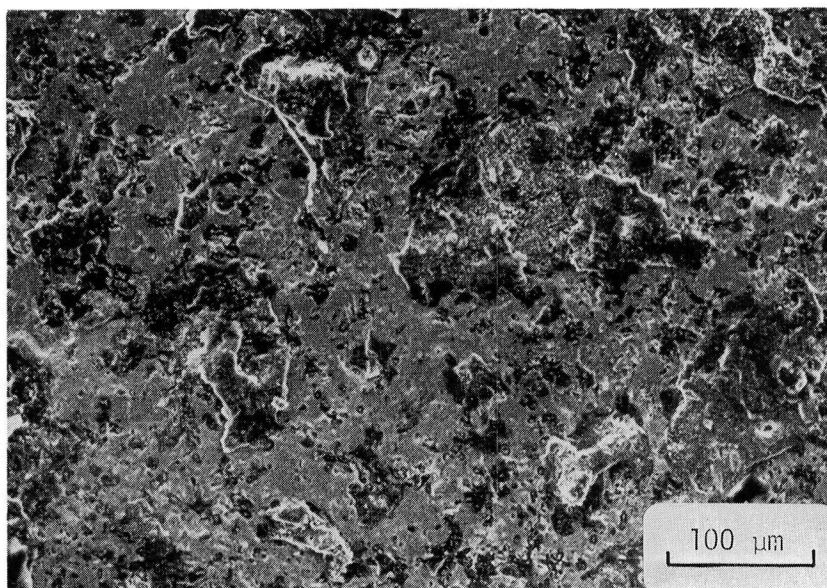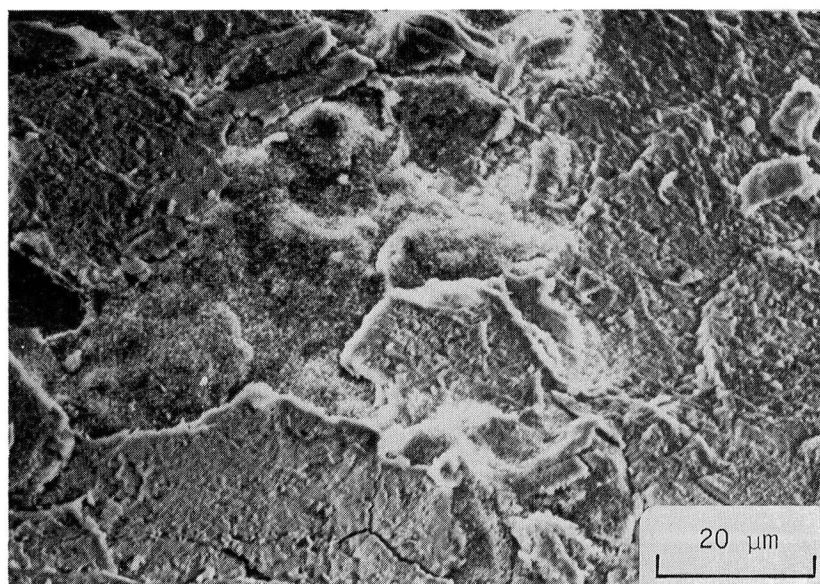Figure 11. Surface oxide morphologies for LPPC
substrates (con't)

g,h) 2Ta coating alloy at 750 cycles

($\approx$85μm) without g.b.s.e. at 250 and 350 cycles had predominately NiO and other less protective oxides (Figure 11c,d). These less protective oxides were also present on the LPPC Ni10Cr10Al substrate at the 250 cycle point (24). The presence of these less protective oxides indicates that breakaway oxidation was occurring for both cases at 250 cycles.

The LPPC superalloy substrates with g.b.s.e. had the more protective Al_2O_3 and $NiAl_2O_4$ scale at all cycle times (Figure 11e,f). The presence of the protective oxides at later cycle times indicates higher oxidation resistance than the LPPC substrates without g.b.s.e.

Larger coating thicknesses (greater than 110μm) resulted in the presence of the protective oxide scale at all cycle times. The continued presence of the protective oxides in the LPPC substrates without g.b.s.e. (H and J) at 350 cycles demonstrated the improved oxidation resistance of thicker coatings. The two coating alloys also had the protective scale through 750 cycles. The presence of almost exclusively Al_2O_3 with small quantities of $NiAl_2O_4$ in these alloys indicates the effects of an "infinite" coating thickness. The highly adherent scale is shown in Figure 11g,h.

Microstructure

The coating and diffusion effected substrate zone underwent several microstructural changes during the degradation process (Figures 12c-e, follow the degradation process step by step). The high-Al β phase was still present in the coating in all LPPC substrates at the 50 cycle point (Figures 12a-c). However, β depletion had occurred at the coating surface and at the coating/substrate interface. The β depletion resulted in single phase γ at the surface and γ+γ' at the coating/substrate interface. Continued oxidation and interdiffusion resulted in the remaining γ+β transforming to a coarse γ+γ' structure (Figures 12d, f, h, i, and k). As the coating approaches breakaway oxidation, the coating, and substrate adjacent to the coating/substrate interface transformed to single phase γ (Figures 12e, g, and j). These transformations were indicative of the large Al demand required by the oxide scale.

The β depletion zone thickness (interdiffusion) decreased with increasing Ta (Figure 13). Pennisi and Gupta (10) observed increases in the β volume fraction in the as-sprayed microstructure when Ta was added to the Ni-Cr-Co-Al-Y coating composition. Based on these results, the decrease in β depletion was due to the change in phase equilibria of the γ+β structure.

The formation of the less protective oxides resulted
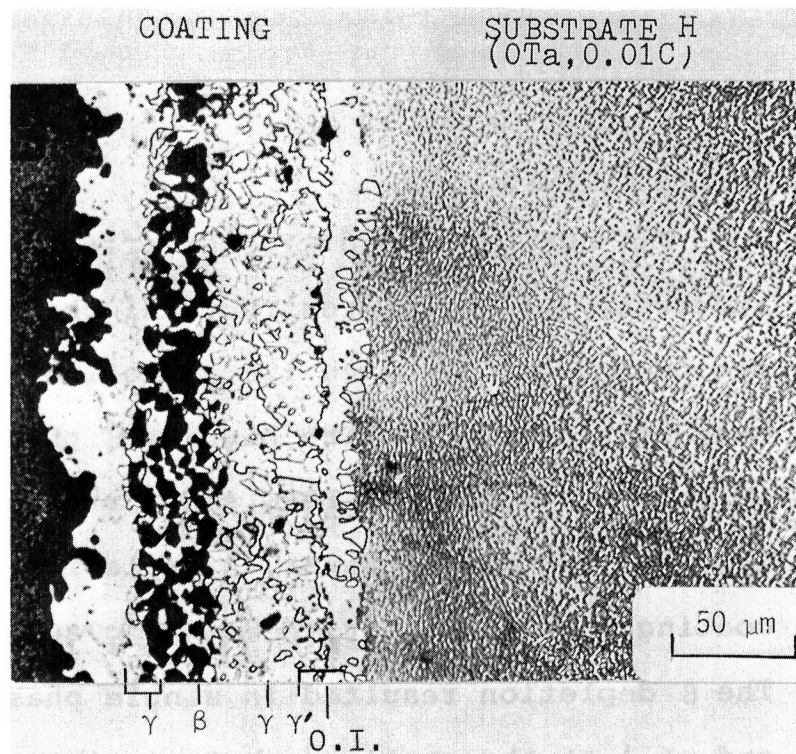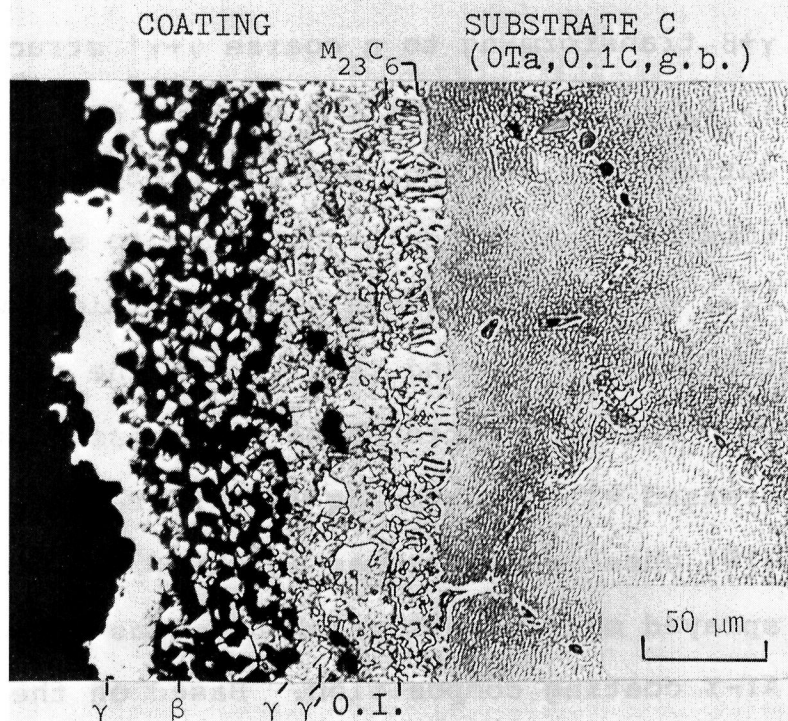
Figure 12. Microstructure of oxidized LPPC substrates
a) LPPC substrate H at 50 cycles
b) LPPC substrate C at 50 cycles

COATING   SUBSTRATE F
                    (3Ta,0.1C)

c)

50 μm

50 cycles

d)

50 μm

130 cycles

e)

50 μm
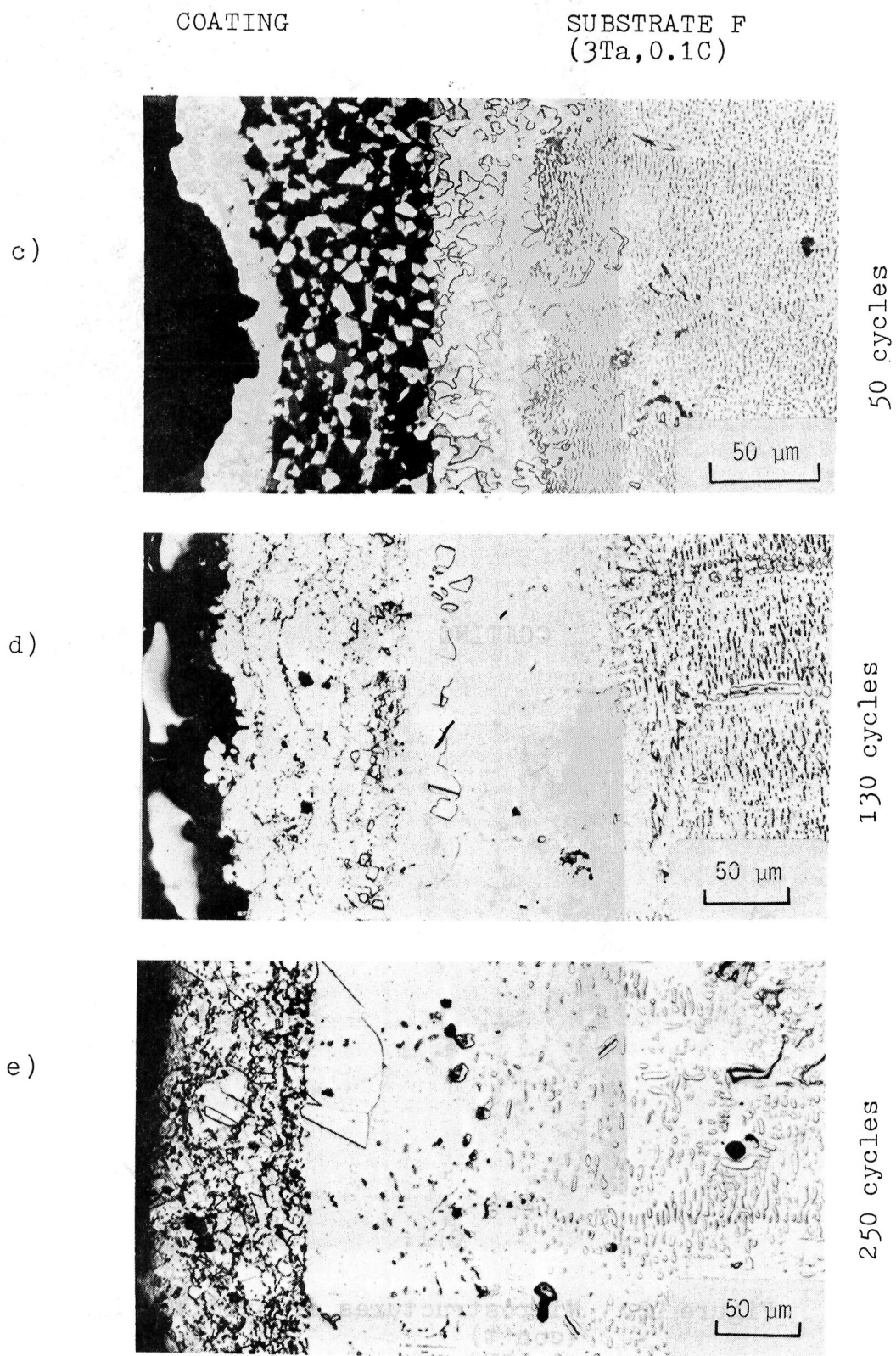
250 cycles

Figure 12. Microstructures of oxidized LPPC substrates
             (con't)
          c) LPPC substrate F at 50 cycles
          d) LPPC substrate F at 130 cycles
          e) LPPC substrate F at 250 cycles

54

Figure 12.   Microstructures of oxidized LPPC substrates
             (con't)
             f) LPPC substrate E at 115 cycles
             g) LPPC substrate E at 250 cycles
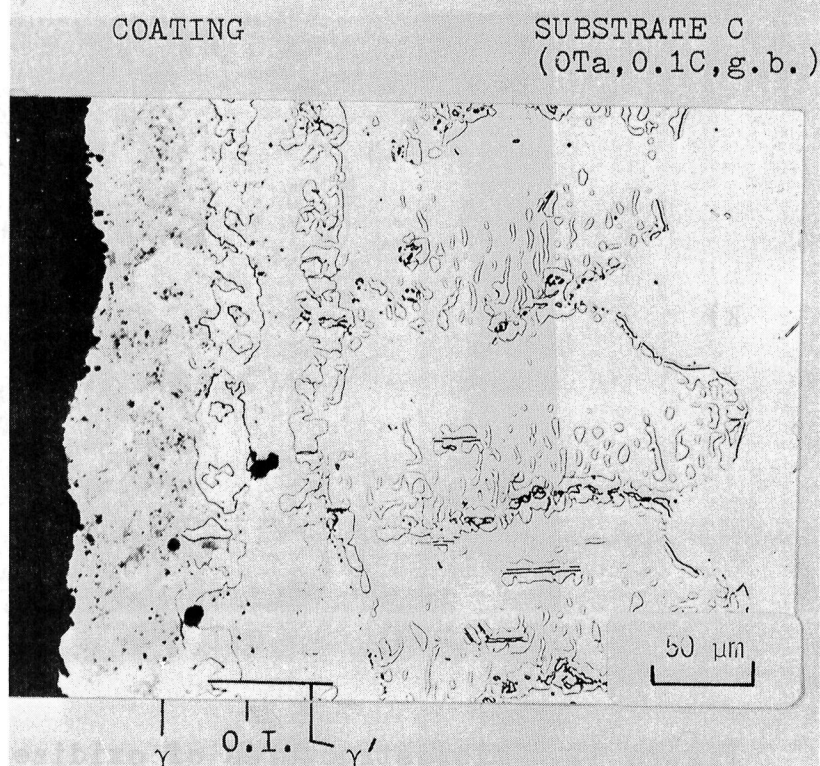
Figure 12.   Microstructures of oxidized LPPC substrates
             (con't)
             h) LPPC substrate C at 350 cycles
             i) LPPC substrate C at 550 cycles

56

COATING   SUBSTRATE H
                                 (0Ta,0.01C)

j)

50 µm

γ   O.I.
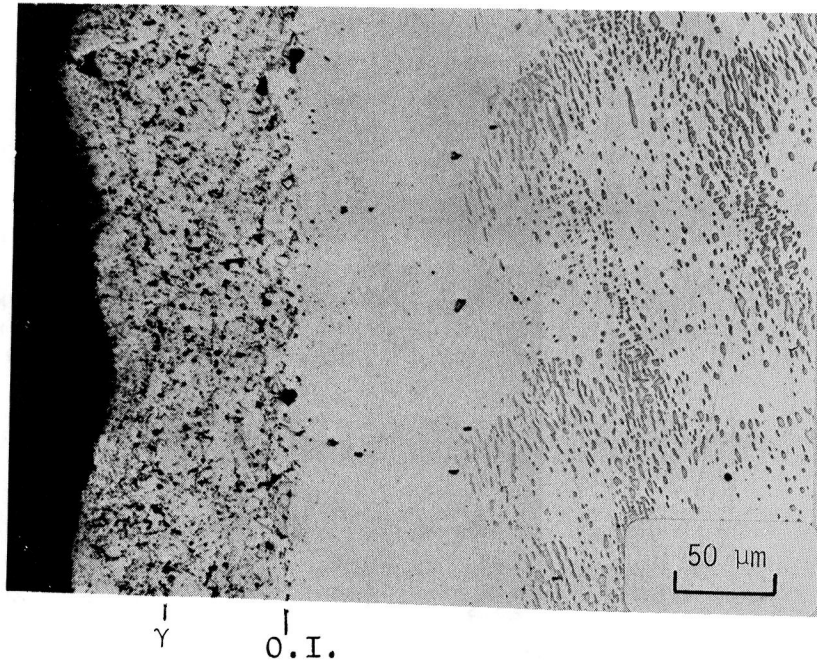
COATING   SUBSTRATE H
                                 (0Ta,0.01C)

k)

50 µm

γ   γ' O.I.
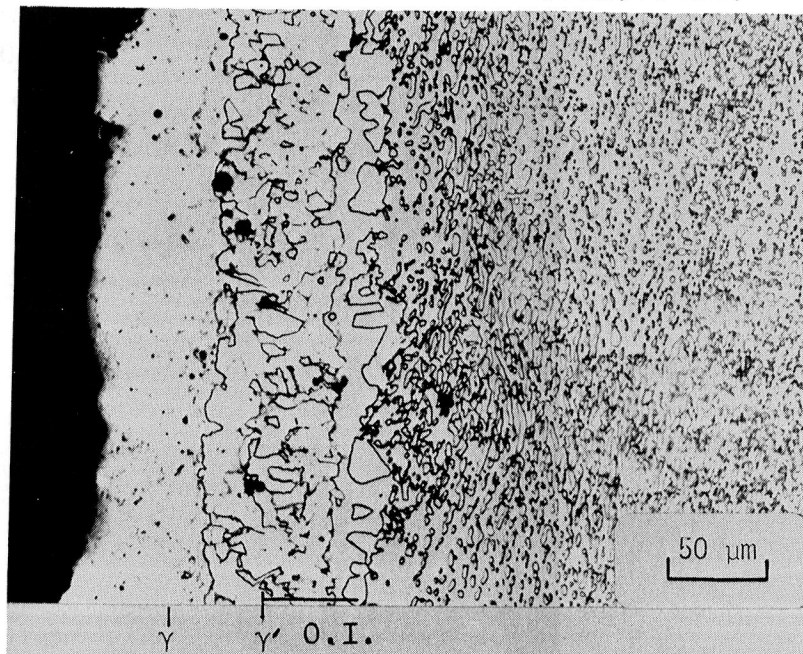
Figure 12.   Microstructures of oxidized LPPC substrates
                 (con't)
                 j) LPPC substrate H at 250 cycles (thin coat)
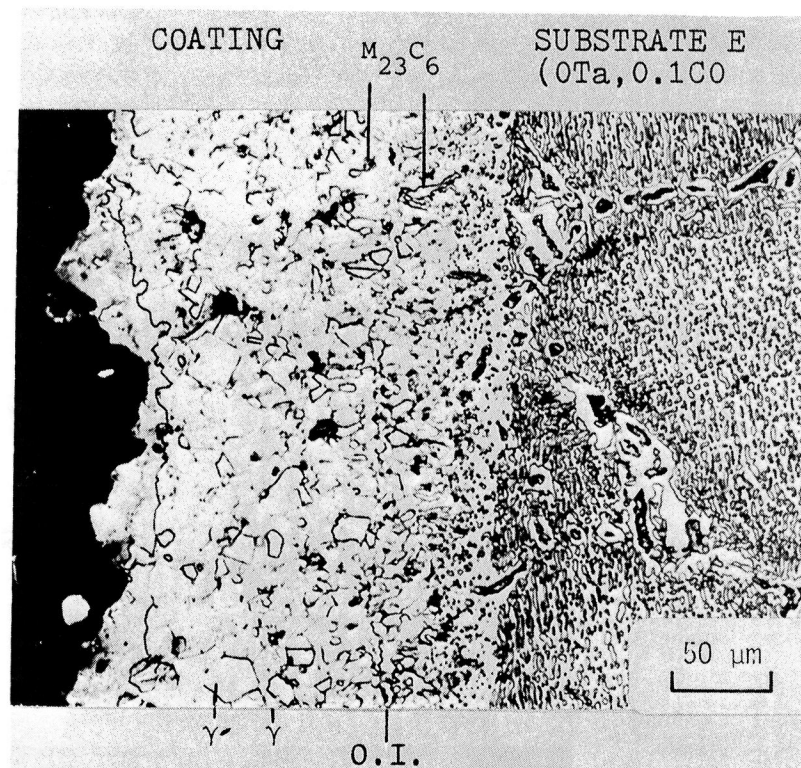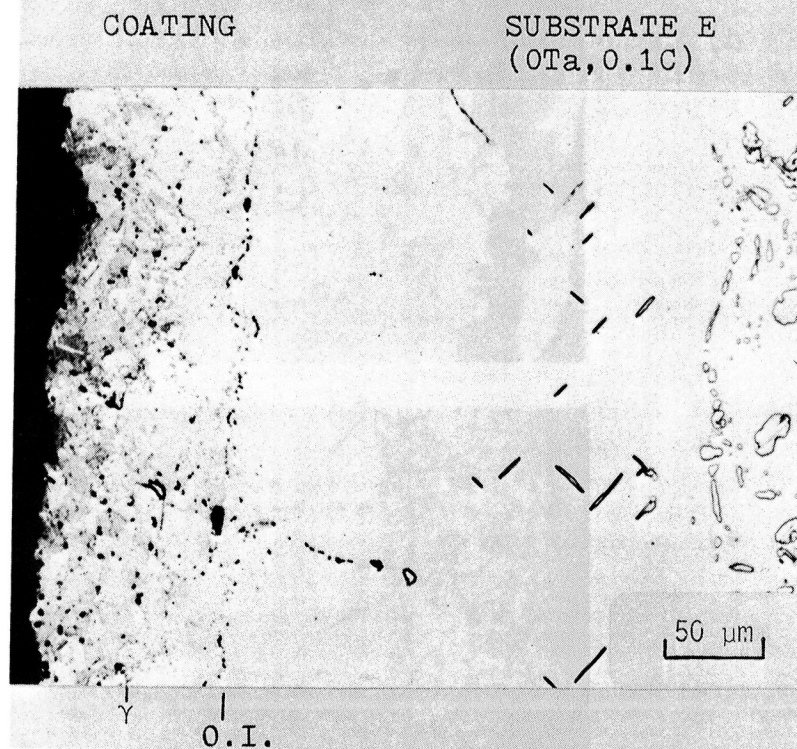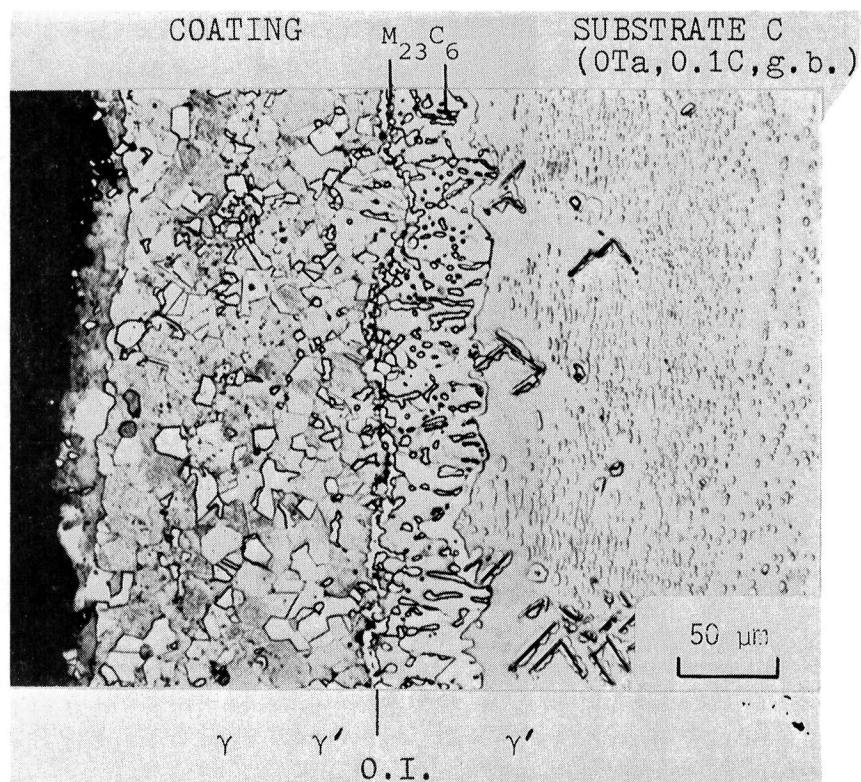   k) LPPC substrate H at 350 cycles (thick coat)
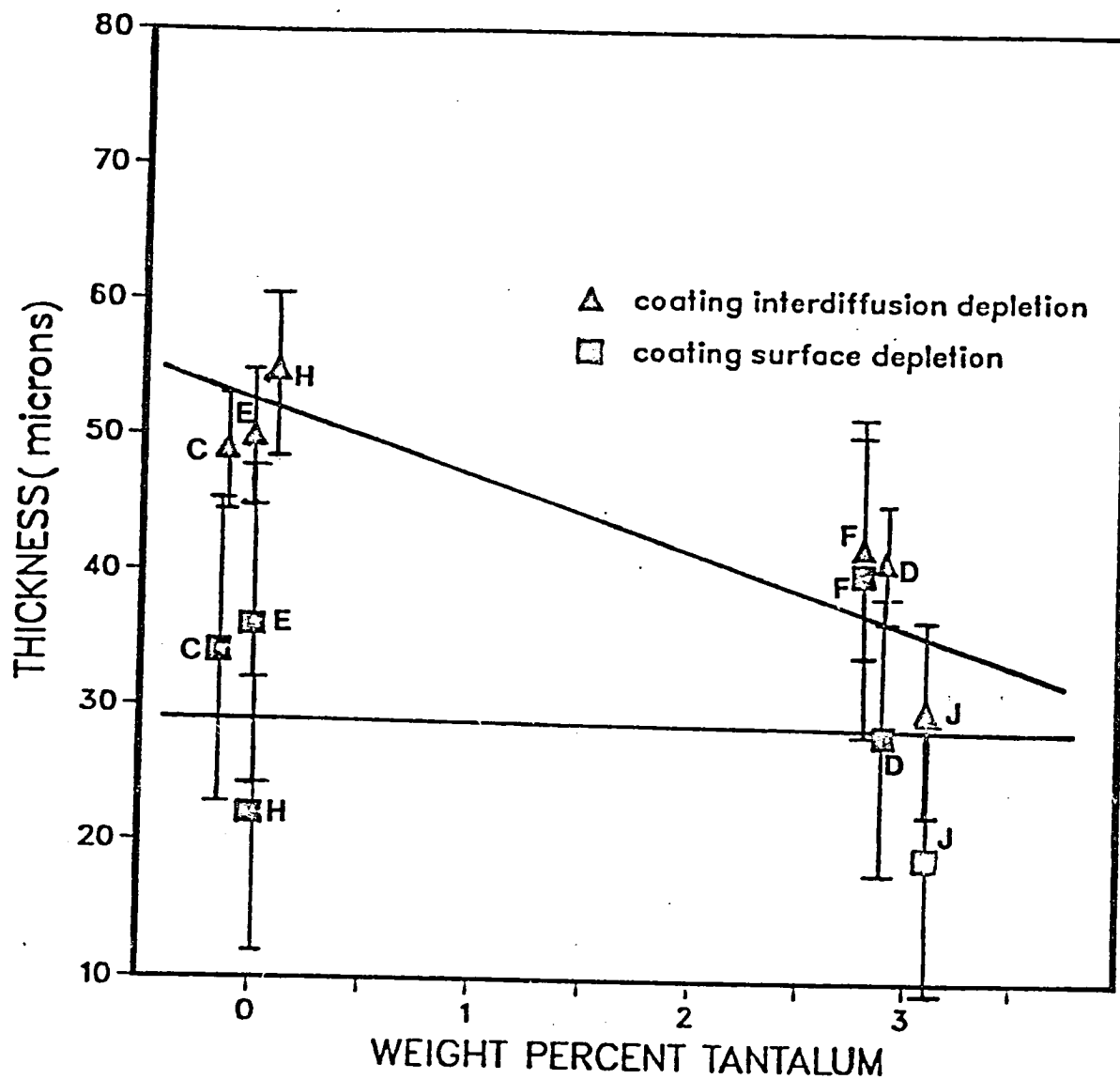
Figure 13   Coating interdiffusion and surface depletion
zone thicknesses for LPPC substrates at 50
cycles (β depletion)

in limited coating life. At low levels of Al, the other elements such as Cr moved to the surface to supply the growth of the less protective oxides. The development of the less protective oxides lead to increased spalling, which lead to higher rates of coating recession. These higher rates resulted in significant deterioration of the protective coating (Figure 14).

The high-carbon LPPC substrates developed $M_{23}C_6$ carbides during the degradation process. Generally, the $M_{23}C_6$ carbides nucleated at the coating/substrate and coating/coating interfaces (Figures 12b, c, d, f, and h). However, scattered $M_{23}C_6$ particles were found in both the coating and the substrate. The LPPC high-carbon, tantalum-free substrates formed a continuous $M_{23}C_6$ carbide at the coating/substrate interface (Figures 12b and e). In all high-carbon LPPC substrates tested, the quantity of $M_{23}C_6$ carbides decreased with increasing Ta concentration. The $M_{23}C_6$ carbide were mainly Cr with varying concentrations of W (up to 15 wt.%).

The $M_{23}C_6$ carbides, that formed early in the degradation process, dissolved at later times (Figures 12f and g). This dissolution occurred in all LPPC substrates that formed the less protective oxide scales and the LPPC substrates that were cycled 550 times (C and D). Their dissolution was due to the changing composition in the coating/substrate interdiffusion zone due to both degradation processes.

COATING   SUBSTRATE E
                  (0Ta,0.1C)

50 μm

O.I.
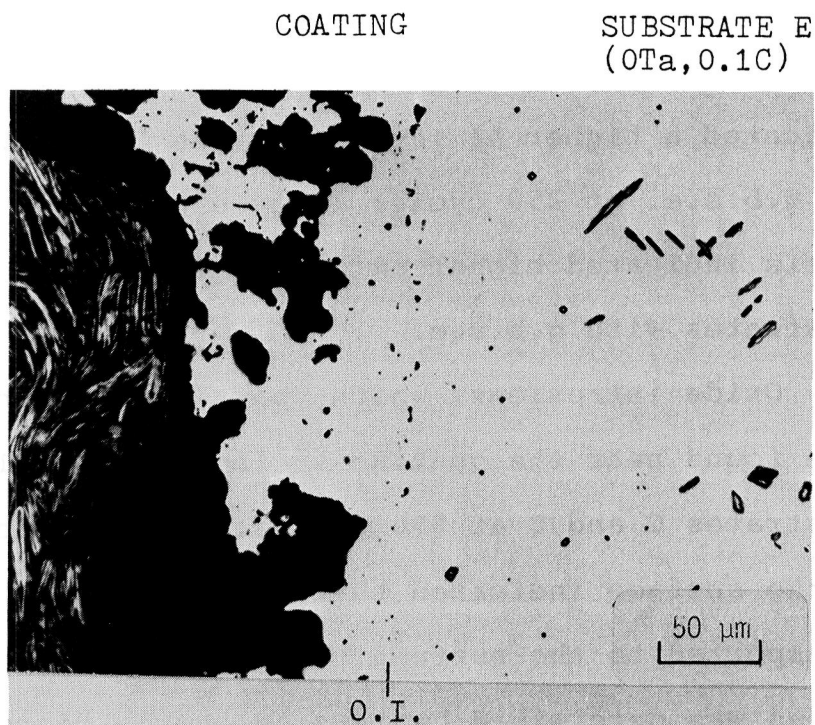
Figure 14. Cross section of LPPC substrate E at 250
             cycles shows a region where significant
             deterioration of the protective coating
             has occurred.

The coarse $\gamma+\gamma'$ structure was present at all cycle times for the LPPC substrates with g.b.s.e. for all coating thicknesses. The presence of the coarse $\gamma+\gamma'$ structure (Figure 12i) in the LPPC substrate C at 550 cycles indicated a higher Al level than the LPPC substrates without g.b.s.e. at 250 cycles (single phase γ). The higher levels indicated higher oxidation resistance for the LPPC substrates with g.b.s.e.

Oxide intrusions, which contained Hf-rich particles, were found near the coating surface (Figure 15) for LPPC substrates C and D at 550 cycles. The Hf-rich particles at the surface indicated that Hf from the substrate has been transported to the surface. The composition of the particles was determined by in-situ energy dispersive analysis. The particles were predominantely Hf with small concentrations of Al. These particles are normally associated with Hf-rich oxides. Improved oxidation resistance has been observed when Hf-rich oxides were present at the oxide/metal interface (32).

The degradation process was strongly affected by coating thickness. The coarse $\gamma+\gamma'$ structure was present in the thicker coatings for low-carbon substrates H and J at 350 cycles (Figures 12j and k). This $\gamma+\gamma'$ structure is contrasted with single-phase γ which was present in the thinner coatings for LPPC substrate H and J at 250 cycles.

61

COATING SURFACE

O.I.

50 μm

SUBSTRATE

COATING SURFACE

5 μm
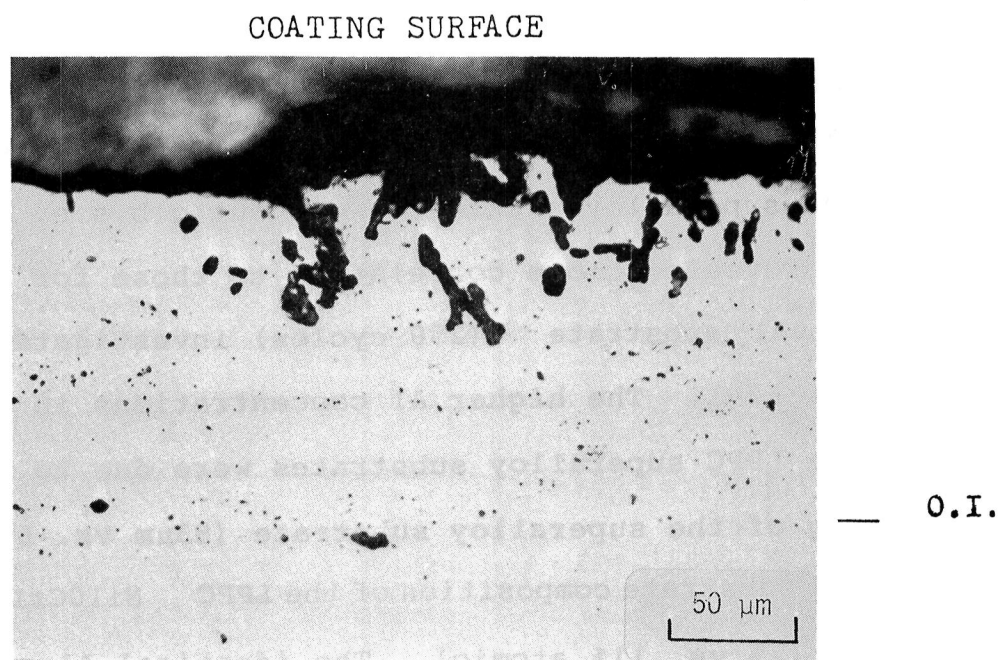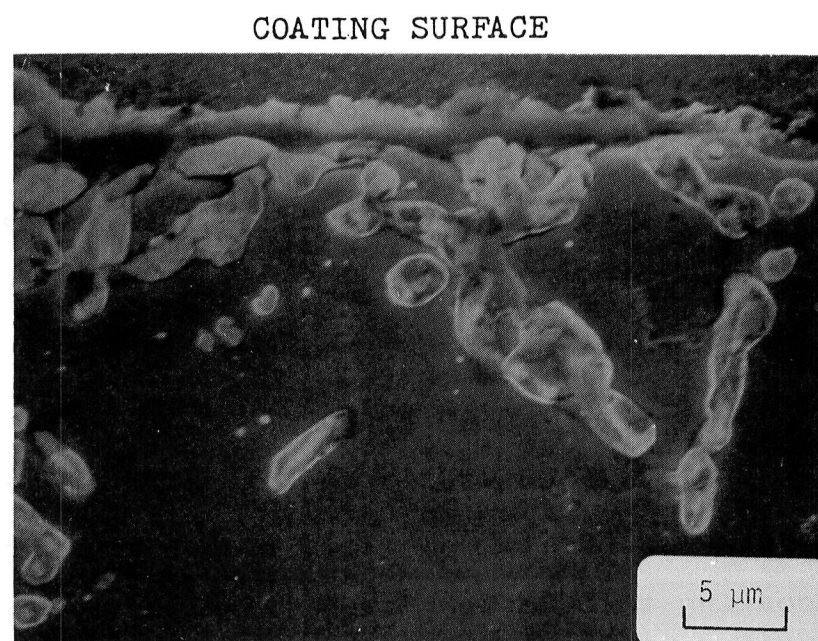
COATING

Figure 15   Oxide intrusions present in LPPC substrates with
             g.b. elements at 550 cycles(LPPC substrate C-OTa,
             0.1C,g.b.) a) optical photomicrograph b) SEM photo-
             micrograph

62

Concentration/Distance Profiles

The Al concentration/distance profiles (Figure 16a-f) for the superalloy substrates without g.b.s.e. (E, F, H, and J) revealed close correlation to those for the LPPC Ni10Cr10Al substrate (250 cycles) investigated by Nesbitt (24). The higher Al concentrations in the coating for the LPPC superalloy substrates were due to the thicker coating of the superalloy substrate (83μm vs. 67μm) and the lower Al substrate composition of the LPPC Ni10Cr10Al substrate (7% vs. 11% atomic). The identical Al profiles (similar shapes and concentrations) for the LPPC superalloy substrates at 350 cycles and the LPPC Ni10Cr10Al substrate at 250 cycles indicate that the simultaneous oxidation and coating/substrate interdiffusion processes were similar for both LPPC substrate systems. These profiles indicate similar oxidation resistance for the LPPC superalloy and the LPPC Ni10Cr10Al substrate.

The Al concentration/distance profiles for LPPC substrates with g.b.s.e. were higher than the LPPC substrates without g.b.s.e. (Figures 16e and f). The higher Al concentrations were due to the g.b.s.e. and in most cases, larger coating thicknesses. The effect of g.b.s.e. was noted for LPPC substrate C at 550 cycles whose thickness was of the same magnitude as the LPPC substrates without g.b.s.e. A direct comparison of the Al profile is illustrated in Figure 17. In this case, the concentration/
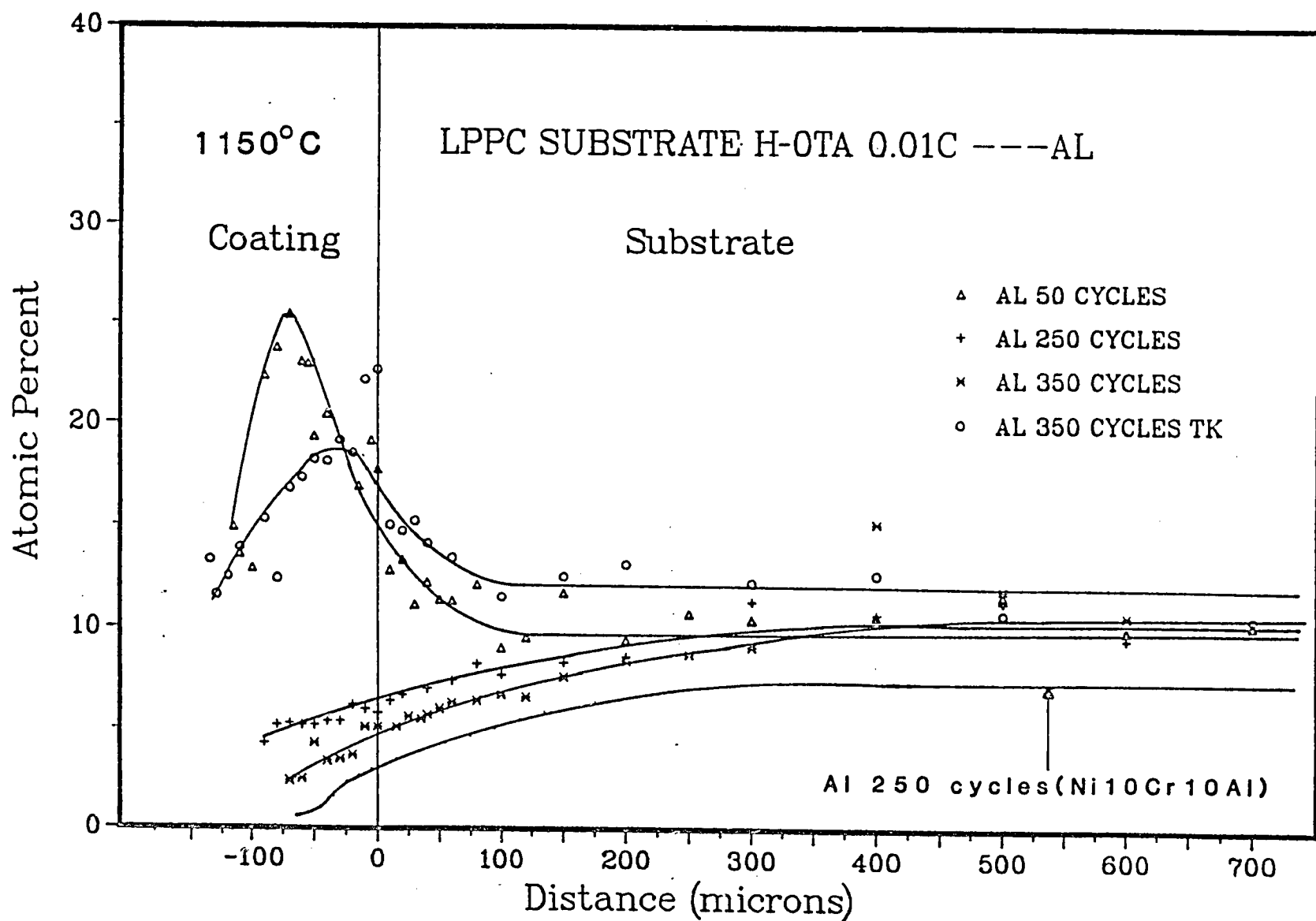
Figure 16   LPPC substrate concentration/distance profiles for Al
             a) LPPC substrate H -- 0 Ta, 0.01C

1150°C   LPPC SUBSTRATE J-3TA-0.01C ———AL

Coating   Substrate

Legend:
- △ AL 50 CYCLES
- + AL 250 CYCLES
- × AL 350 CYCLES
- ○ AL 350 CYCLES TK

Al 250 cycles (Ni 10 Cr 10 Al)

Y-axis: Atomic Percent (0 to 40)
X-axis: Distance (microns) (-100 to 700)

Figure 16   LPPC substrate concentration/distance profiles for Al (con't)
b) LPPC substrate J -- 3 Ta, 0.01C

Figure 16   LPPC substrate concentration/distance profiles for Al (con't)
c) LPPC substrate E -- 0 Ta, 0.1C

Figure 16   LPPC substrate concentration/distance profiles for Al (con't)
d) LPPC substrate F -- 3 Ta, 0.1C

Figure 16   LPPC substrate concentration/distance profiles for Al (con't)
             e) LPPC substrate C -- 0 Ta, 0.1C, g.b.

Figure 16 LPPC substrate concentration/distance profiles for Al (con't)
f) LPPC substrate D -- 3 Ta, 0.01C, g.b.

distance profiles for low-carbon, tantalum-free, LPPC substrate (without g.b.s.e.) were measured on a thicker side. The extra measurement allowed comparison of equivalent coating thicknesses. As shown, the Al level for high-carbon, tantalum-free, LPPC substrate C at 550 cycles was substantially higher than the Al level for LPPC substrate H at 250 cycles (Figure 17). The higher Al levels demonstrate the improved oxidation resistance associated with the g.b.s.e. additions. The importance of coating thickness was observed for LPPC substrates H and J (without g.b.s.e.) at the 350 cycle point. In both cases, the thicker coatings had substantially higher Al levels than the thinner coatings (Figure 16a, b). The higher Al levels were a result of the higher Al supply in the thicker coating.

The Al profiles indicate that some of the Al that has diffused into the substrate returned to the coating at later times. In all cases, the Al maximum was moving toward the substrate with increasing time (Figures 16a-f). The Al maximum for LPPC substrates F at 130 cycles, and LPPC substrates C and D at 550 cycles were present in the substrates. The Al maximum in the substrate indicates that some of the Al that moved into the substrate will at later times move back into the coating. The return was necessary to continue the supply of Al to the protective Al_2O_3 scale. The Al maximums in the substrate were also observed for the LPPC Ni-Cr-Al substrates in the prior study (24).
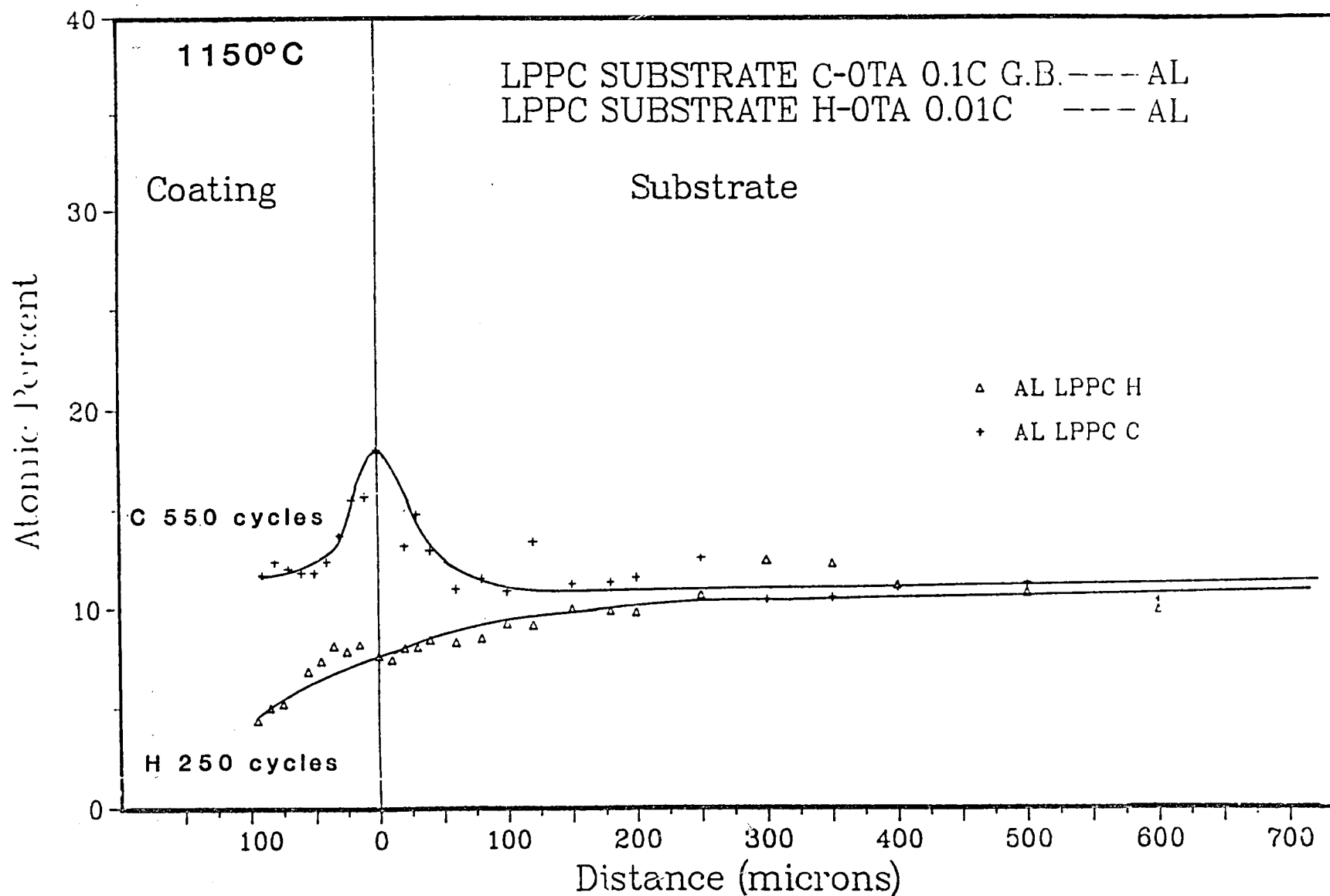
Figure 17   Comparison of Al concentration/distance profiles for LPPC substrates with (LPPC substrate C) and without g.b.s.e. (LPPC substrate H)

The Cr concentration/distance profiles (Figure 18) for the superalloy substrates without g.b.s.e. (E, F, H, and J) revealed close correlation to those for the LPPC Ni10Cr10Al substrate (250 cycles) investigated by Nesbitt (24). Both the superalloy and Ni10Cr10Al Cr profiles were flat with small gradients at 250 cycles. The higher concentration of Cr for the LPPC Ni10Cr10Al substrate was due to the higher Cr level in this substrate (13% vs. 10% atomic). The similar shapes and concentrations demonstrate the similar simultaneous oxidation and interdiffusion processes for these two systems.

A Cr maximum was observed in all Cr profiles at the 50 cycle point (Figure 18). The Cr maximums were either caused by the diffusion cross terms (see diffusion couple studies) or by the changing phase volume fractions (Figures 12a-c). The Cr maximums were also observed for the LPPC Ni-Cr-Al substrates investigated in the prior study (24). In the prior study, the Cr maximum was attributed to the diffusion cross terms (single phase γ was present).

The similar Al and Cr profiles for both Ta and Ta-free LPPC substrates indicate that Ta was not affecting oxidation resistance. The similar profiles for Ta and Ta-free LPPC substrates was observed for Group 1 (high-carbon with g.b.s.e.), Group 2 (high carbon without g.b.s.e.), and Group 3 (low-carbon without g.b.s.e.) substrates.

The similar Al and Cr profiles for high- and low-carbon LPPC substrates at later times in the degradation process indicate that C did not affect oxidation resistance. The

Figure 18   LPPC substrate concentration/distance profiles for Cr
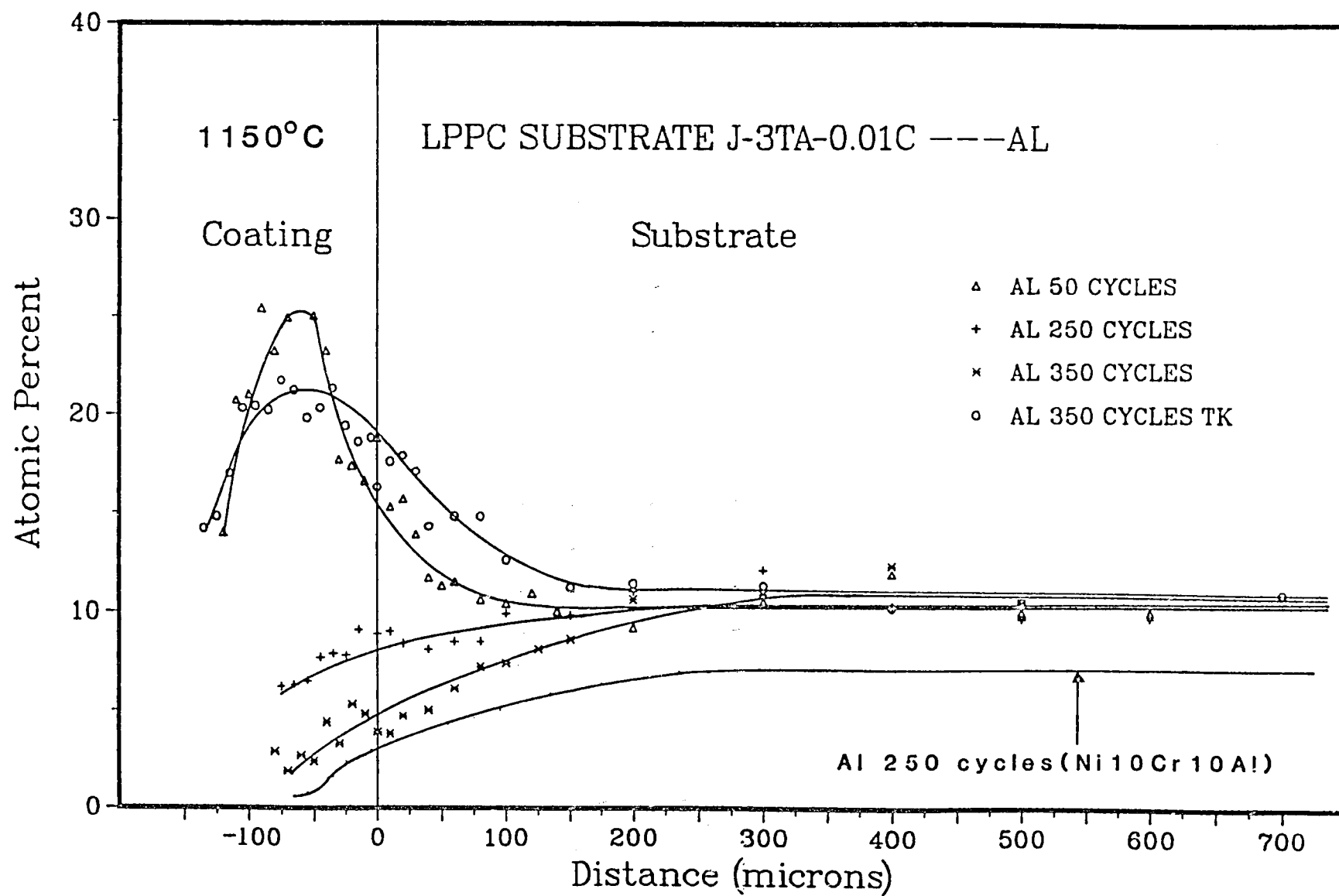   a) LPPC substrate H -- 0 Ta, 0.01C

Figure 18   LPPC substrate concentration/distance profiles for Cr (con't)
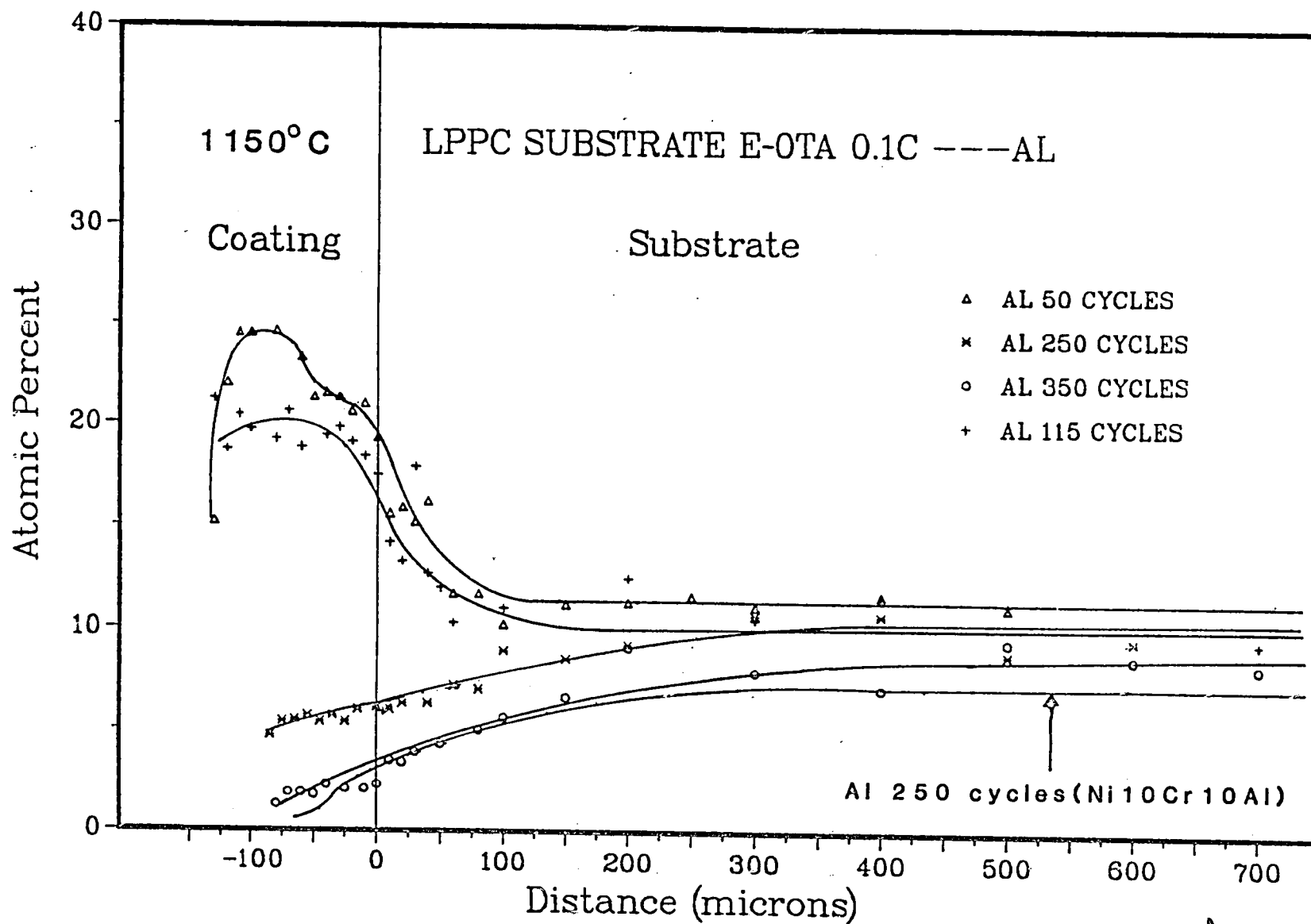   b) LPPC substrate J -- 3 Ta, 0.01C

Figure 18   LPPC substrate concentration/distance profiles for Cr (con't)
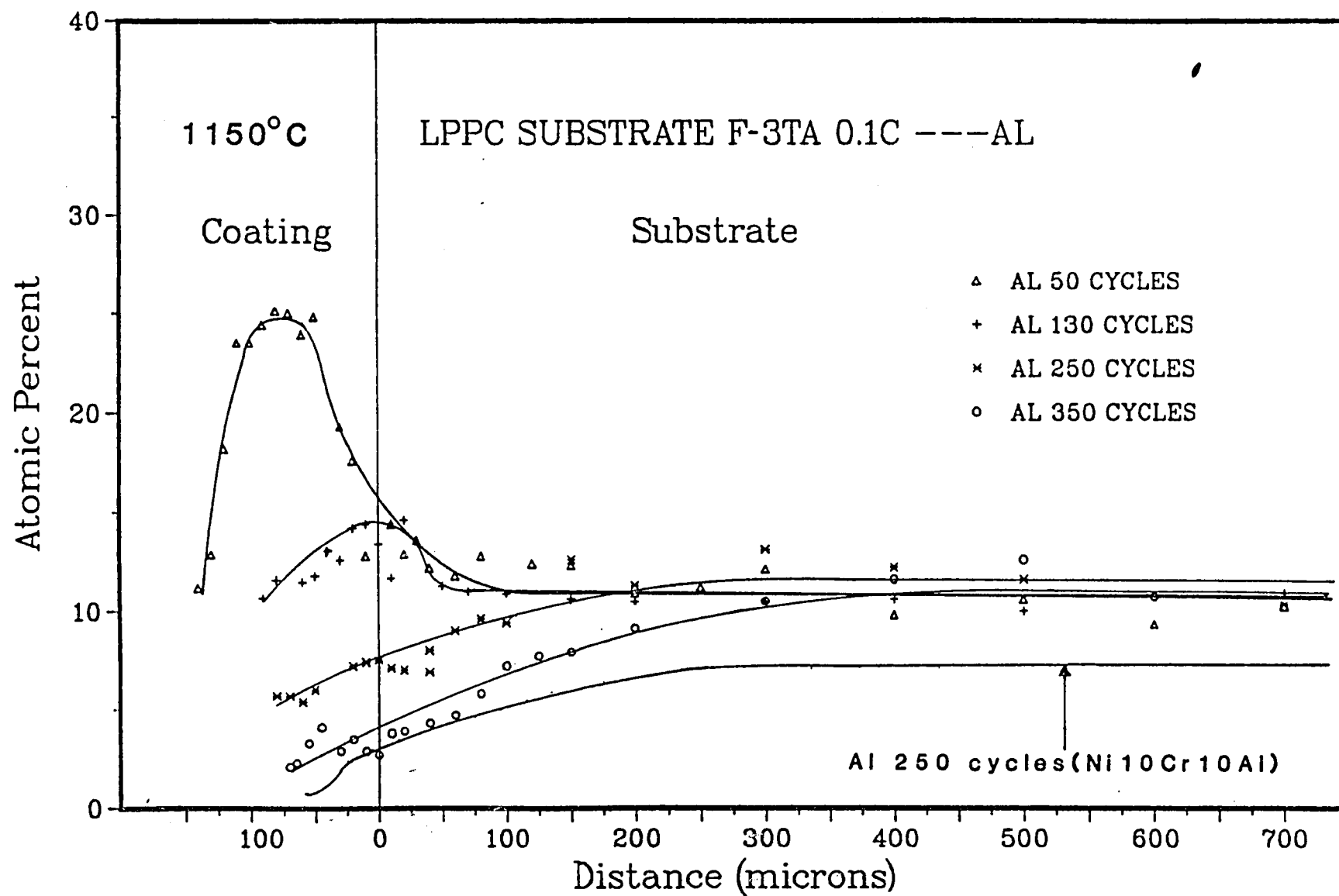c) LPPC substrate E -- 0 Ta, 0.1C

Figure 18   LPPC substrate concentration/distance profiles for Cr (con't)
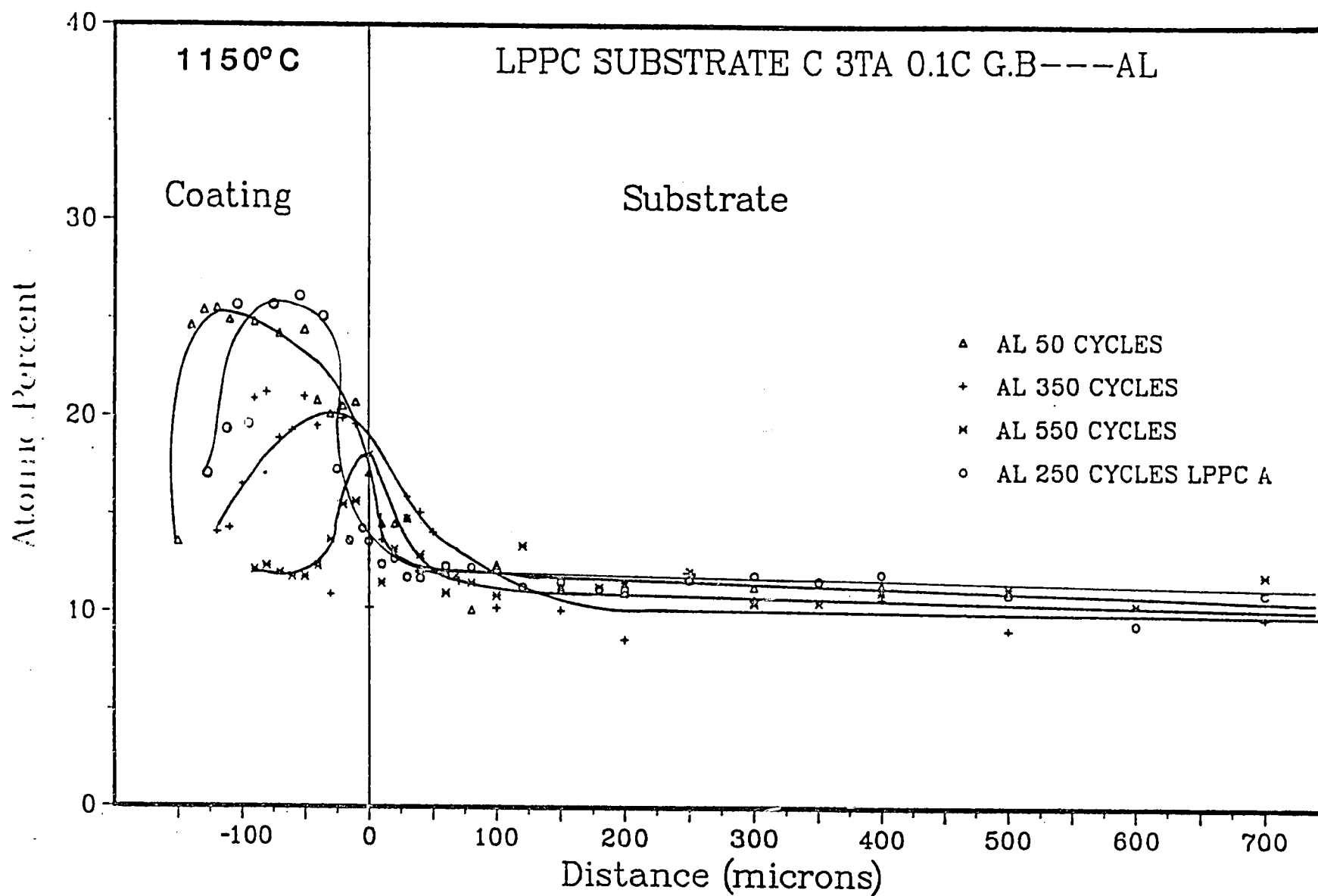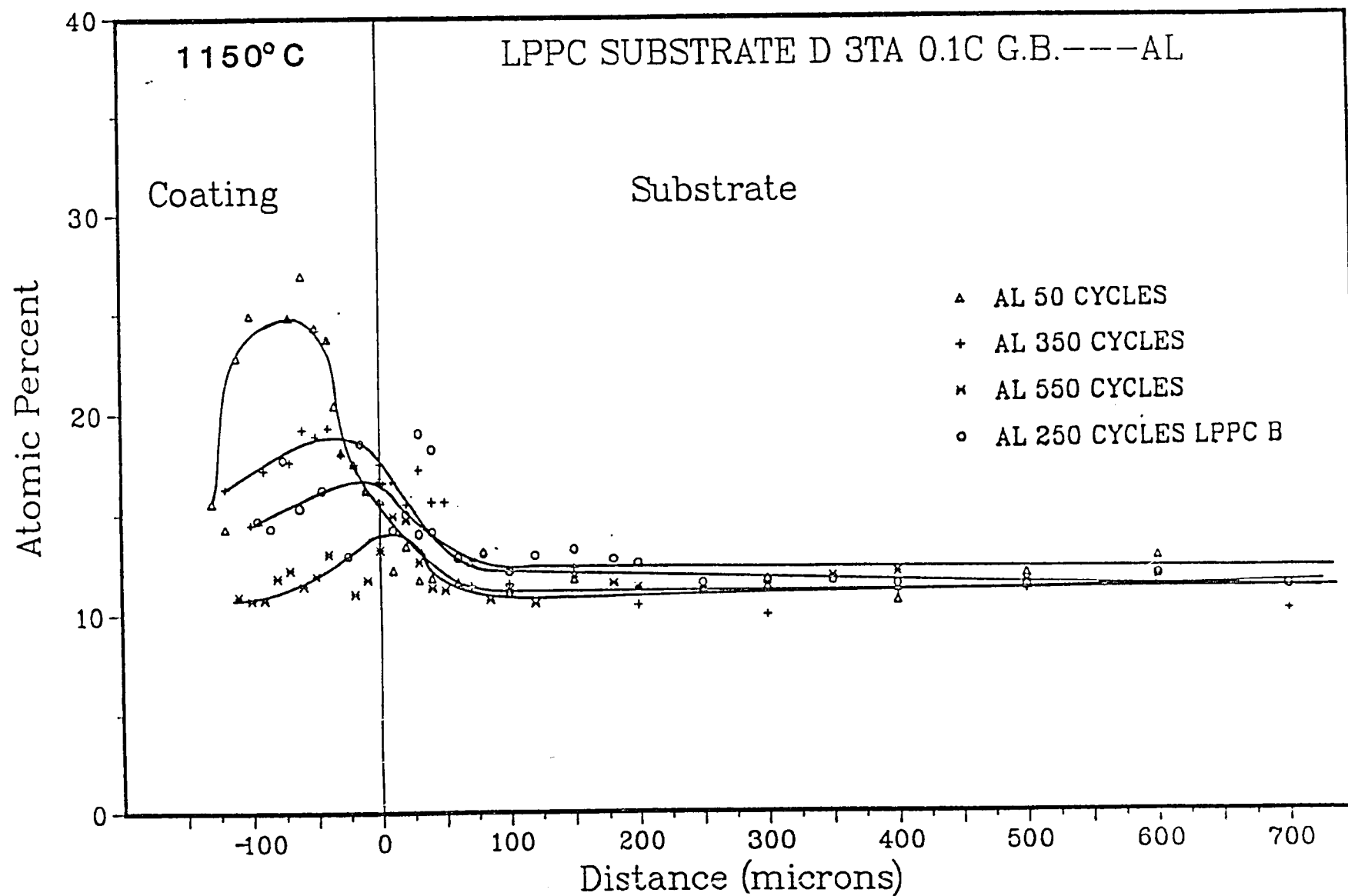d) LPPC substrate F -- 3 Ta, 0.1C

Figure 18 LPPC substrate concentration/distance profiles for Cr (con't)
e) LPPC substrate C -- 0 Ta, 0.1C, g.b.

Figure 18   LPPC substrate concentration/distance profiles for Cr (con't)
             f) LPPC substrate D -- 3 Ta, 0.1C, g.b.

similar profiles were the result of the dissolution of $M_{23}C_6$ carbides. The dissolution (flat Cr profiles) was observed for both LPPC substrates that developed the less protective oxides (thin-coated LPPC substrates without g.b.s.e. at 250 and 350 cycles) and the LPPC substrates cycled 550 times. The dissolution of $M_{23}C_6$ carbides at 550 cycles (protective oxides present) indicated that $M_{23}C_6$ carbides were dissolved before breakaway oxidation.

The similar Al and Cr profiles for the LPPC superalloy (without g.b.s.e.) and LPPC Ni10Cr10Al substrates indicate that the other substrate additions, such as W and Co were not affecting oxidation resistance. The concentration/distance profile for Co, W, and Ta indicate that these elements were reaching the coating surface at later cycle times (Figures 19 and 20). These results indicate that these elements were not affecting oxidation resistance or that the elements were synergistically not affecting oxidation resistance. Further investigation is necessary to determine which conclusion is applicable.

The diffusion of substrate elements (Co, Ta, and W) into the coating was significantly affected by coating thickness. The effect of coating thickness was clearly illustrated for LPPC substrates H and J (Figures 19a,b and 20a,b). Here, the thicker coatings (H-tk and J-tk) had significantly lower concentrations of Ta, Co, and W at the surfaces than the thinner coating at equivalent cycle times.
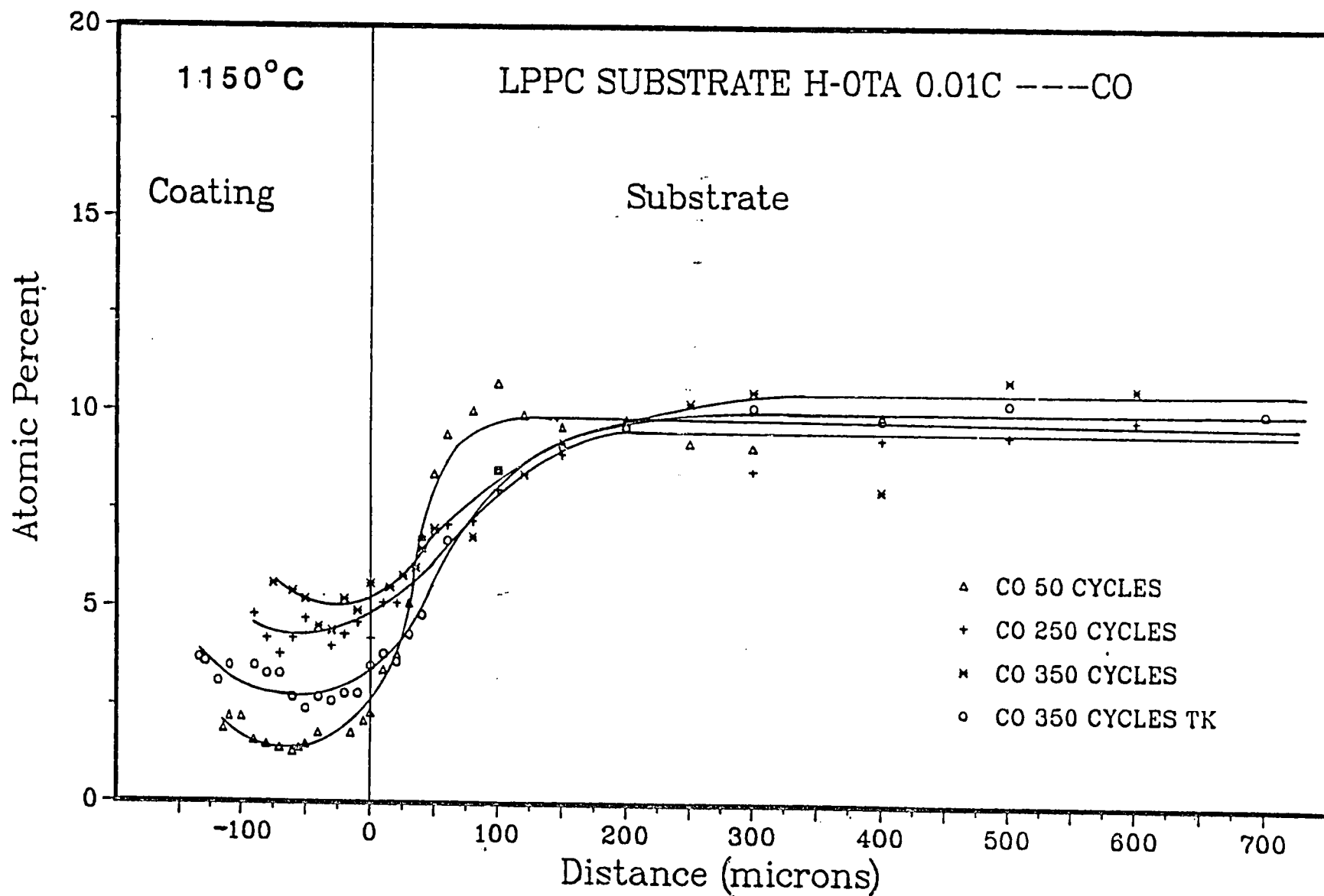
Figure 19   LPPC substrate concentration/distance profiles for Co
             a) LPPC substrate H -- OTa, 0.01C
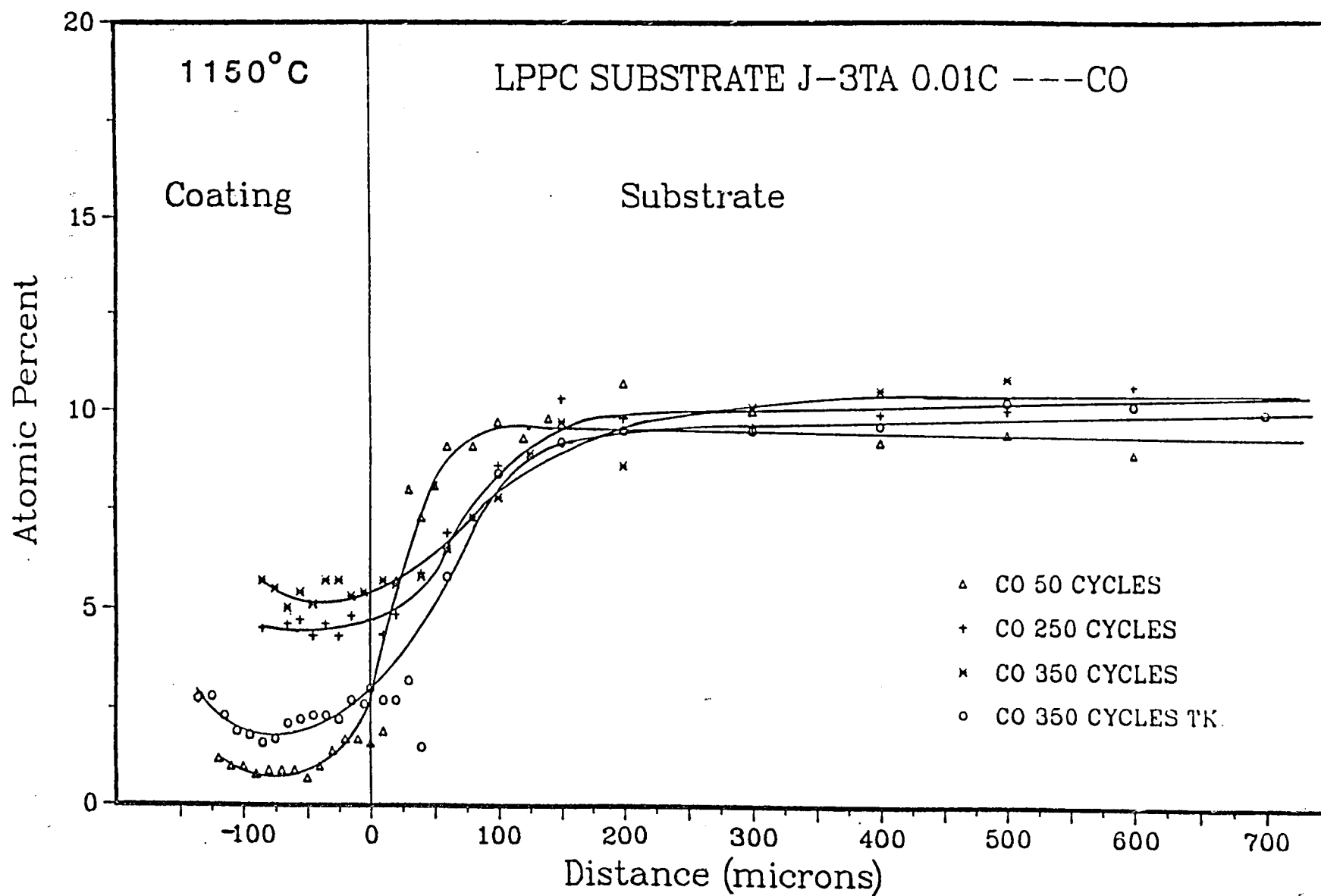
Figure 19   LPPC substrate concentration/distance profiles for Co (con't)
             b) LPPC substrate J -- 3 Ta, 0.01C
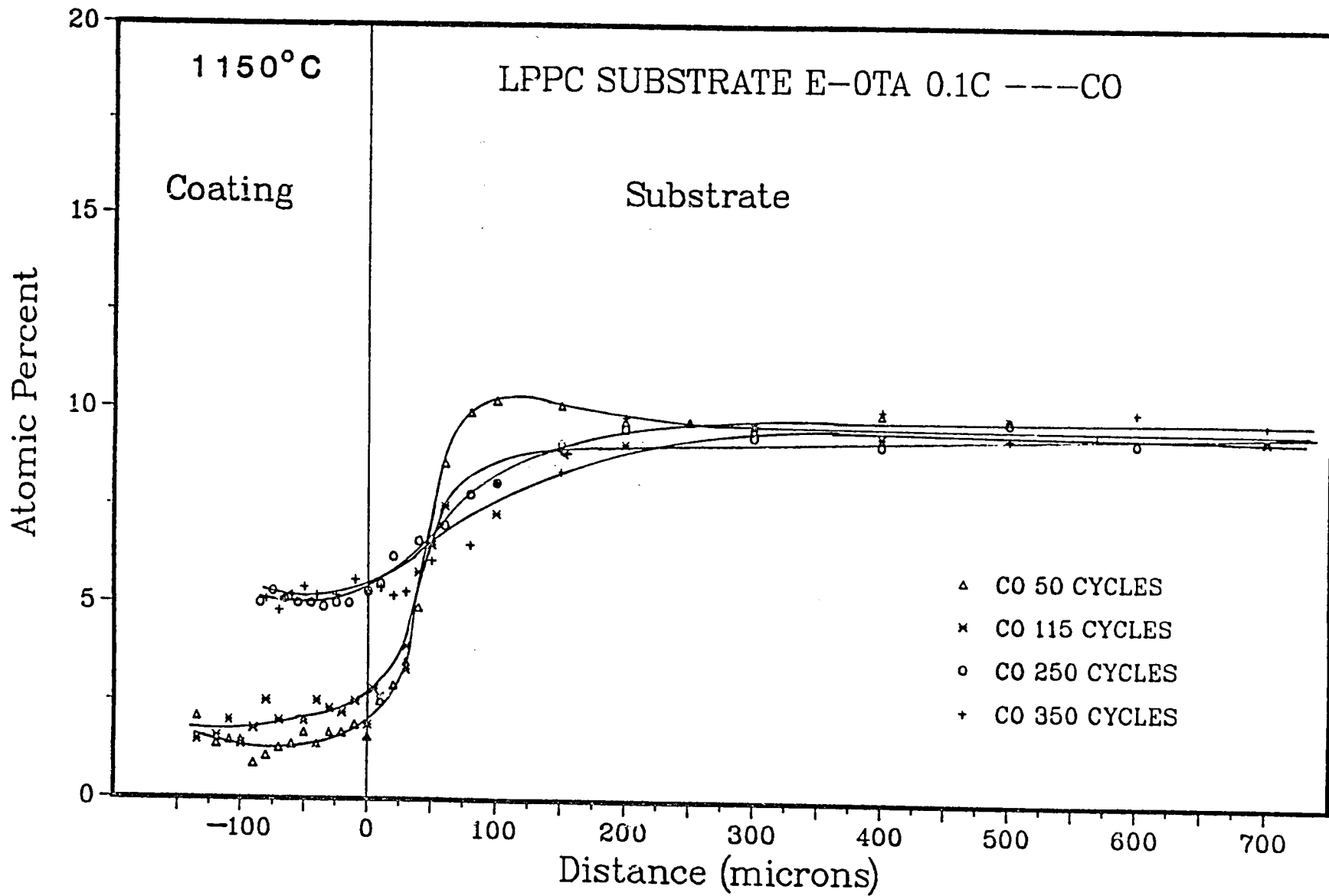
Figure 19   LPPC substrate concentration/distance profiles for Co (con't)
             c) LPPC substrate E -- 0 Ta, 0.1C
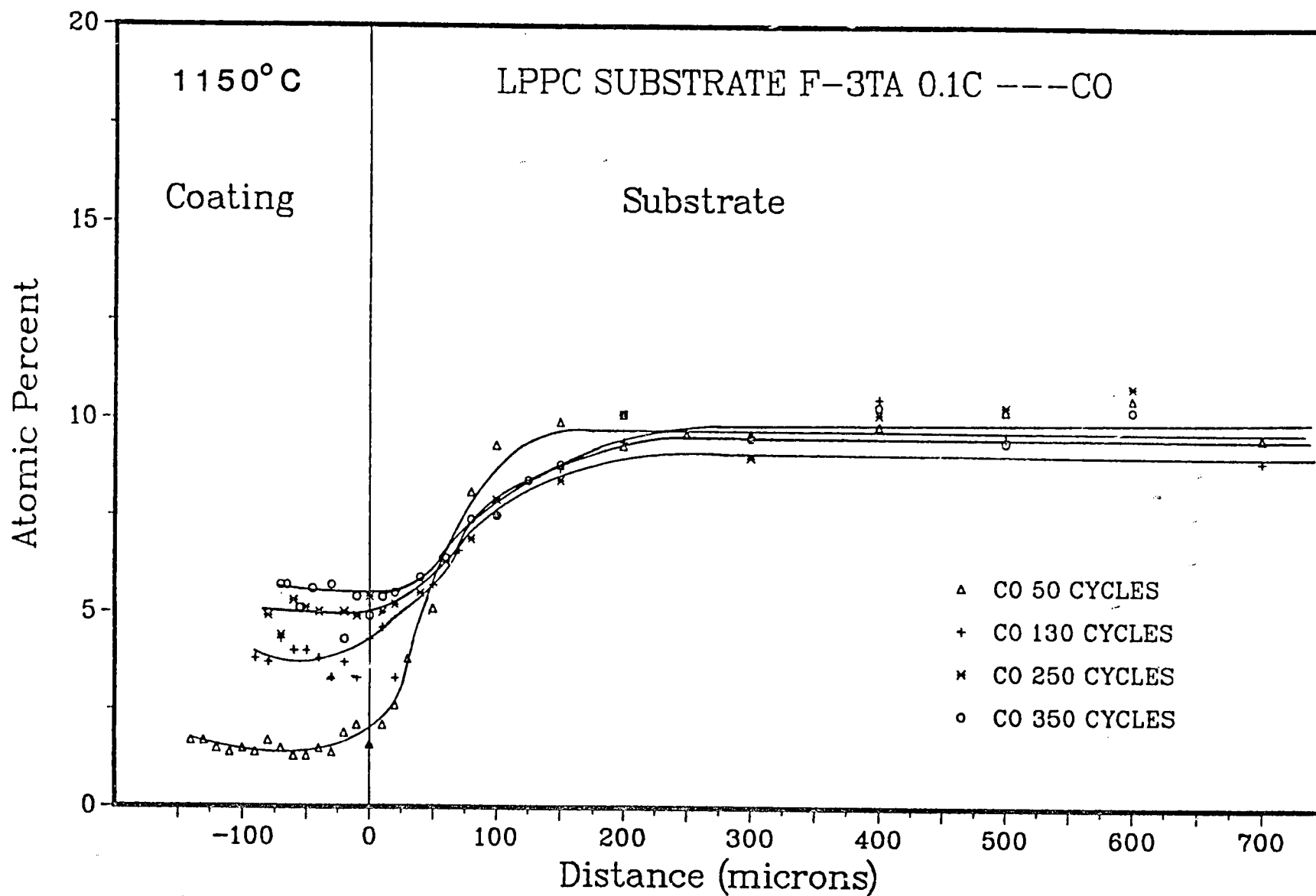
Figure 19   LPPC substrate concentration/distance profiles for Co (con't)
             d) LPPC substrate F -- 3 Ta, 0.1C
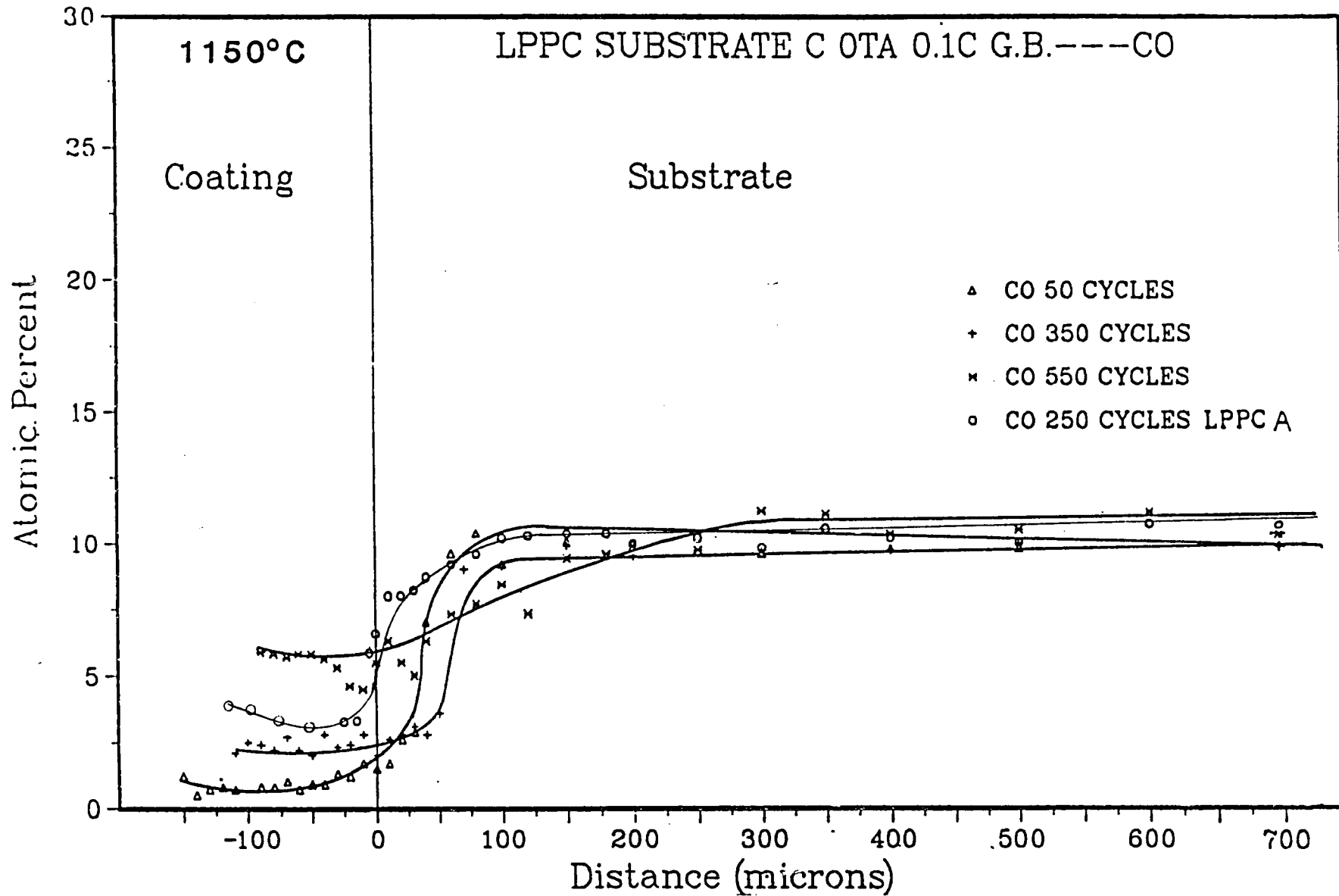
Figure 19   LPPC substrate concentration/distance profiles for Co (con't)
             e) LPPC substrate C -- 0 Ta, 0.1C, g.b.
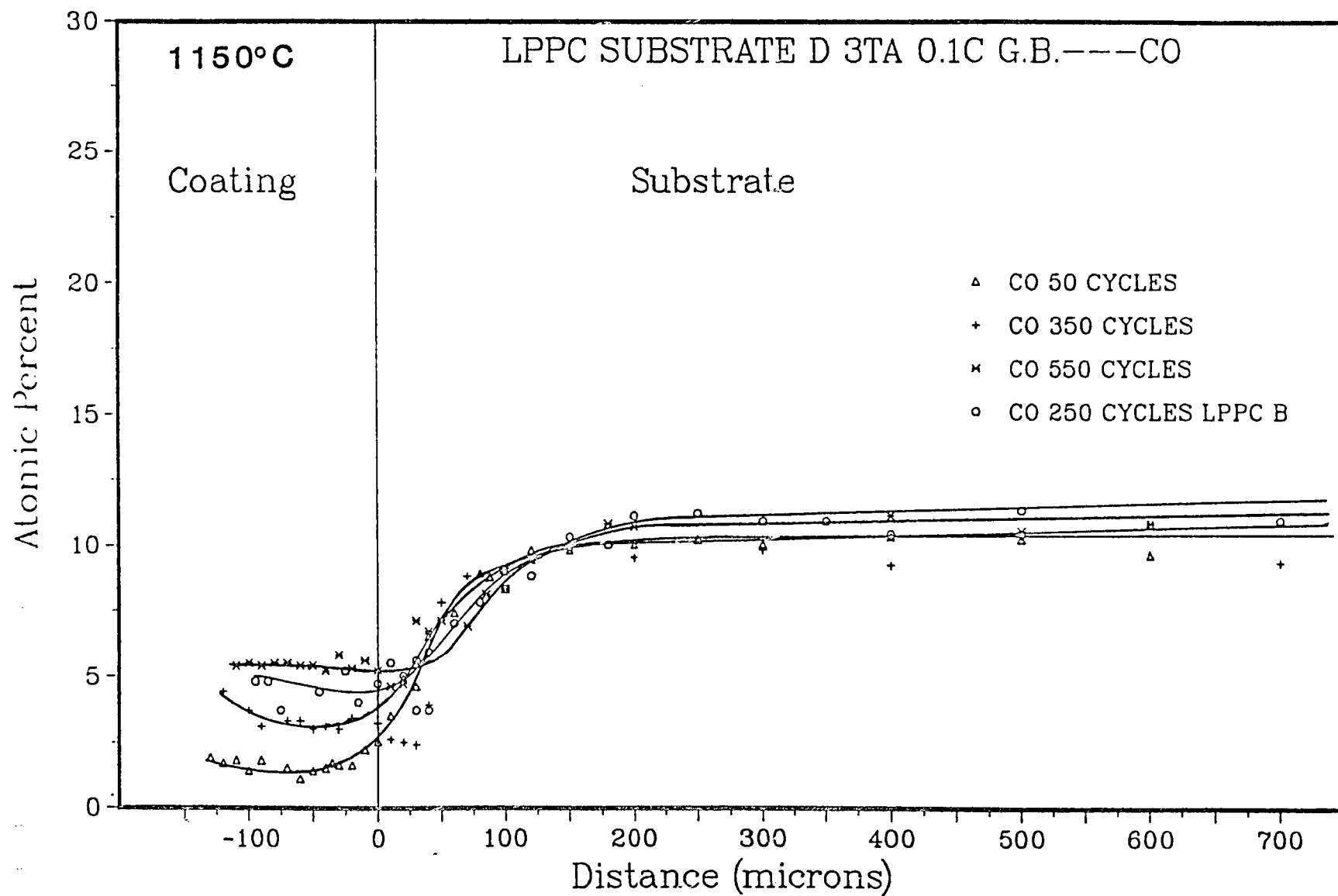
Figure 19   LPPC substrate concentration/distance profiles for Co (con't)
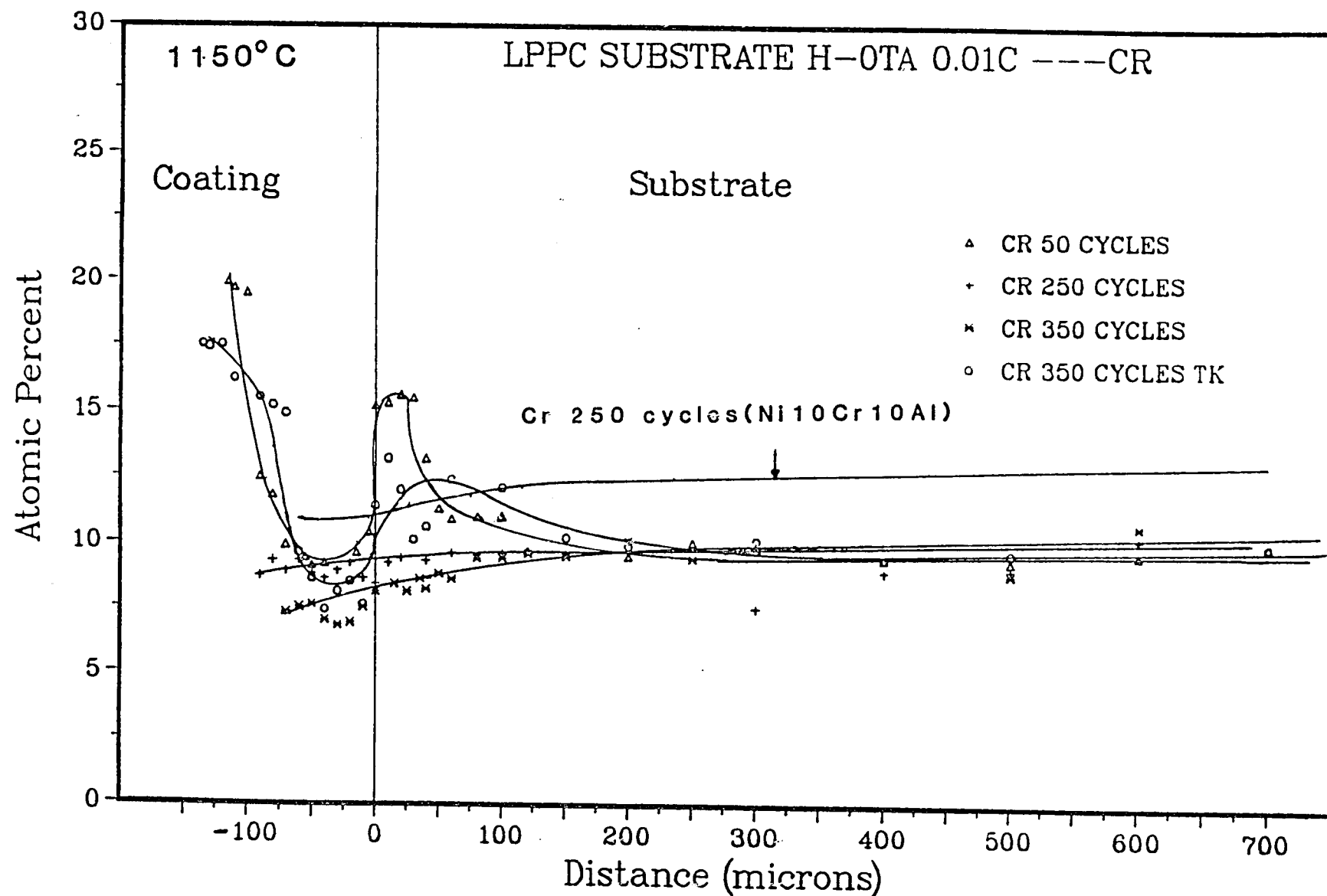   f) LPPC substrate D -- 3 Ta, 0.1C, g.b.
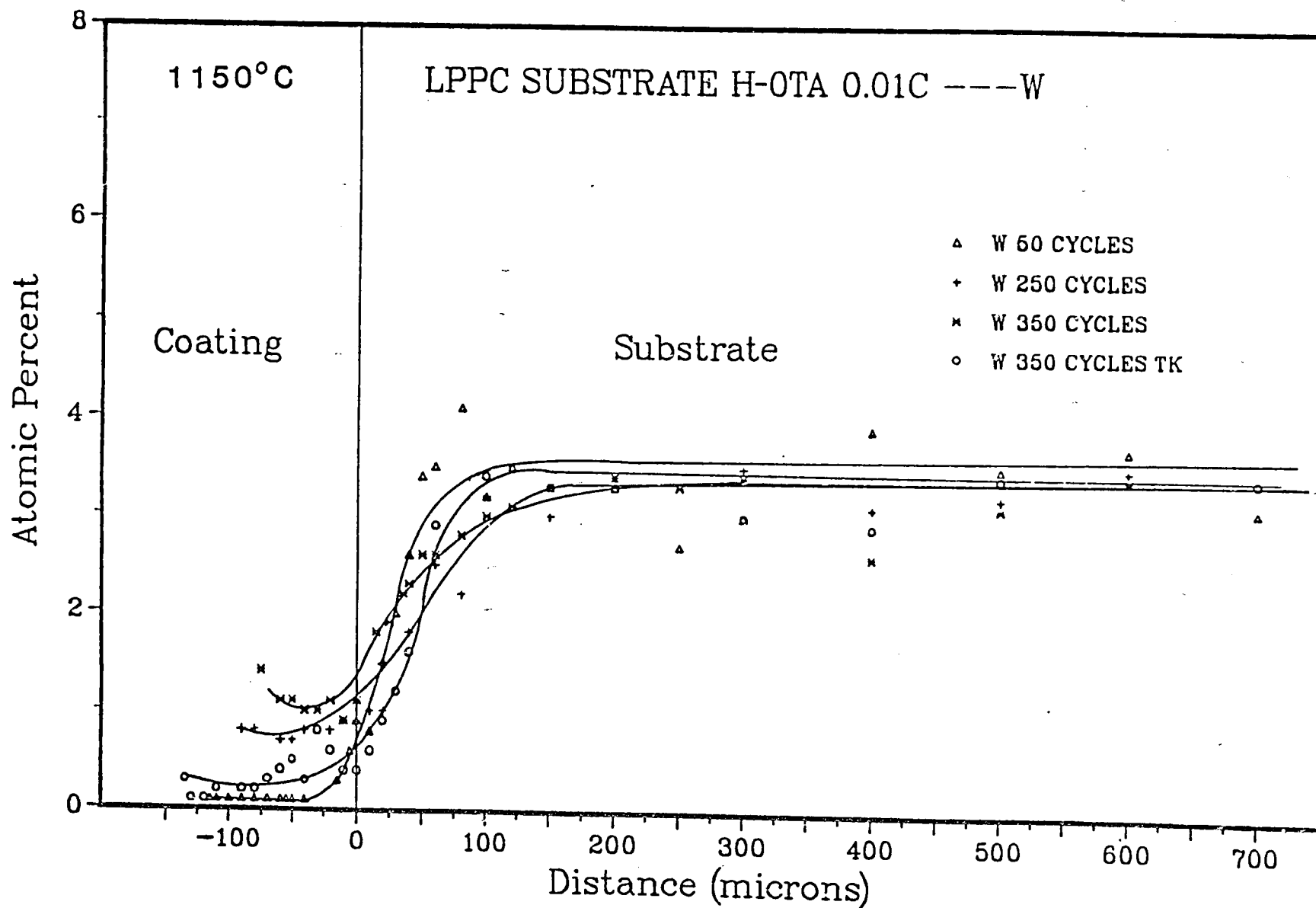
Figure 20   LPPC substrate concentration/distance profiles for W and Ta
a) LPPC substrate H -- 0 Ta, 0.01C
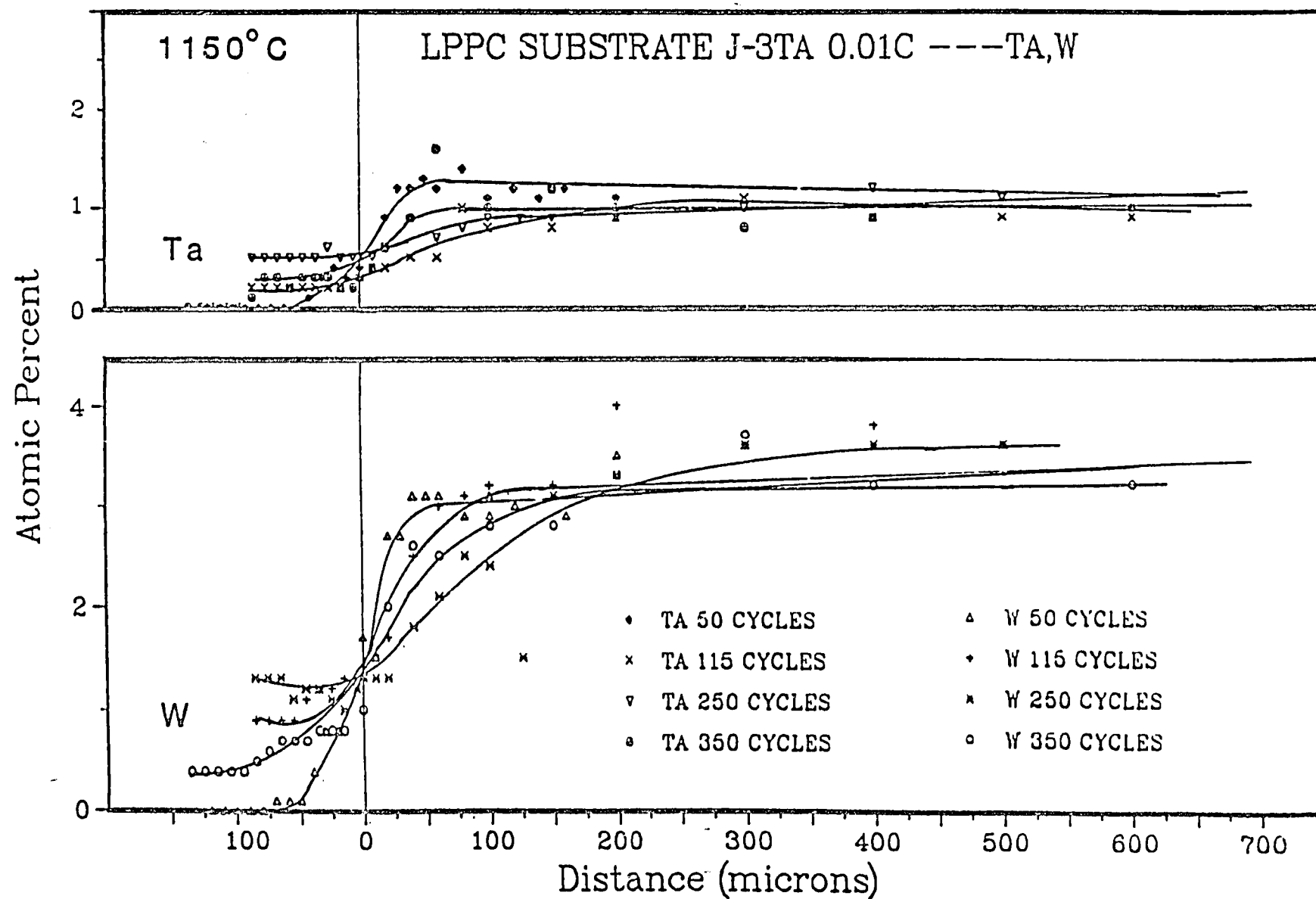
Figure 20   LPPC substrate concentration/distance profiles for W and Ta (con't)
             b) LPPC substrate J -- 3 Ta, 0.01C
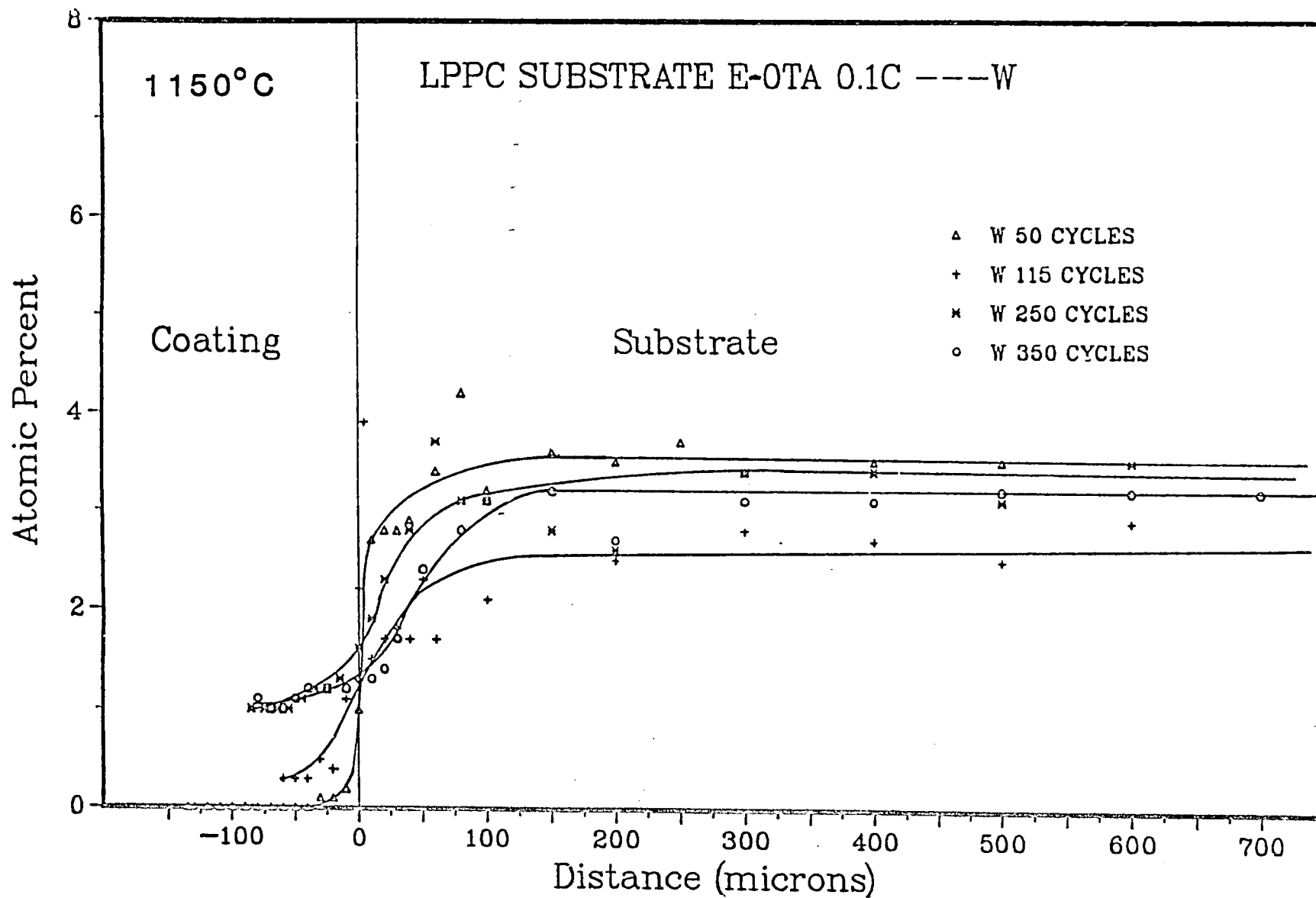
Figure 20 LPLPPC substrate concentration/distance profiles for W and Ta (con't)
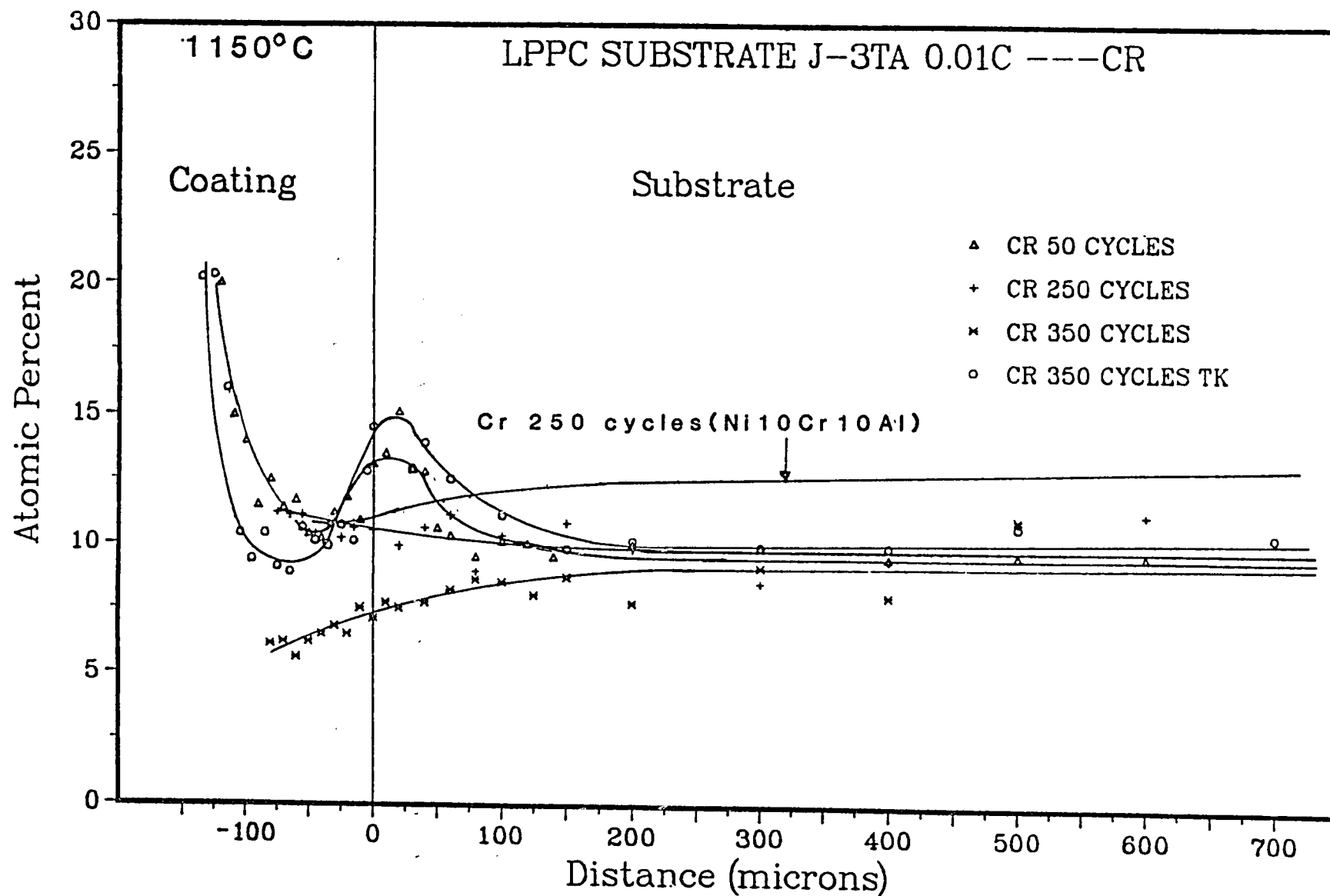c) LPPC substrate E -- 0 Ta, 0.1C
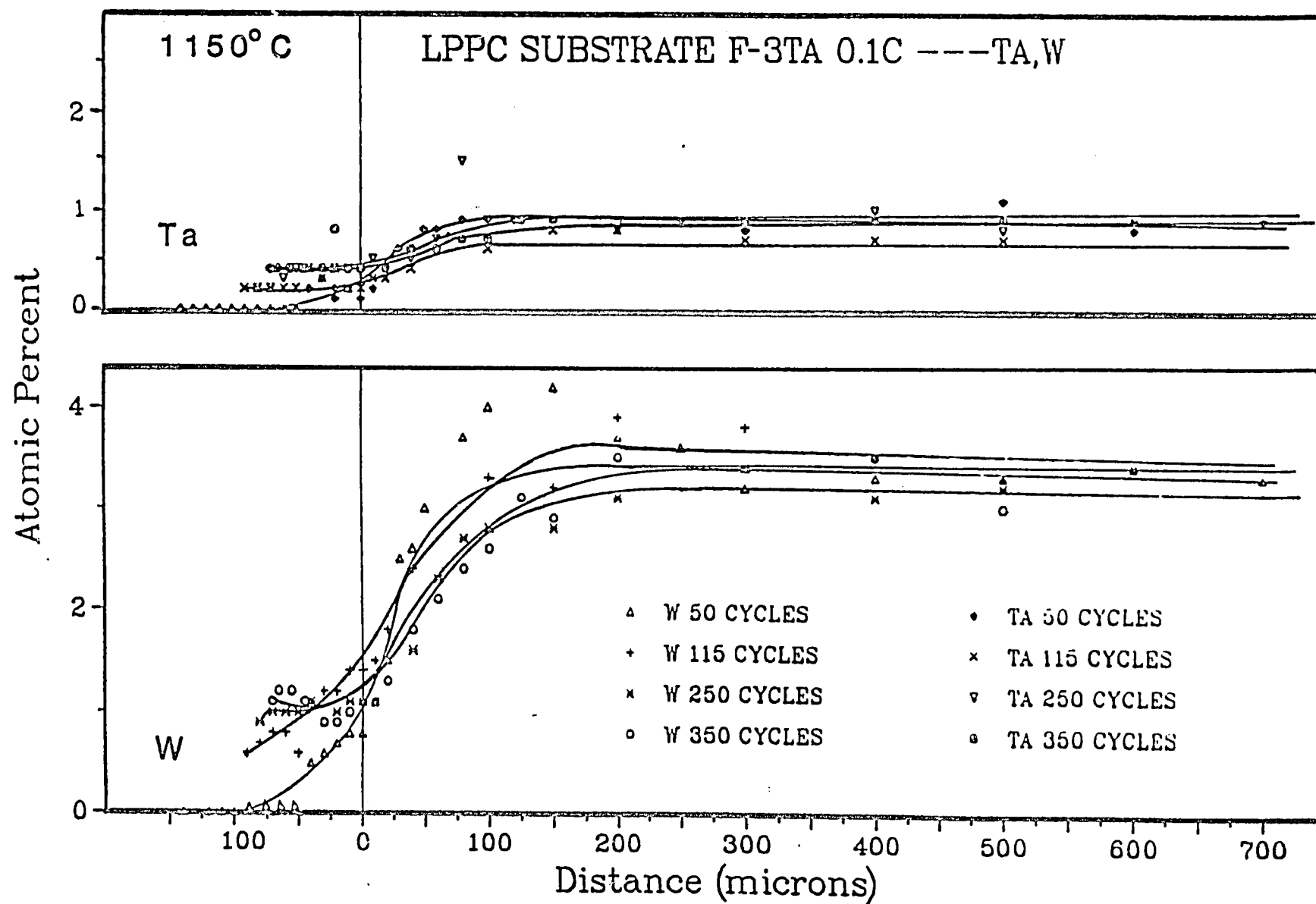
Figure 20   LPPC substrate concentration/distance profiles for W and Ta (con't)
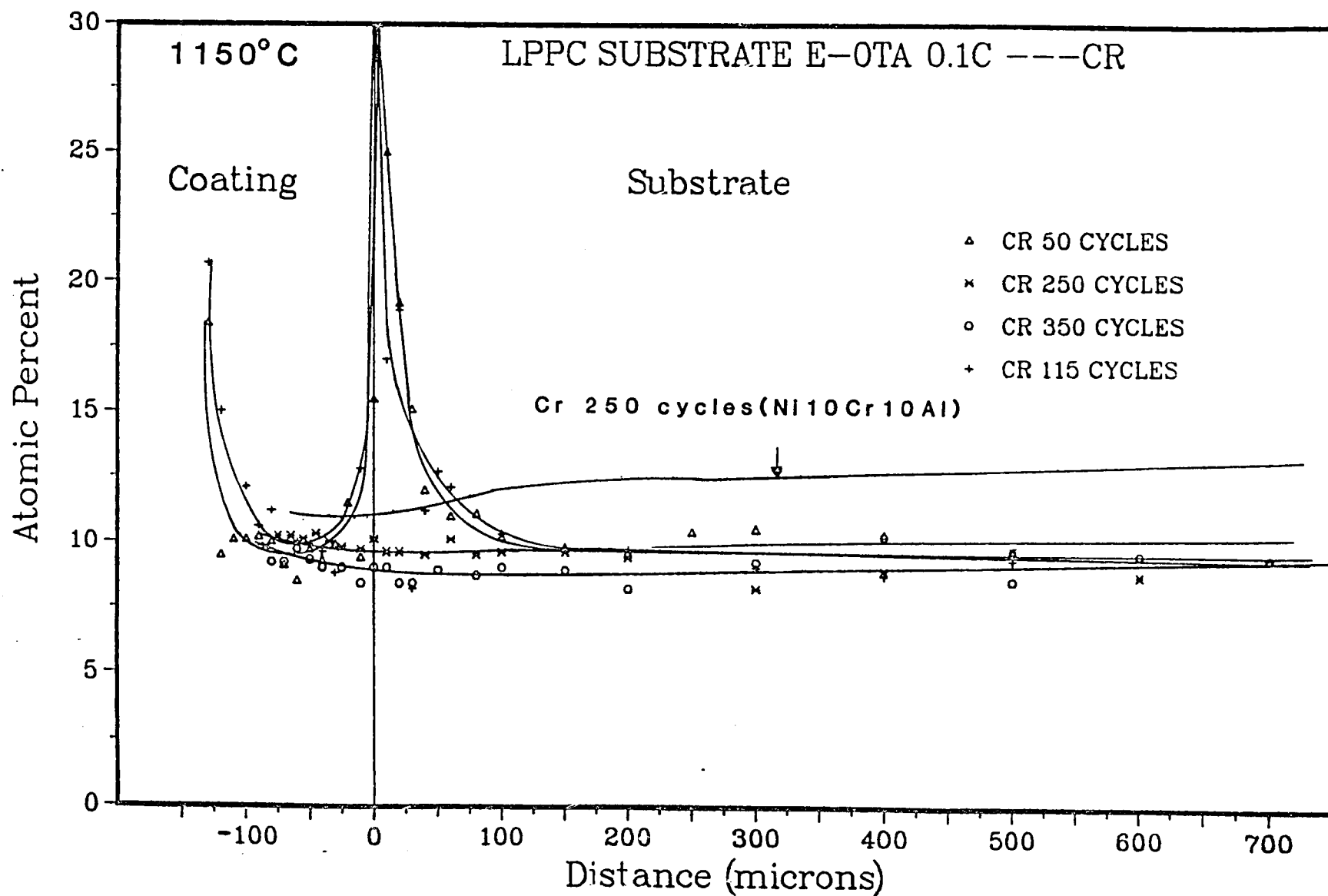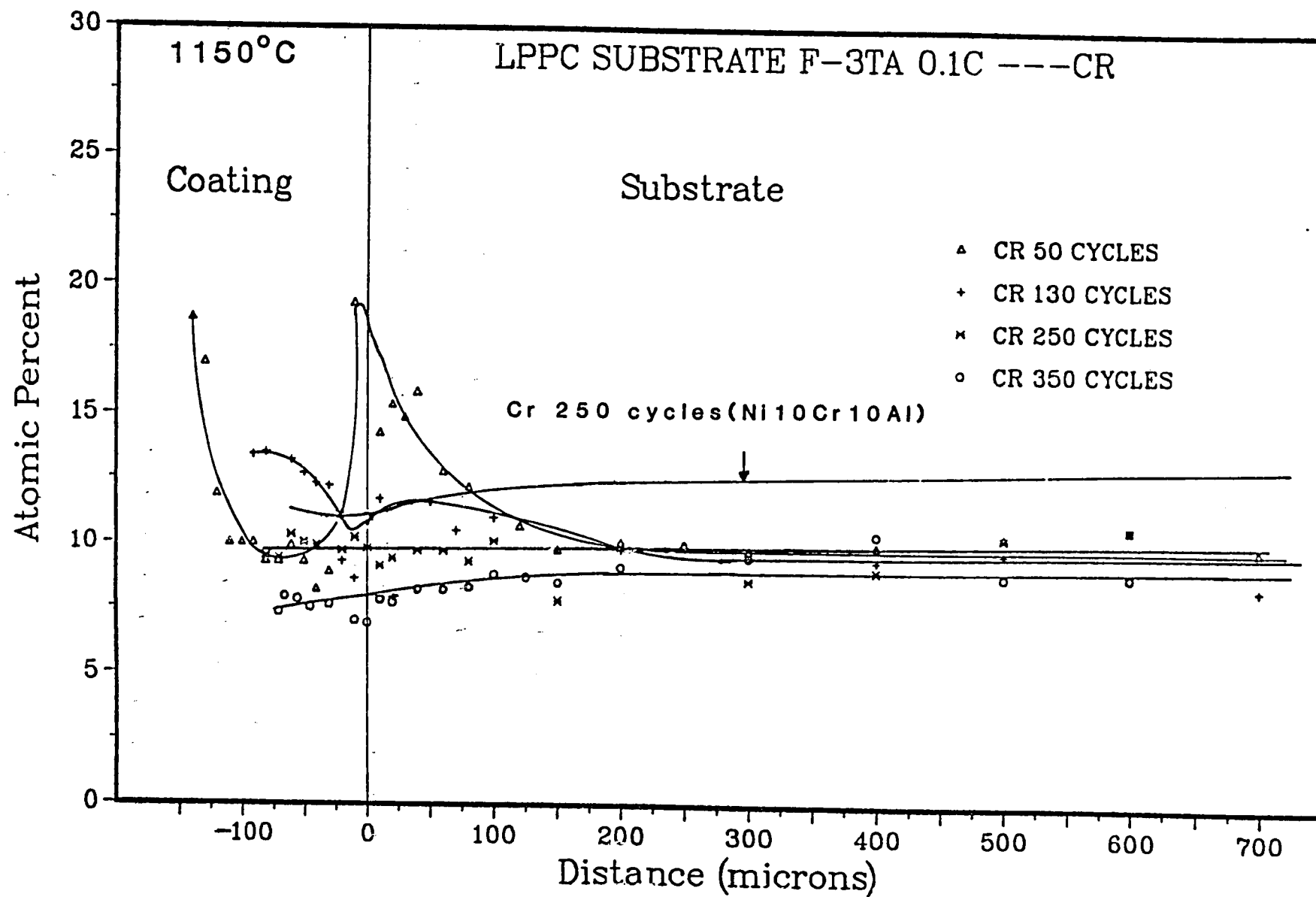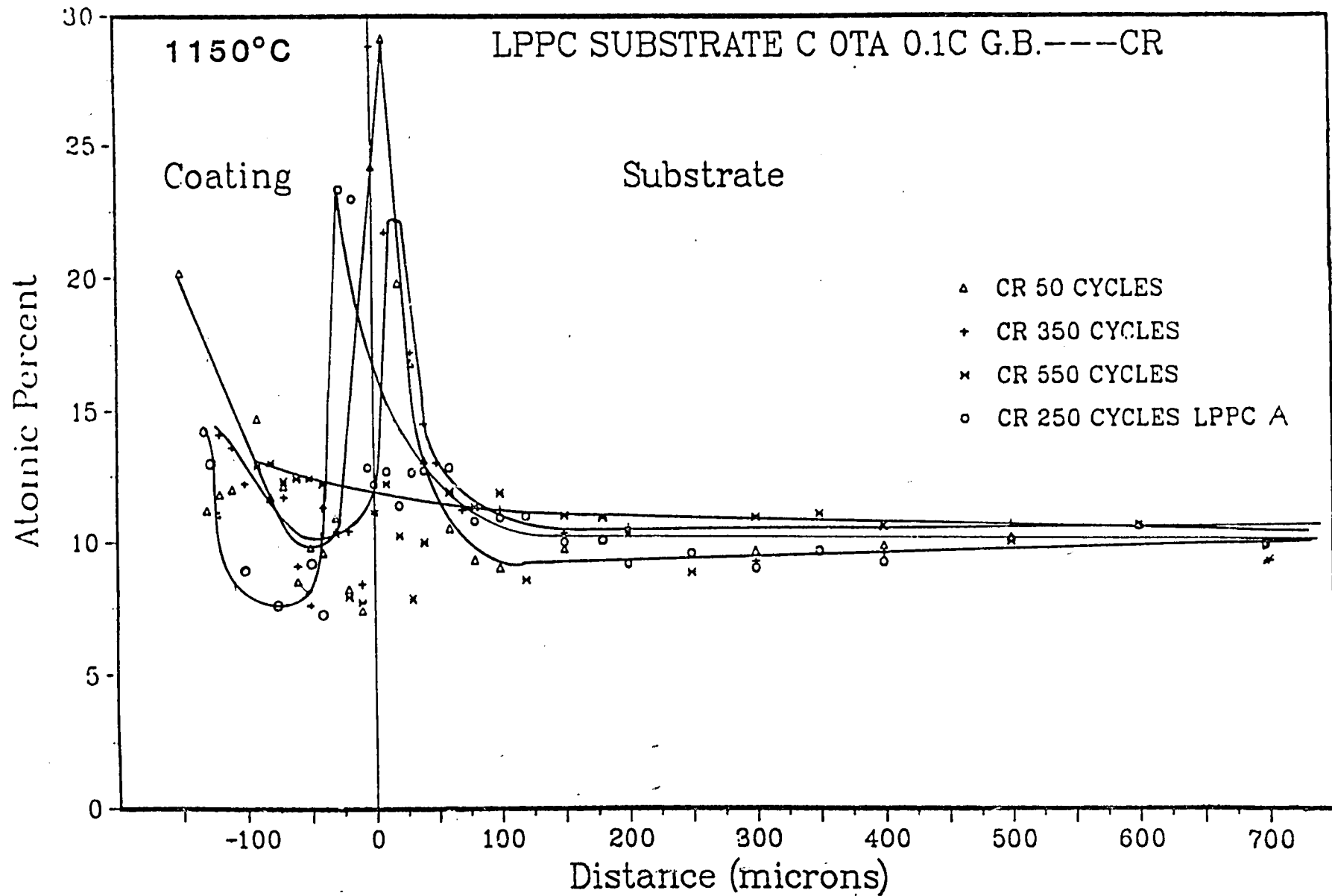d) LPPC substrate F -- 3 Ta, 0.1C
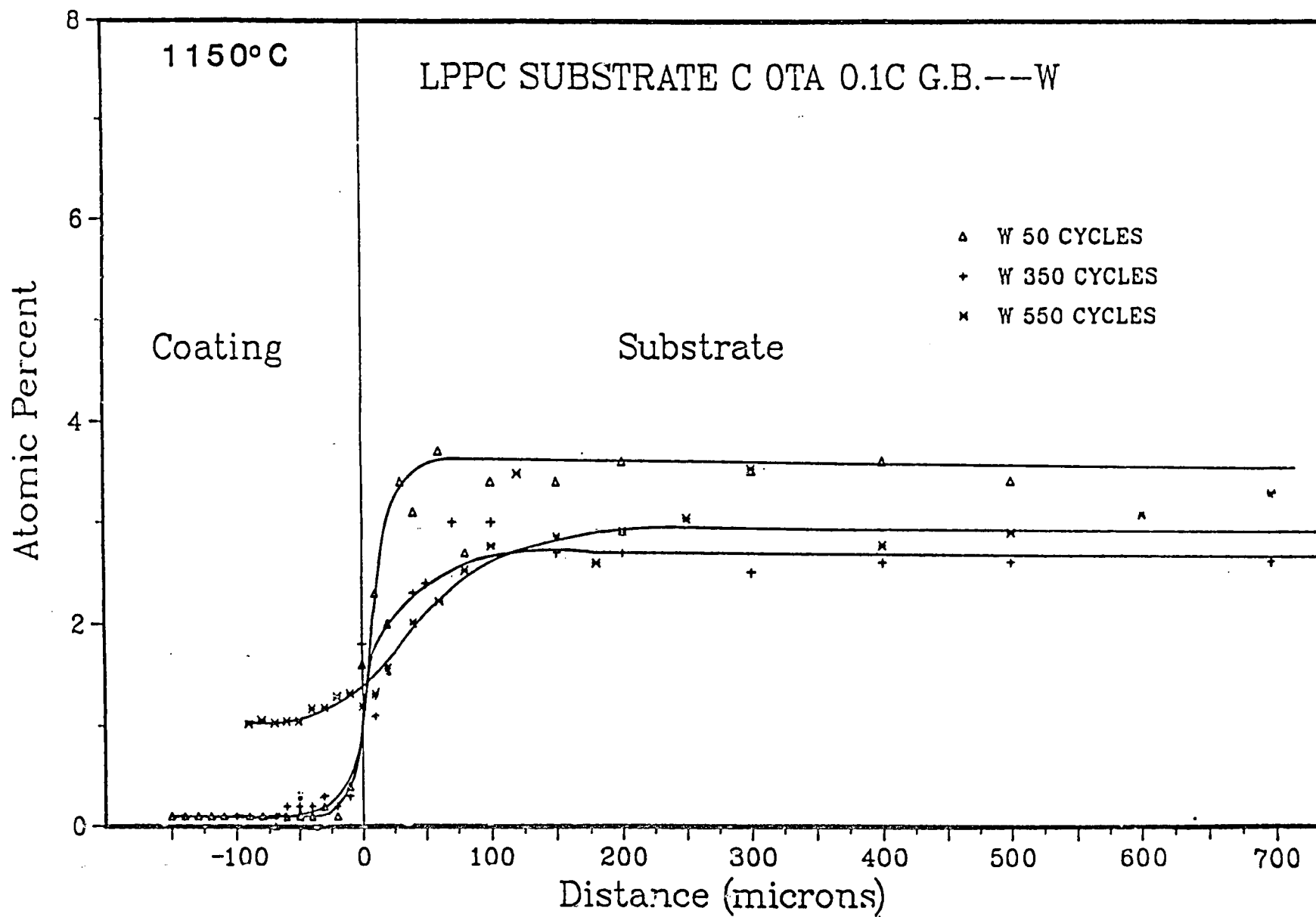
Figure 20   LPPC substrate concentration/distance profiles for W and Ta (con't)
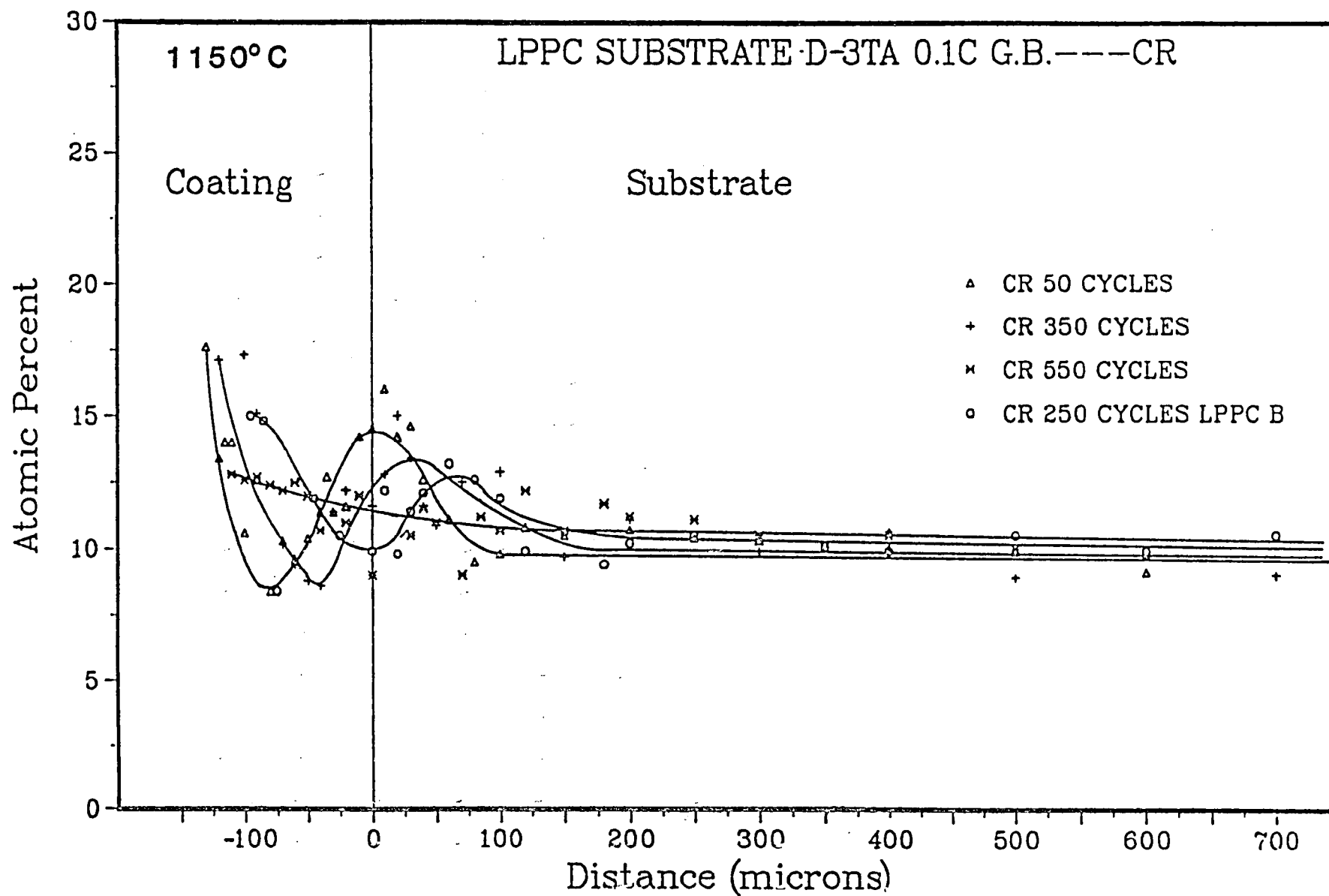   e) LPPC substrate C -- 0 Ta, 0.1C, g.b.
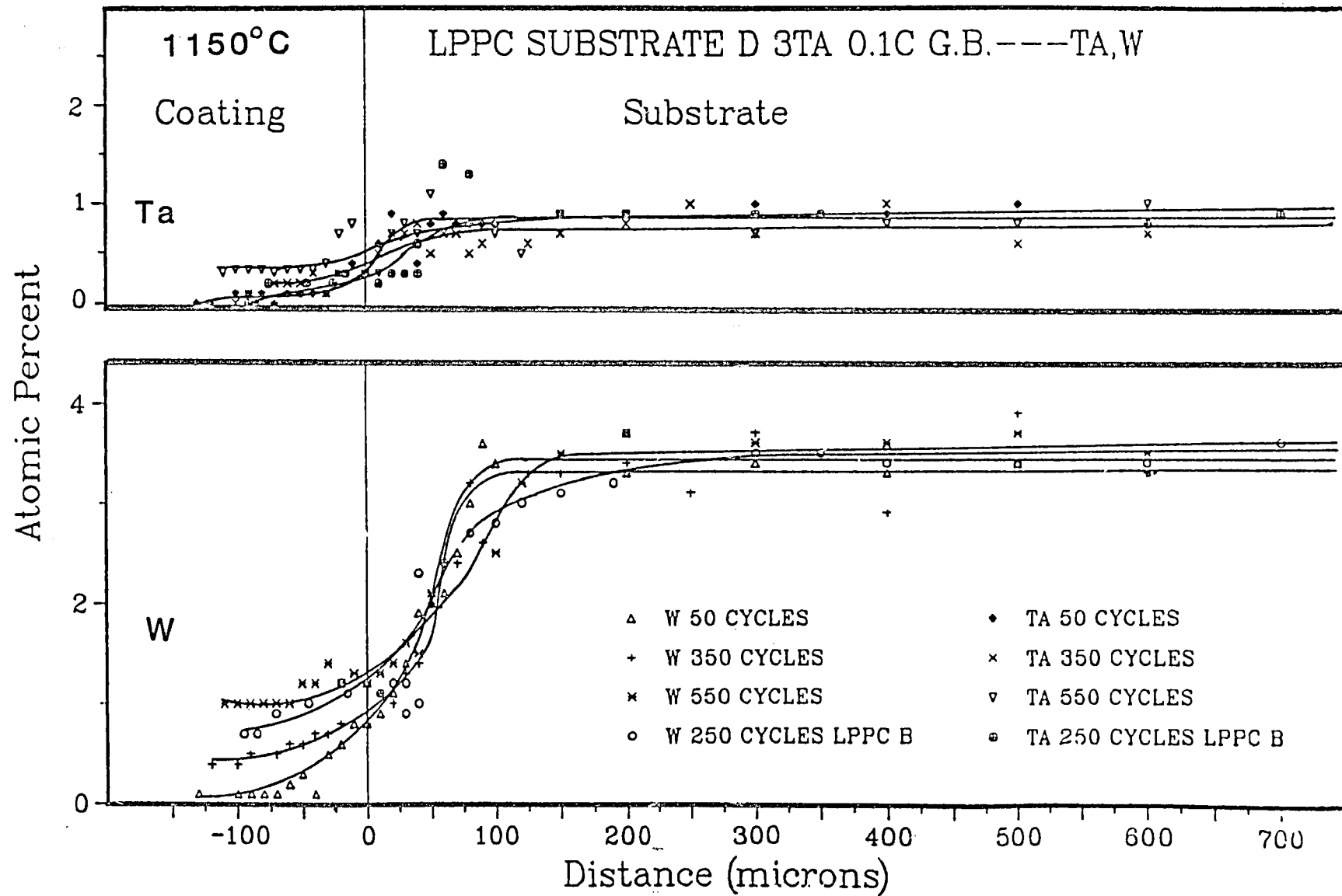
Figure 20   LPPC substrate concentration/distance profiles for W and Ta (cOn't)
             f) LPPC substrate D -- 3 Ta, 0.1C, g.b.

IV. DISCUSSION

Comparison of LPPC Mar-M247 and Ni-Cr-Al Substrates

For the LPPC superalloy and LPPC Ni-Cr-Al substrate systems (two systems with equivalent Al and Cr atomic percentages) to have equivalent oxidation resistance, the LPPC superalloy specimens should have slightly higher Al concentrations in the coating than the LPPC Ni10Cr10Al specimens after the equivalent number of cycles. The Ni10Cr10Al substrate composition was actually 7% Al and 13% Cr (atomic percent). The lower Al concentration (7% vs. 11% Al for the superalloy substrate) combined with a thinner coating on the Ni10Cr10Al specimen results in a lower initial Al supply than present for the LPPC superalloy specimens. The higher initial Al supply in the superalloy specimens should result in higher Al levels after the equivalent number of cycles. The slightly higher Al levels were present in all LPPC substrates without g.b.s.e. The Al profiles for the LPPC superalloy substrates without g.b.s.e. at the 350 cycle point were essentially identical to the Al profile for the LPPC Ni10Cr10Al substrate at the 250 cycle point. The identical profiles indicate that the simultaneous oxidation and coating/substrate interdiffusion mechanisms were similar for these two LPPC substrate systems.

The Cr concentration/distance profiles for the LPPC substrates without g.b.s.e. and LPPC Ni10Cr10Al substrate were similar at the 250 cycle point. In both cases, the Cr

profiles were smooth with no Cr maximum. The formation of the less protective oxides (consumption of Cr and Ni) should result in a flux of Cr to the oxide/coating interface (negative gradient). The negative Cr gradient for the Ni10Cr10Al specimen indicated that the less protective oxides were consuming Cr. The smaller negative and positive gradients for the LPPC superalloy substrates without g.b.s.e. indicated that less Cr has been consumed. The smaller gradients indicated that breakaway oxidation has been occurring for a shorter period of time for the LPPC superalloy substrates. The shorter periods reveal the higher oxidation resistance associated with the higher initial Al supply. However, the oxidation resistance difference is small since coating life is limited once the less protective oxides form.

The ΔWg curves also indicate that the LPPC substrates without g.b.s.e. had similar oxidation resistance to the LPPC Ni10Cr10Al substrate. The ΔWg curves were nearly identical for the four LPPC superalloy substrates without g.b.s.e. and the LPPC Ni10Cr10Al substrate. Close examination of the curves reveal slightly larger weight losses for the first 170 cycles for the LPPC Ni10Cr10Al substrate. The larger weight losses indicate slightly lower oxidation resistance associated with the lower initial Al supply. The large weight losses of two of the LPPC superalloy substrates after 170 cycles was due to the coating procedure. As mentioned, significant macrospalling of the

end coating occurred after 200 cycles. Macrospalling was a problem for both the Ni-Cr-Al and the superalloy specimens. However, the specimen geometry (Appendix 2) used in this study was more susceptible to end spalling. The large weight losses can, therefore, be associated with macrospalling of the ends and not oxidation resistance.

The similar oxidation resistance for both the LPPC superalloy and the Ni10Cr10Al substrate indicated that Al and Cr were the main controllers of oxidation resistance. The close correlation indicates the importance of understanding the Ni-Cr-Al system and also the potential importance of models developed for this system. However, there are limitations to the applicability of the Ni-Cr-Al system. The concentrations of the other elements in the coating are significantly affected by the particular coating/substrate system and coating thickness. Higher concentrations of these other elements in the substrate and thinner coatings can result in higher concentrations of these elements in the coating. Higher concentrations of these elements increases the probability of changes in oxidation resistance. Further investigation is necessary to appraise the applicability of the Ni-Cr-Al system for other situations.

Effect of Substrate Grain Boundary Strengthening Element (g.b.s.e.) Additions

The LPPC substrates with g.b.s.e. (B, Zr, and Hf) exhibited oxidation resistance higher than the substrates without these elements. The improved oxidation resistance

was due to the transport of Hf from the substrate into the coating. The Hf was detected in Hf-rich oxide particles associated with oxide intrusions near the oxide/coating interface. The improved oxidation resistance was not un-expected since Hf has been shown to improve oxidation re-sistance (32). Stringer, Allam, and Whittle (32) attributed the improvement in Co-Cr-Al alloys to the presence of the oxide intrusions. Further investigation is necessary to determine how Hf is improving the oxidation resistance for these oxidized LPPC superalloy substrates.

The small substrate concentrations of B and Zr in the substrate were considered too small to effect coating oxi-dation resistance. The substrate Zr concentration (0.05 wt.%) was less than the coating Zr concentration (0.1 wt.%). Therefore, higher Zr coating concentrations due to substrate Zr concentrations are unlikely. The small 0.01 wt.% B concentration also makes B an unlikely candidate for im-proved coating oxidation resistance.

Effect of Substrate Tantalum Concentration

The effect of Ta on oxidation resistance is dependent on the coating or alloy composition of the oxidized speci-mens. As indicated (Introduction), both increases and de-creases in oxidation resistance have been observed for coat-ing and alloy compositions that contain Ta. In this study, the small quantities of Ta (generally less than 1 wt.%) that

reached the surface of the coating did not affect oxidation resistance. However, microstructural changes due to Ta were observed.

Microstructural changes due to Ta were observed in both diffusion couple and oxidation studies. The most important effect of Ta was the reduction of $M_{23}C_6$ carbides at the coating/substrate interface. By adding Ta to high-carbon, tantalum-free LPPC substrates, the continuous $M_{23}C_6$ carbides changed to particle type carbides. The change in morphology was accompanied by a reduction in quantity. The reduction in quantity increases the mechanical integrity of the coating/substrate system. In diffusion couples, by increasing the Ta concentration, the thickness of the γ' depletion zone in the substrate was decreased. The effect was not observed in the oxidized LPPC substrate specimens. The difference was due to the development of a coarse $\gamma+\gamma'$ structure in the substrate of the LPPC specimens instead of single phase γ (γ' depletion) present in the diffusion couples. The $\gamma+\gamma'$ structure resulted from the higher Al diffusivity paths present in LPPC oxidized specimens. The as-sprayed coating provided numerous diffusion paths such as initial particle surfaces and γ/β interfaces (finer $\gamma+\beta$ microstructure than in couples). The effect of these numerous paths were also observed in the Ni-Cr-Al specimens investigated by Nesbitt (24). In this case, γ' ppts. were observed in the LPPC γ Ni10Al substrate after a four hour

96

anneal at 1150°C. These higher rates result in changes in the composition of the diffusion zone as compared to the diffusion couples. The β depletion zone thickness (coating) associated with interdiffusion decreased with increasing Ta in the LPPC substrates (not observed in diffusion couples). This decrease was attributed to the change in phase equilibrium due to the presence of Ta. However, these microstructural changes early in the process did not affect oxidation resistance.

Effect of Substrate Carbon Concentration

Limited interdiffusion was observed in $\gamma+\beta$/Mar-M247 diffusion couples that developed continuous $M_{23}C_6$ carbides. The continuous carbide formed in both the diffusion couples and the LPPC substrates (high-carbon, tantalum-free specimens). The development of this continuous barrier has potential importance. By limiting diffusion, the barrier would minimize both coating and substrate degradation. Limited degradation could result in improved oxidation resistance and substantially higher mechanical integrity. However, the continuous $M_{23}C_6$ carbide did not significantly limit interdiffusion in the oxidized LPPC substrates.

The presence of $M_{23}C_6$ carbides in the high-carbon substrates did not affect the oxidation resistance of the LPPC substrates. This result was due to the dissolution of the $M_{23}C_6$ carbides that formed early in the process. Unlike the

diffusion couples, where $M_{23}C_6$ carbides grow and coarsen
with time, the $M_{23}C_6$ carbides in the LPPC substrates dis-
solved with time. Their dissolution results from the
changing coating composition with time. The changing coat-
ing composition in the semi-infinite LPPC substrate re-
sults in time-dependent diffusion paths. In the infinite
diffusion couples, the diffusion path is independent of
time. Therefore, the $M_{23}C_6$ carbides will always be present
in the diffusion couples as long as the couple remains in-
finite. The dissolution results in C not affecting oxida-
tion resistance unless fracture of the $M_{23}C_6$ carbide occurs
early in the oxidation process.

The formation of the continuous $M_{23}C_6$ carbide layer
can result in catastrophic failure at the coating/substrate
interface. Cracks were observed in the continuous carbide
layer in both the diffusion couple and oxidation specimens.
Generally, the LPPC substrates are subject to thermal cyc-
ling. The presence of the brittle carbide is undesirable
in cyclic engineering applications. The catastrophic nature
of the failure was demonstrated by macrospalling of the en-
tire end coating at the coating/coating and coating/sub-
strate interfaces for one test. As noted, the addition of
Ta reduces the amount and changes the continuous carbide to
particles. The Ta addition may be necessary in applica-
tions where carbon is a required substrate addition.

98

Importance of Diffusion Couple Studies

Diffusion couple studies can be used to predict inter-diffusion and microstructural features for LPPC substrates. The diffusion couple studies predicted the formation of the continuous $M_{23}C_6$ carbides in the high-carbon, tantalum-free substrates; the decrease in $M_{23}C_6$ carbides with increasing Ta; and the Cr maximum present in the Cr profile. Generally, diffusion couples are easier to fabricate than LPPC specimens. Their easy fabrication make the diffusion couple an excellent tool for evaluating microstructural changes for new proposed substrate or coating compositions.

V. CONCLUSION

1. The oxidation resistance of the LPPC superalloy substrates without grain boundary strengthening elements was similar to the LPPC Ni-Cr-Al substrate of equivalent Al and Cr atomic percentages. Verified by:

    - Similar change in weight curves;
    - Similar surface oxides;
    - Similar concentration/distance profiles for Al and Cr;
    - Both exhibited a Cr maximum in the substrate.
    - Both exhibited β depletion in the coating (via interdiffusion).

2. Higher oxidation resistance was observed for LPPC substrates that contained grain boundary strengthening elements (Zr, Hf, and B). The improved resistance was associated with the transport of Hf from the substrate into the coating.

3. The effect of Ta on oxidation resistance is dependent on the compositions of the oxidized specimens. The small quantities of Ta (less than 1 wt.%) that reached the surface in this study did not affect oxidation resistance.

4. The amount of $M_{23}C_6$ carbides decreased with increasing Ta concentration. The decrease is due to the strong carbide forming abilities of Ta which limit the carbon available for the formation of $M_{23}C_6$

(Cr-rich) carbides.

5. The oxidation resistance was not affected by the formation and dissolution of the $M_{23}C_6$ carbides in the high-carbon LPPC substrates.

6. Significant increases in oxidation resistance were observed with increasing coating thickness.

7. The continuous $M_{23}C_6$ carbide layer limited interdiffusion in $\gamma+\beta$/Mar-M247 diffusion couples. This limitation was due to the continuous $M_{23}C_6$ barrier at the coating/substrate interface.

8. The γ' depletion thicknesses decreased with increasing Ta concentration in $\gamma+\beta$/Mar-M247 diffusion couples. The decrease was due to the γ' forming abilities of Ta.

9. Diffusion couple studies can be used to predict interdiffusion and microstructural features for LPPC substrates.

VI. REFERENCES

1. H. W. Grunling, K. Scheider, Thin Solid Films, 84, p. 1, (1981).

2. G. W. Goward, Source Book on Materials For Elevated Temperature Applications, pp. 369-386, ASM, 1979.

3. G. W. Goward, High Temperature Corrosion, R. A. Rapp, Editor, NACE, p. 553, 1983.

4. J. R. Rairden, M. R. Jackson, M.F.X. Gigliotti, M. F. Henry, J. R. Ross, W. A. Seaman, D. A. Woodford, and S. W. Yang, High Temperature Corrosion, R. A. Rapp, Editor, NACE, p. 561, 1983.

5. W. K. Halnan and D. Lee, High Temperature Protective Coatings, S. C. Singhal, Editor, AIME, p. 3, 1982.

6. S. Shankar, D. E. Koenig, and L. E. Dardi, J. of Metals, p. 33, 13, (1981).

7. J. A. Sprague, G. R. Johnston, F. A. Smidt, Jr., S. Y. Hwang, G. H. Meir, and F. S. Pettit, High Temperature Protective Coatings, S. C. Singhal, Editor, AIME, p. 93, 1982.

8. H. Bhat, H. Herman, and R. J. Coyle, High Temperature Protective Coatings, S. C. Singhal, Editor, AIME, p. 37, 1982.

9. J. E. Restall, B. J. Gill, C. Hayman, and N. J. Archer, The Superalloys, John Wiley and Sons, N.Y., p. 405, 1972.

10. F. J. Pennisi and D. K. Gupta, Thin Solid Films, 84, p. 49, (1981).

11. R. W. Smith, Thin Solid Films, 17, p. 1247, (1969).

12. Per Kofstad, High-Temperature Oxidation of Metals, John Wiley and Sons, N.J., p. 112, p. 264, 1966.

13. G. R. Wallwork and A. Z. Hed, Oxid. of Met., 3, p. 171, (1971).

14. A. Ashary, G. H. Meier, and F. S. Pettit, High Temperature Protective Coatings, S. C. Singhal, Editor, AIME, p. 105, 1982.

15. R. I. Jafee and J. Stringer, Source Book on Materials For Elevated Temperature Applications, p. 19-33, ASM, 1979.

16. S. J. Grisaffe, The Superalloys, John Wiley and Sons, N.Y., p. 341, 1972.

17. M. Nakamori, Y. Harada, and I. Hukue, High Temperature Protective Coatings, S. C. Singhal, Editor, AIME, p. 175,

18. F. H. Stot, G. C. Wood, and M. G. Hobby, Oxid. of Met., 3, p. 103, (1971).

19. C. A. Barrett and C. E. Lowell, Oxid. of Met., 11, p. 199, (1977).

20. C. A. Barrett and C. E. Lowell, Oxid. of Met., 13, p. 33, (1978).

21. A. Kumar, M. Nasrallallah and D. L. Douglas, Oxid. of Met., 8, p. 227, (1974).

22. C. Burman and T. Ericsson, High Temperature Protective Coatings, S. S. Singhal, Editor, AIME, p. 51, 1982.

23. P. L. Norman and J. D. Harston, "A Evaluation of the Hot Corrosion Resistance of Commercial High Chromium Nickel-Base alloys for Use in Gas Turbines," A. B. Hart and A. J. B. Cutter, eds., Wiley and Sons, N.Y., p. 260, 1973.

24. J. A. Nesbitt, Ph.D. Thesis, MTU, Houghton, MI, 1983.

25. G. E. Wasielewski and R. A. Rapp, The Superalloys, John Wiley and Sons, N.Y., p. 341, 1972.

26. D. P. Whittle, Acta Met., 17, 1247 (1969).

27. S. R. Levine, Met. Trans., 9A, 1237 (1978).

28. J. L. Smialeh and C. E. Lowell, J. Electrochem. Soc., 121, 800 (1974).

29. C. S. Giggins and F. S. Pettit, J. Electrochem. Soc., 118, 1782 (1971).

30. D. L. Deadmore and C. E. Lowell, Oxid. Metals, Vol. 11, 1977, p. 91.

31. C. S. Giggins, F. S. Pettit, Oxide Scale Adherence Mechanisms and the Effects of Yttrium, Oxide Particles and Externally Applied Loads on the Oxidation of NiCrAl, and CoCrAl Alloys, Report ARL TR 75-0234, Air Force Contract F33615-72-C-1702, June 1975.

32. D. P. Whittle, I. M. Allam and J. Stringer, <u>Materials and Coatings to Resist High Temperature Corrosion</u>, Edited by D. R. Holmes, A. Rahmel, Applied Science Publishers, 1978, pp. 55-69.

33. J. Stringer, I. M. Allam, and D. P. Whittle, Thin Solid Films, 45, (1977), pp. 377-384.

34. J. G. Smeggil and N. S. Barnstein, <u>High Temperature Protective Coatings</u>, S. C. Singhal, Editor, AIME, p. 61, 1982.

35. C. E. Lowell, J. L. Smialek, and C. A. Barrett, <u>High Temperature Corrosion</u>, p. 219, NACE, Editor, R. A. Rapp, 1983.

36. C. H. Wells, P. S. Follansbee, and R. R. Dils, Mechanisms of Dynamic Degradation of Surface Oxides, pp. 220-234, <u>Stress Effects and The Oxidation of Metals,</u> Edited by John V. Cathcart, AIME, 1975.

37. C. S. Giggins, E. J. Felten, and F. S. Pettit, <u>Stress Effects and the Oxidation of Metals</u>, Edited by J. V. Cathcart, AIME, 1975, p. 245.

38. J. A. Nesbitt and R. W. Heckel, <u>High Temperature Protective Coatings,</u> S. C. Singhal, Editor, AIME, p. 75, 1982.

39. F. S. Pettit, Trans., TMS-AIME, <u>239</u>, 1296 (1967).

40. J. R. Stephens, A Status Review of NASA's COSAM Program, NASA Technical Memorandum 82852, May 1982.

41. H. C. Nguyen, M.S. Thesis, MTU, Houghton, MI, 1984.

42. S. W. Yang, Oxid. of Met., Vol. 15, p. 375, 1981.

43. M. Gell, D. N. Duhl, and A. F. Giamel, <u>Superalloys 1980</u>, ASM, p. 205, 1980.

44. E. J. Felten, J. Electrochem. Soc., <u>108</u>, p. 490 (1961).

45. B. Lustman, Trans. Am. Inst. Min. Met. Ret. Eng., <u>188</u>, p. 995 (1950).

46. J. M. Francis and J. A. Juston, Corrosive Science, <u>8</u>, p. 574, (1968).

47. J. Stringer, Metall. Rev., <u>11</u>, p. 113 (1966).

48. H. Pfeiffer, Werkst. Korros., 8, p. <u>574</u>, (1957).

49. L. A. Carol, M.S. Thesis, MTU, Houghton, MI, 1984.

50. I. A. Kvernes, Oxid. of Met., <u>6</u>, p. 45, (1973).

51. G. M. Janowski, M.S. Thesis, MTU, Houghton, MI, 1985.

Appendix I

Substrate and Coating Analyses

TABLE A-1

Substrate and Coating Analysis (w/o)

	A	B	C	D	E	F	G	H	I	J	Coating
Ta	0.20	2.68	--	2.94	--	2.79	4.34	--	1.62	3.07	--
C	0.11	0.10	0.10	0.10	0.11	0.098	0.11	0.010	0.010	0.008	0.006
Cr	8.46	8.70	8.30	8.35	7.87	8.00	8.02	7.87	7.98	8.05	14.03
W	9.40	9.72	9.40	9.60	9.52	9.78	9.76	9.58	9.58	9.74	--
Co	9.60	10.20	9.45	9.64	9.08	9.60	9.70	9.22	9.43	9.60	0.038
Mo	0.51	0.58	0.49	0.56	0.48	0.55	0.58	0.48	0.53	0.55	--
Al	4.95	5.45	4.88	5.37	4.88	5.40	5.59	4.94	5.24	5.45	13.40
Ti	0.88	0.94	0.77	0.82	0.46	0.52	0.60	0.50	0.55	0.57	0.008
Zr	0.070	0.070	0.056	0.055	0.006	0.005	0.008	0.006	0.008	0.008	0.10
B	0.013	0.019	0.011	0.013	--	--	--	--	--	--	--
Hf	1.55	1.66	1.23	1.23	--	--	--	--	--	--	--
Ni	64.26	59.88	65.42	61.44	67.60	63.26	61.30	67.39	65.05	62.95	72.42

TABLE A-2

Substrate and Coating Analysis (a/o)

	A	B	C	D	E	F	G	H	I	J	Coating
Ta	0.07	0.88	--	0.97	--	0.91	1.43	--	0.53	1.01	--
C	0.53	0.50	0.49	0.51	0.52	0.48	0.53	0.049	0.049	0.040	0.025
Cr	9.58	9.98	9.37	9.57	8.84	9.12	9.21	8.87	9.06	9.21	13.48
W	3.01	3.16	3.00	3.11	3.02	3.15	3.17	3.05	3.08	3.15	--
Co	9.59	10.33	9.41	9.75	8.99	9.65	9.83	9.16	9.44	9.70	0.032
Mo	0.31	0.36	0.30	0.35	0.29	0.34	0.36	0.29	0.33	0.34	--
Al	10.80	12.05	10.61	11.86	10.56	11.86	12.37	10.73	11.46	12.02	24.80
Ti	1.08	1.17	0.94	1.02	0.56	0.64	0.75	0.61	0.68	0.71	0.008
Zr	0.045	0.046	0.036	0.036	0.004	0.003	0.005	0.004	0.005	0.005	0.055
B	0.071	0.105	0.060	0.072	--	--	--	--	--	--	--
Hf	0.51	0.56	0.40	0.41	--	--	--	--	--	--	--
Ni	64.41	60.86	65.38	62.35	67.22	63.84	62.34	67.24	65.38	63.81	61.60

106

APPENDIX II

Coating End Spalling

The formation of a thin oxide scale at the coating/coating interface during the coating process resulted in ΔWg curves indicating lower oxidation resistance. The presence of the γ layer (low Al phase) at the coating/coating interface in the as-sprayed microstructure can be attributed to the oxide scale (Figure A-1a). The detrimental effects of the oxide scale are two-fold. First, the oxide scale is brittle and susceptible to fracture. The brittle nature resulted in macrospalling of regions of the outer coating (second spray application) in all specimens (Figure A-1b). Second, this inner Al_2O_3 scale at the coating/coating interface grows during oxidation and results in additional Al consumption. The effects of the oxide scale (coating overlap) on Al consumption are depicted in Figures A-2 and A-3. In both figures, the increased β depletion (high Al phase) can be attributed to coating overlap.

The detrimental effects of end spalling were greater for the cylinder geometry used in this study than the pin geometry used in the Ni-Cr-Al study (1). As shown in Figure A-4, the pin geometry has a smaller percentage of coating overlap area than the cylinder geometry. The decrease results in less area being involved in end spalling.

All specimens examined in this study had the same geometry and dimensions (Figure A-4b) except substrates A and B. The difference (dictated by bar stock) was a shorter length (0.875" vs. .0950") for substrates A and B. The shorter length increases the percentage of overlap area which is affected by end spalling. The shorter length could be responsible for the slightly inferior ΔWg curves when compared to the other ΔWg curves (Figure 11b) for LPPC g.b.s.e.

In summary, macrospalling at the ends is a common problem for LPPC substrate "specimens". Pin-shaped geometries should be utilized to minimize this problem.

COATING   SUBSTRATE G

a)

γ-layer

COATING   SUBSTRATE F

b)

O.I.
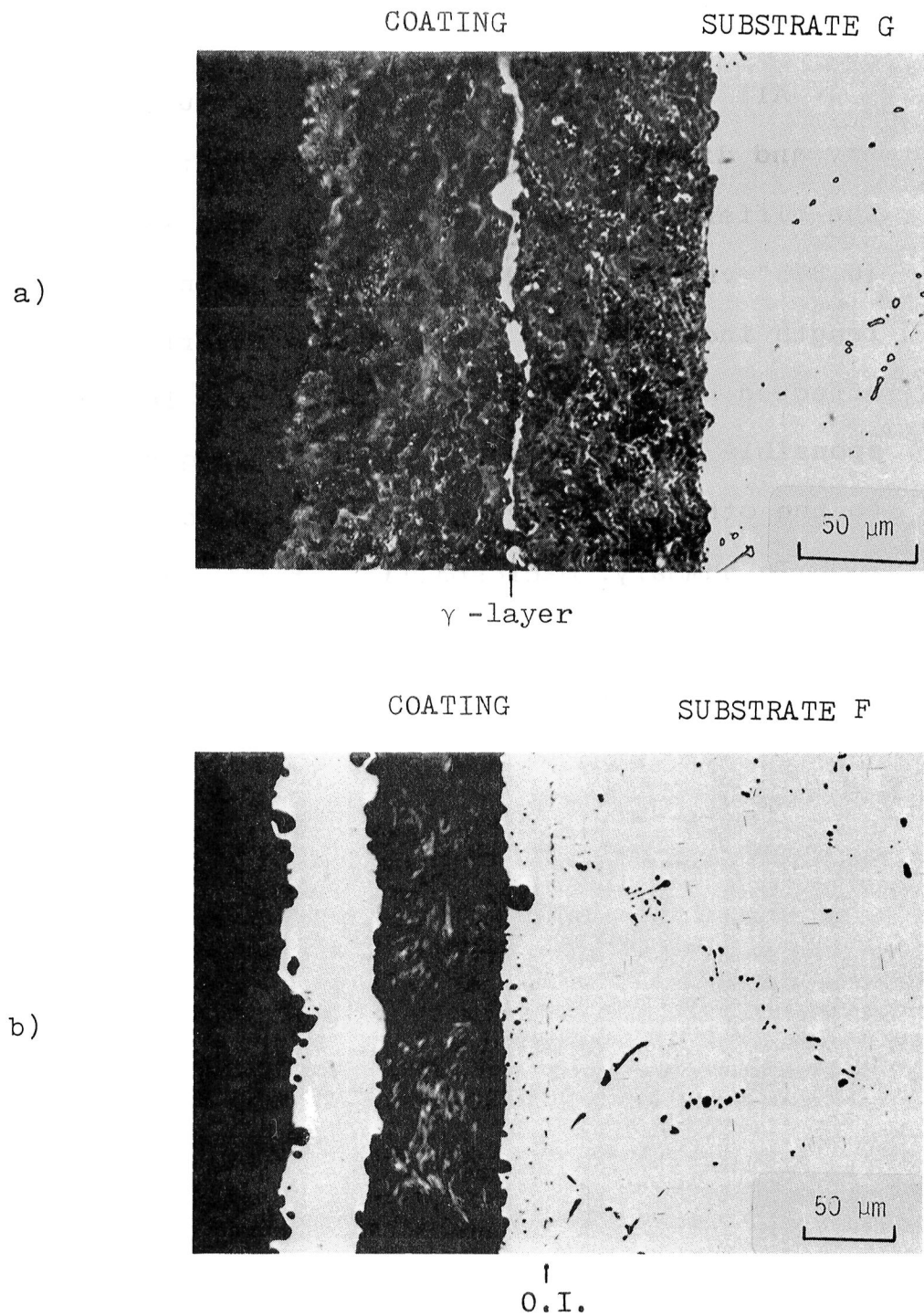
Figure A-1   Detrimental effects of two-step coating
process
a) Presence of γ-layer at coating/coating
interface
b) Fracture at coating/coating interface

COATING   Substrate J

a)

50 μm

O.I.

COATING   Substrate J

b)

50 μm
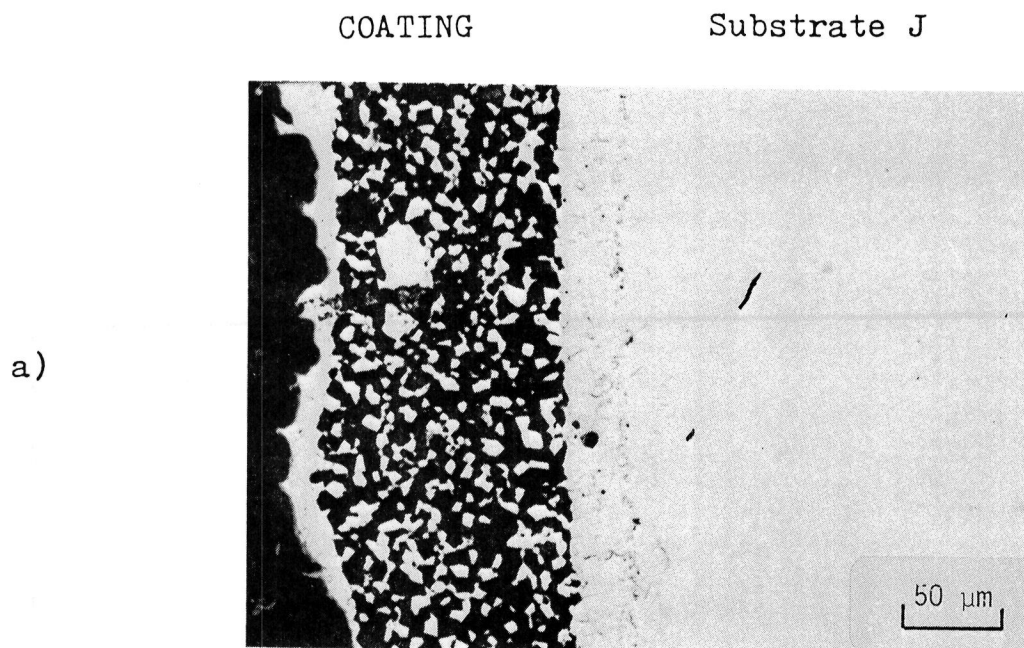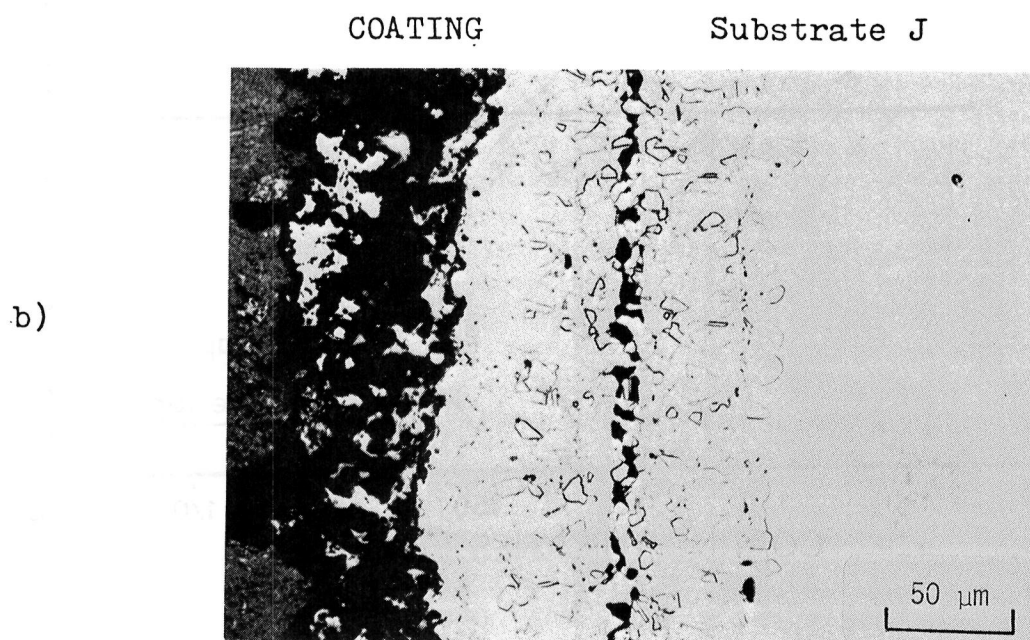
O.I.

Figure A-2   Photomicrographs demonstrating coating overlap
             effects: a) Section where no overlap is present
             b) Section where overlap is present
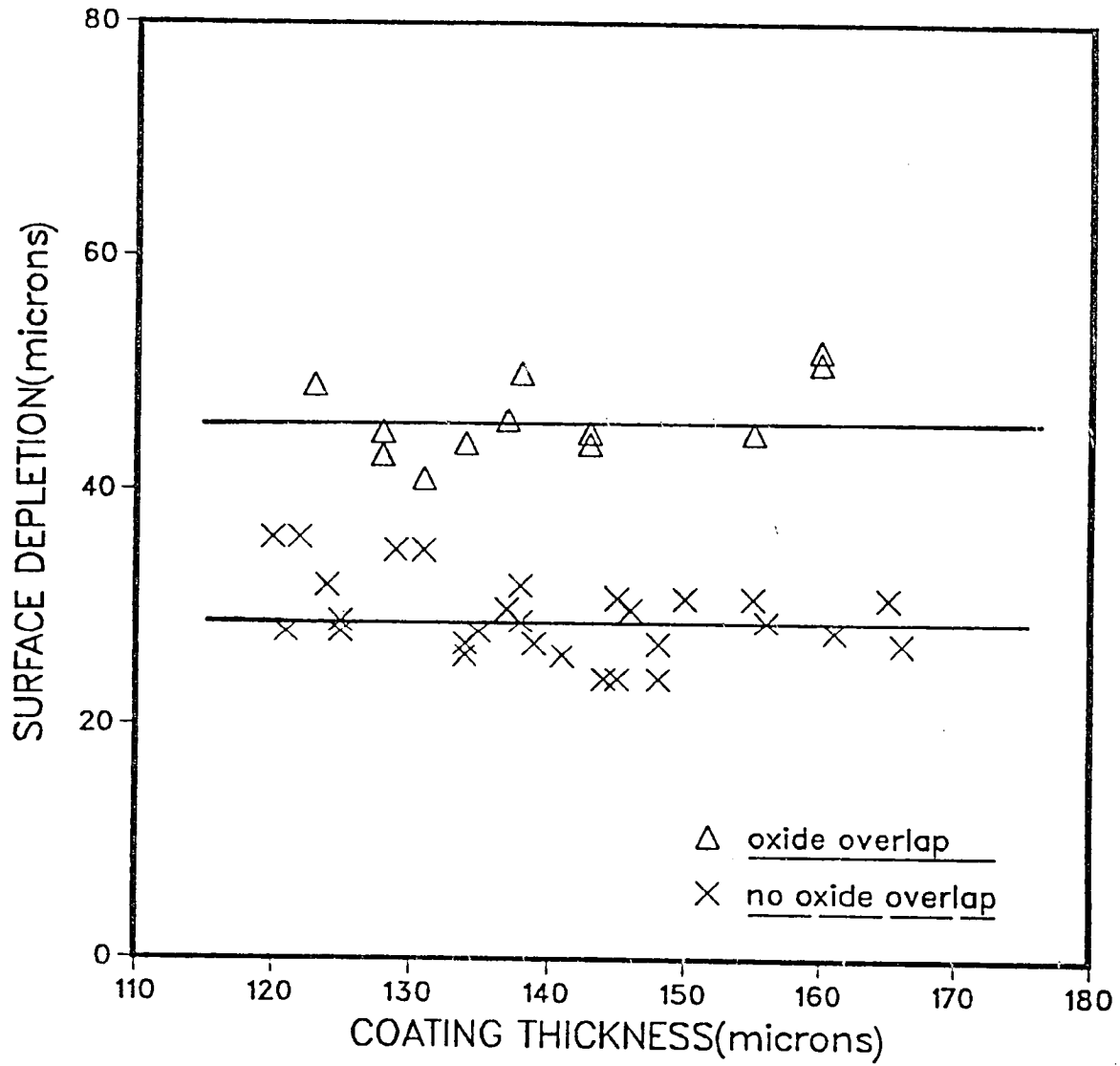
Figure A-3   A comparison of surface depletion (coating)
due to coating overlap

0.25" dia.

a)   As Machined

b)   As Coated

c)   As Machined

d)   As Coated

▬▬▬▬ First Step Coating

▭▭▭▭ Second Step Coating
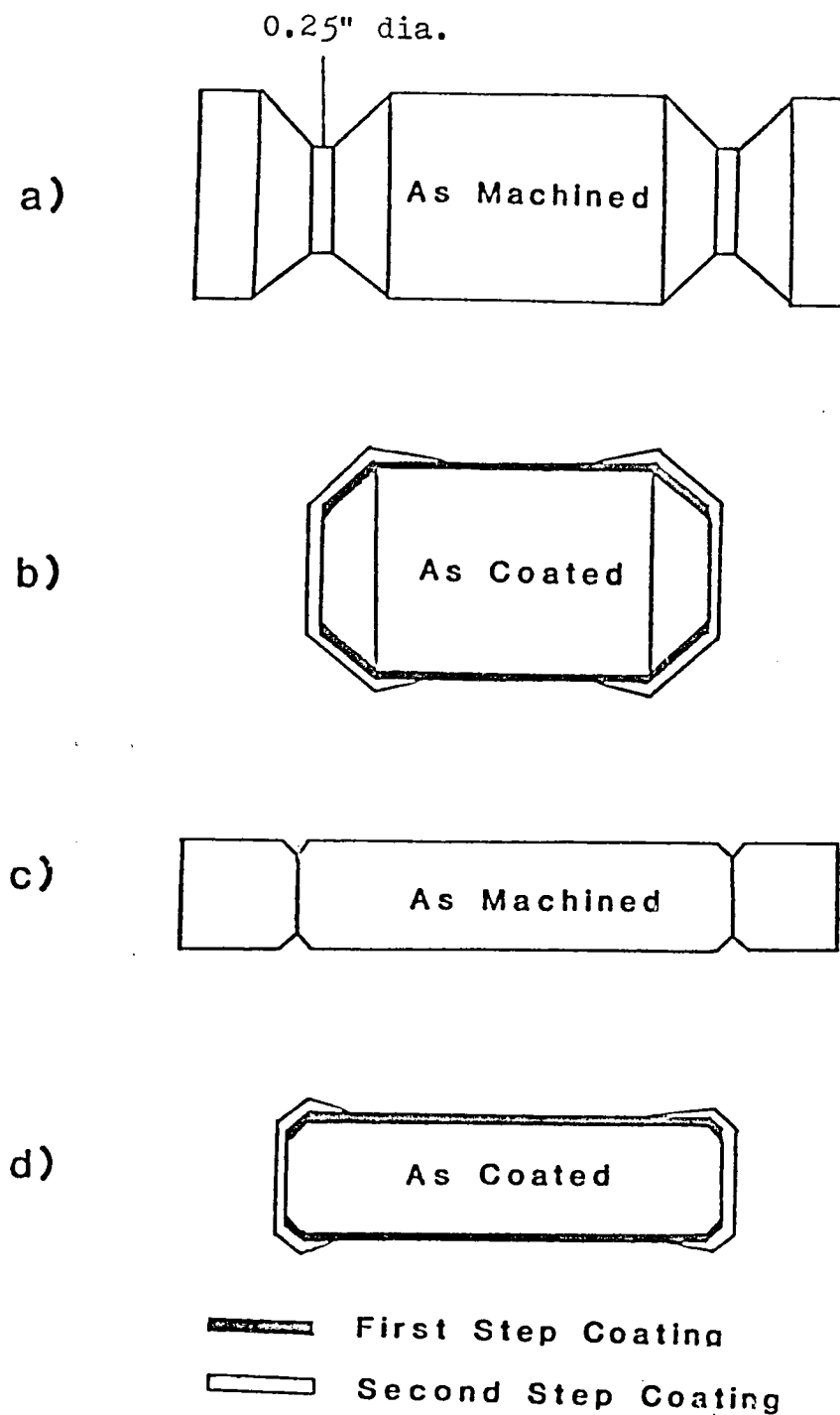
Figure A-4 A comparison of cylinder and pin shaped coated
specimens: a) as machined uncoated dumbell
geometry (this study); b) as coated cylinder
geometry; c) as machined uncoated pin specimen
(Nesbitt's Study); d) as coated pin geometry.
Scale 2:1 (coating thickness not to scale).

APPENDIX III

Concentration Measurements

The Al, Cr, Co, W, and Ta concentrations were determined with the aid of both an electron microprobe (EM) and scanning electron microscope (SEM). A listing of the technique employed for each specimen is given in Table A-3. Both systems were equipped with the necessary analytical capabilities. ZAF correction schemes were applied to both sets of measurements. The ZAF correction scheme accounts for differences between specimen and standard for electron scattering and retardation (atomic number effect, Z), absorption of X-rays within the specimen (absorption, A), and fluorescence effects (F)(1). The two systems were utilized to jointly handle this complex multicomponent multiphase system. The accuracy of the SEM/ZAF and EM/ZAF measurements were determined by the use of known compositions which included γ, γ', $\gamma+\beta$, and $\gamma+\gamma'$ specimens.

The SEM was a Joel 35C equipped with an EDAX energy dispersive system (EDS). The EDS system consisted of a Si(Li) counting system connected to a 711 series multichannel analyzer. This system was coupled to a Texas Instrument 733ASR high-speed data terminal which was interfaced to a Data General NOVA 2 mini-computer. The ZAF correction program was a modified version of the original computer program, designated as FRAME (2). The input into this program was the operating vol-

TABLE A-3

Measurement Procedure Employed

Substrate	System	Time	Elements					
			Al	Cr	Co	Ni	W	Ta
C	Couple	200 hrs.	SE	SE	SE	D	SE	--
D	Couple	200 hrs.	SE	SE	SE	D	PW	PW
E	Couple	200 hrs.	SE	SE	SE	D	SE	--
F	Couple	200 hrs.	SE	SE	SE	D	PW	PW
H	Couple	200 hrs.	SE	SE	SE	D	SE	--
J	Couple	200 hrs.	SE	SE	SE	D	PW	PW
C	Plasma	50 cyc.	SE	SE	SE	D	SE	--
D	Plasma	50 cyc.	SE	SE	SE	D	PW	PW
E	Plasma	50 cyc.	SE	SE	SE	D	SE	--
F	Plasma	50 cyc.	SE	SE	SE	D	PW	PW
H	Plasma	50 cyc.	SE	SE	SE	D	SE	--
J	Plasma	50 cyc.	SE	SE	SE	D	PW	PW
C	Plasma	350 cyc.	SE	SE	SE	D	SE	--
D	Plasma	350 cyc.	SE	SE	SE	D	PW	PW
E	Plasma	115 cyc.	SE	SE	SE	D	SE	--
F	Plasma	130 cyc.	SE	SE	SE	D	PW	PW
H	Plasma	350 cyc.	SE	SE	SE	D	SE	--
J	Plasma	350 cyc.	SE	SE	SE	D	PW	PW
A	Plasma	250 cyc.	SE*	SE*	SE*	D	SE*	--
B	Plasma	250 cyc.	SE*	SE*	SE*	D	PW	PW
C	Plasma	550 cyc.	SE*	SE*	SE*	D	SE*	--
D	Plasma	550 cyc.	SE*	SE*	SE*	D	PW	PW
E	Plasma	250 cyc.	PE	PE	PE	D	PW	--
E	Plasma	350 cyc.	PE	PE	PE	D	PW	--
F	Plasma	250 cyc.	PE	PE	PE	D	PW	PW
F	Plasma	350 cyc.	PE	PE	PE	D	PW	PW
H	Plasma	250 cyc.	PE	PE	PE	D	PW	--
H	Plasma	350 cyc.	PE	PE	PE	D	PW	--
J	Plasma	250 cyc.	PE	PE	PE	D	PW	PW
J	Plasma	350 cyc.	PE	PE	PE	D	PW	PW

SE = Scanning Electron Microscope With Energy-Dispersive X-Ray Spectrometer

PE = Electron Microprobe With Energy-Dispersive X-Ray Spectrometer

PW = Electron Microprobe with Wavelength-Dispersive X-Ray Spectrometer

D = Determined by Difference

*Kevex 8000 Series

tage; the angle between the incident beam, sample surface, and EDS collector; and the characteristic lines of the elements measured. In all cases, the SEM was operated at an accelerating voltage of 20 KV and a beam current of approximately $1x10^{-9}$ amperes. The K lines were used for Al, Co, Cr, and Ni, while the M lines were used for W.

The EP was a Material Analysis Co Model MAC 400 equipped with both energy dispersive spectrometer (EDS) and wavelength dispersive spectrometer (WDS) capabilities. The EDS system consisted of a Si(Li) counting system connected to a Kevex 5100 series multichannel analyzer. This system was coupled to a Digital pdp 11/03 computer. The input parameters were essentially the same as for the SEM system. The main difference was the probe operating at an accelerating voltage of 15 KV. The WDS system consisted of TAP and KAP crystal spectrometers. The K ratios determined by both the WDS and EDS systems were ZAF corrected by the MAGIC V program supplied by the Kevex system.

The SEM was used in most cases to measure Al, Cr, Co, and W compositions due to its rastering capabilities. The necessity of rastering was dictated by the fine two phase structure present in both the coating and the substrate. Both the $\gamma+\beta$ structure in the coating and the $\gamma+\gamma'$ structure in the substrate were too fine to probe individually (one micron or less). The rastering capabilities of the SEM provide averaging of the two phase compositions. A line profile

of approximately 100 μm was transversed perpendicular to the coating/substrate interface in both the coating and substrate. The system analyzed for Al, Cr, W, Co, and Ni (Ni determined by difference). The counting time for each measurement was at least 200 seconds. Before, during, and after each concentration/distance profile, measurements were made on known substrate and coating compositions. These measurements were performed to check the validity of the SEM/ZAF measurement system. The measurement was obtained from rastering a 100 μm line profile (10,000 μm area on γ+β coating specimen). The results are presented in Tables A-4 and A-5. In this case, γ+γ' and γ+β known compositions were measured. As shown, the error was generally less than 10% relative for both γ+β and γ+γ' specimens. This system under the same operating conditions also showed high correlation on Ni-Cr-Al specimens in another study (2).

The SEM measurement system would have been the only system used in this study if both Ta and W were not present in this nickel-base superalloy. The presence of both Ta and W provide two different analysis problems. First, the presence of the high quantities of Ni prevent the use of L lines to try to measure their contents. This was due to the significant Ni K lines which overlap both the Ta L and W L lines. Second, the M lines for Ta and W are too close to be separated by the EDS system. This inability resulted in the use of the EM's WDS system to measure the W and Ta compositions

TABLE A-4

Comparison of Chemical Analysis and SEM/ZAF
Measurement Procedure (γ+β)

Designation	Howmet Chemistry*	SEM/ZAF	ΔC	% Relative Error
γ-γ'C	4.88 Al	4.91 (±0.42)	0.03	0.6
	8.30 Cr	8.61 (±0.28)	0.31	3.5
	9.45 Co	9.59 (±0.43)	0.14	1.5
	9.40 W	9.33 (±0.64)	-0.07	0.7
γ-γ'D	5.37 Al	4.84 (±0.55)	-0.53	9.9
	8.35 Cr	8.70 (±0.38)	0.35	4.2
	9.64 Co	9.60 (±0.56)	-0.04	0.4
γ-γ'E	4.88 Al	5.10 (±0.28)	0.22	4.5
	7.87 Cr	8.77 (±0.32)	0.90	11.4
	9.08 Co	9.92 (±0.21)	0.84	9.3
	9.52 W	10.37 (±0.82)	0.85	8.9
γ-γ'F	5.40 Al	4.84 (±0.15)	-0.56	10.4
	8.00 Cr	8.52 (±0.42)	0.52	6.5
	9.60 Co	9.55 (±0.42)	-0.05	0.5
γ-γ'H	4.94 Al	5.00 (±0.42)	0.06	1.2
	7.87 Cr	8.86 (±0.29)	0.99	12.6
	9.22 Co	9.67 (±0.52)	0.45	4.9
	9.58 W	9.39 (±0.60)	-0.19	2.0
γ-γ'J	5.45 Al	4.96 (±0.47)	-0.49	9.0
	8.05 Cr	8.63 (±0.46)	0.58	7.2
	9.60 Co	9.31 (±0.28)	-0.29	3.0

*Total analysis present in Tables A-1 and A-2.

TABLE A-5

Comparison of Instrumental Analysis and SEM/ZAF
Measurement Procedure (γ+β)

Designation	Instrumental Analysis	SEM/ZAF	ΔC	% Relative
γ+β	13.40 Al	13.00 (±0.57)	-0.40	3.0
	14.04 Cr	14.78 (±0.75)	+0.74	5.3

in coating/substrate systems that contained both elements.

Both the EDS and WDS systems on the electron microprobe were utilized. Unfortunately, the electron microprobe at Michigan Tech only utilizes two spectrometers and was not automated. This made it impractical to measure all elements via wavelength dispersive analysis. As noted, the wavelength system was necessary to separate W and Ta concentrations. The other elements such as Al, Co, W, and Ni were generally determined on the SEM system. However, the presence of single phase γ in both the coating and substrate (100-300μm) for LPPC substrates that developed less protective oxides made the probe system applicable. In these cases, the LPPC substrate Al, Cr, Co, and Ni K ratios were determined by the energy dispersive system. The accelerating voltage used in EDS and WDS was 15 KV. The counting time for each EDS measurement was 200 seconds. Three 50 second counting periods were taken and averaged for each WDS measurement. The background of the specimen and pure standard were measured. After deadtime and background correction, the K ratios for W and Ta were determined. The MAGIC V ZAF program on the Kevex system was used to determine the EP/ZAF concentrations. In this case, γ and γ+γ' known specimens were utilized to check the accuracy of the EM/ZAF derived values. As shown in Tables A-6 and A-8, the largest error was of the same magnitude as the SEM/ZAF derived values. The known γ+γ' specimen was given a special heat treatment to develop a finer γ+γ' structure. The specimen was annealed at 1270°C

118

TABLE A-6

Comparison of Instrumental Analysis and EM/ZAF
Measurement Procedure

Designation	Instrumental Analysis	EM/ZAF	ΔC	% Relative Error
J-S	5.59 Al	5.12 (±0.52)	-0.47	8.4
	8.79 Cr	8.02 (±0.13)	-0.77	8.8
	10.35 Co	9.48 (±0.39)	-0.87	8.4
	10.28 W	11.00 (±0.18	+0.72	7.0
	3.15 Ta	3.67 (±0.52)	+0.52	16.5

TABLE A-7

Comparison of Atomic Absorption and EM/ZAF
Measurement Procedure

Designation	Atomic Absorption	EM/ZAF	ΔC	% Relative Error
γ-1	2.29 Al	2.17 (±0.07)	-0.12	5.2
	17.88 Cr	17.33 (±0.25)	-0.55	3.1
	79.93 Ni	82.51 (±1.63)	+2.58	3.2
γ-2	2.56 Al	2.28 (±0.11)	-0.28	10.9
	7.10 Cr	6.82 (±0.13)	-0.28	3.9
	90.34 Ni	89.31 (±1.23)	-1.03	1.1
γ-3	4.98 Al	5.64 (±0.26)	+0.66	13.2
	24.74 Cr	23.15 (±0.27)	-1.59	6.4
	70.28 Ni	69.02 (±0.81)	1.26	1.8

TABLE A-8

Comparison of Instrumental Analysis and SEM/ZAF
(8000 series) Measurement Procedure (γ+γ')

Designation	Instrumental Analysis	EM/ZAF	ΔC	% Relative Error
J-S	5.59 Al	5.45 (±0.08)	0.14	2.5
	8.79 Cr	8.49 (±0.13)	-0.30	3.4
	10.35 Co	10.70 (±0.19)	0.35	3.4
	10.28 W	*		
	3.15 Ta	*		

*Not able to separate W and Ta peaks on SEM EDS system.

TABLE A-9

Comparison of Atomic Absorption Analysis and SEM/ AF
(8000 series) Measurement Procedure (γ)

Designation	Atomic Absorption	EM/ZAF	ΔC	% Relative Error
γ-1	2.29 Al	2.49 (±0.10)	0.20	8.7
	17.88 Cr	17.39 (±0.14)	0.49	2.7
	79.93 Ni	80.09 (±0.15)	0.16	0.2
γ-2	2.56 Al	2.67 (±0.07)	0.11	4.3
	7.10 Cr	6.88 (±0.14)	0.22	3.1
	90.34 Ni	90.44 (±0.10)	0.10	0.1
γ-3	4.98 Al	5.44 (±0.08)	0.46	9.2
	24.74 Cr	24.49 (±0.28)	0.25	1.0
	70.28 Ni	70.07 (±0.30)	0.21	0.3

TABLE A-10

Comparison of Chemical Analysis and SEM/ZAF
(8000 series) Measurement Procedure (γ', $\gamma+\gamma'$)

Designation	Chemical Analysis	EM/ZAF	ΔC	% Relative Error
$\gamma-\gamma'$ A*	4.95 Al	5.30 ($\pm$0.09)	0.35	7.1
	8.46 Cr	8.78 ($\pm$0.33)	0.32	3.8
	9.40 W	9.42 ($\pm$0.23)	0.02	0.2
	9.60 Co	10.57 ($\pm$0.19)	0.97	10.1
$\gamma'-1$	10.21 Al	10.49 ($\pm$0.18)	0.28	2.7
	4.03 Cr	4.69 ($\pm$0.10)	0.66	16.4
	81.8 Ni	84.83 ($\pm$0.19)	3.03	3.7

*Total analysis present in Table A-1 and A-2.

(above the solutionizing temperature) for 12 hours and air cooled.

The concentration determination for W and Ta should be viewed as semi-quantitative. This designation results from two factors. First, the inability to produce W and Ta standards that contained small quantities of these elements. In most cases, the Ta concentrations measured were less than 1% in the coating, while W concentrations measured were less than 3% (both by weight). To obtain quantitative results in this case, standards with these low concentrations are required. This requirement is extremely important for these measurements since the use of M lines increases the absorption correction. Second, the electron microprobe was utilized in all specimens that contain Ta and W. The full utilization meant that in certain applications γ+β and/or γ+γ' were present. Their presence results in the possibility of hitting all or part of these phases. The result is significant scatter in the profiles. Tantalum and tungsten concentrations measured in this study provide important insight on the amount of Ta and W reaching the surface, but the limitations of the system must be realized.

*Special Note: Hardware problems led to the replacement of the EDAX EDS system on the SEM. The EDAX system was replaced by a Kevex 8000 series system. The specimens measured on this system are indicated with an asterisk (Table A-3). The accuracy of this SEM/ZAF system is shown in Tables A-8 through A-10.

REFERENCES

1. J. I. Goldstein, D. E. Newbury, P. Echlin, D. C. Joy,
    C. Fiori, and E. Lifshin, Scanning Electron Micro-
    copy and X-Ray Microanalysis, Plenum Press, N.Y.,
    1981.

2. EDIT/EP Operations Manual, EDAX International, Inc.,
    Manual #80-00503-00, 1975.

3. J. A. Nesbitt, M.S. Thesis, MTU, Houghton, MI, 1981,
    also published as NASA Contractor Report 165544,
    May 1982.

1. Report No. NASA CR-174851	2. Government Accession No.	3. Recipient's Catalog No.	
4. Title and Subtitle Effects of MAR-M247 Substrate (Modified) Composition on Coating Oxidation and Coating/Substrate Interdiffusion		5. Report Date February 1985	
		6. Performing Organization Code	
7. Author(s) Brian H. Pilsner		8. Performing Organization Report No. None	
		10. Work Unit No.	
9. Performing Organization Name and Address Michigan Technological University Houghton, Michigan		11. Contract or Grant No. NAG 3-216	
		13. Type of Report and Period Covered Contractor Report	
12. Sponsoring Agency Name and Address National Aeronautics and Space Administration Washington, D.C. 20546		14. Sponsoring Agency Code 505-33-62	

16. Abstract

The effects of $\gamma+\gamma'$ Mar-M247 substrate composition on $\gamma+\beta$ Ni-Cr-Al-Zr coating oxidation and coating/substrate interdiffusion were evaluated. These results were also compared to a prior study for a Ni-Cr-Al-Zr coated γ Ni-Cr-Al substrate with equivalent Al and Cr atomic percentages. Cyclic oxidation behavior at 1150 °C was investigated using change in weight curves. Concentration/distance profiles were measured for Al, Cr, Co, W, and Ta. The surface oxides were examined by x-ray diffraction and scanning electron microscopy. The results indicate that variations of Ta and C concentrations in the substrate do not affect oxidation resistance, while additions of grain boundary strengthening elements (Zr, Hf, B) increase oxidation resistance. In addition, the results indicate that oxidation phenomena in $\gamma+\beta/\gamma+\gamma'$ Mar-M247 systems have similar characteristics to the $\gamma+\beta/\gamma$ Ni-Cr-Al system.

17. Key Words (Suggested by Author(s)) Oxidation Overlay coatings Coating degradation Interdiffusion		18. Distribution Statement Unclassified - unlimited STAR Category 26	
19. Security Classif. (of this report) Unclassified	20. Security Classif. (of this page) Unclassified	21. No. of pages 126	22. Price* A07

National Aeronautics and
Space Administration

Washington, D.C.
20546

SPECIAL FOURTH CLASS MAIL
BOOK

U.S.MAIL

```
LIBRARY M.S.185
 NASA
 LANGLEY RESEARCH CTR.
 LANGLEY FIELD,VA 23365
```

NASA